Measurement of the inclusive isolated prompt photon cross-section in proton-proton collisions at $\sqrt{s} = 8$ TeV with the ATLAS detector

Michael Stoebe

Doctor of Philosophy

Physics

McGill University

Montreal,Quebec

2015-03-11

A thesis submitted to McGill in partial fulfillment of the requirements of the degree of Doctor of Philosophy

DEDICATION

This thesis is dedicated to both my father, Detlef Alfred Stoebe, and my grandfather, Fritz Stoebe.

ACKNOWLEDGEMENTS

I would like to thank my supervisors Prof. Brigitte Vachon and Mark Stockton who have guided and supported me continuously, not only on the selection and completion of this analysis, but also throughout my entire PhD.

Many thanks also to the entire McGill ATLAS group for allowing me to always seek help and support when needed and for providing a vibrant and friendly environment to be a part of. Particularly, Annabelle Chuinard and Sebastien Prince, for their help with the translation of the abstract into French.

I would like to give special thanks to the ATLAS Collaboration which allowed me to work on such a fantastic and exciting experiment and without which this thesis would not have been possible. I would also like to thank the whole ATLAS Standard Model Jet & Photon group, with particular thanks to Sergei Chekanov and Josu Cantero Garcia as they directly helped to develop the analysis and ensured the high quality of the measurement.

Last but not least I would like to thank my entire family, particularly Christiane, Christian and Eva-Beate Stoebe, as well as all my close friends for their continuous support and belief in me. Special thanks goes to my wife Michelle McKeown, as she has played a tremendous role in pushing, encouraging and helping me throughout the entire PhD program.

ABSTRACT

Differential cross-section measurements of the inclusive production of isolated prompt photons in proton-proton collisions at a centre-of-mass energy $\sqrt{s} = 8$ TeV are presented. The measurements cover the pseudorapidity regions $|\eta| < 1.37$ and $1.56 \leq |\eta| < 2.37$ in the photon transverse energy range $25\ \text{GeV} < E_{\text{T}}^{\gamma} < 1500\ \text{GeV}$. Results are based on a data sample corresponding to an integrated luminosity of $20.2\,\text{fb}^{-1}$, collected with the ATLAS detector at the Large Hadron Collider in 2012. Photon candidates are identified by combining information from the ATLAS calorimeters and inner tracker. The signal yield is measured using a data-driven technique. The measured differential cross-section values are compared to leading order and next-to-leading order perturbative QCD calculations and found to be in good agreement over ten orders of magnitude.

ABRÉGÉ

Des mesures de la section efficace différentielle de la production inclusive de photons prompts et isolés dans des collisions proton-proton à une énergie de centre de masse de $\sqrt{s} = 8$ TeV sont présentées. Les mesures recouvrent les régions de pseudorapidité $|\eta| < 1.37$ et $1.56 \leq |\eta| < 2.37$ pour des valeurs d'énergie transverse comprises dans l'intervalle 25 GeV $< E_{\mathrm{T}}^{\gamma} <$ 1500 GeV. Les résultats sont basés sur des données correspondant à une luminosité intégrée de $20.2\,\mathrm{fb}^{-1}$, recueillies avec le détecteur ATLAS au Large Hadron Collider en 2012. De potentiels photons sont identifiés en combinant l'information des calorimètres et du trajectographe interne d'ATLAS. La quantification du signal est obtenue en utilisant des techniques s'appuyant sur les données elles-mêmes. Les valeurs mesurées des sections efficaces différentielles sont en accord avec un calcul perturbatif de bas ordre de la théorie QCD, ainsi que les predictions obtenues à l'ordre suivant, sur plus de dix ordres de grandeur.

AUTHOR'S CONTRIBUTION

The data analysis and results presented in this thesis are the author's original work. The results presented in this manuscript rely on the tremendous work from thousands of physicists, engineers and technicians involved with the ATLAS detector and the LHC in general. Their contributions go beyond the sole building and running of the entire detector, but also include the development of a required large computational infrastructure (analysis software, Monte Carlo simulations, computing grid infrastructure, data quality monitoring framework etc.). The development and performance monitoring of algorithms used to reconstruct the presence of photons in the ATLAS detector is overseen by a dedicated group of physicists. Tools developed by this group were used and adapted for the specific need of the data analysis presented in this thesis.

All results specific to the photon cross-section measurements presented in this thesis, including tables and figures, are produced by the author himself with the exception of the following list:

- Some systematic studies were performed by Josu Cantero Garcia. In particular, he estimated the uncertainty on the cross-section measurements due to
  - the poorly known fraction of photons coming from fragmentation
  - the uncertainty related to the photon reconstruction efficiency dependence on the photon isolation criteria used

  - the pile-up uncertainty
  - the uncertainty associated to parton shower and hadronization models
  - the uncertainty assigned to hadronization and underlying event effects

  All results were however cross-checked by the author and all figures in the uncertainty Chapter 7 were produced by the author himself.

- The next-to-leading (NLO) order predictions of the inclusive photon cross-section in this thesis were produced by Sergei Chekanov. Nevertheless, the author produced his own samples with smaller statistics as part of the analysis development and as a cross-check.
- Figure 8–5 and Figure 8–6 were produced by Mark Stockton based on data provided by the author and the results from previous ATLAS publications.
- The visual representation of the event shown in Figure 8–4 was produced by Mark Stockton based on the event selection provided by the author.

In addition to the work presented in this thesis, the author performed validation and performance studies on the jet triggers deployed during the 2011 data taking period with a centre-of-mass energy of 7 TeV. The author was also involved in the trigger and data quality monitoring, ensuring good and continuous recording of collision events.

TABLE OF CONTENTS

LIST OF TABLES

LIST OF FIGURES

CHAPTER 1
Introduction

The extensive range of proton-proton collision energies provided by the Large Hadron Collider (LHC) presents particle physicists with a special opportunity to further validate and extend our understanding of nature. The work presented in this thesis consists of the most precise measurement of the production rate of photons in proton-proton collisions. The measurement is used to test predictions of the Standard Model (SM) of particle physics. A brief summary of the SM is given in the next section of this chapter followed by an overview of the analysis.

1.1 The Standard Model

The Standard Model (SM [1])[1] of particle physics describes the interactions between point-like, elementary particles; that is, particles having no substructure. These particles are specified by their charges[2] , spin[3] , and mass. Particles that make up ordinary matter are spin 1/2 fermions.

[1] The SM is a gauge invariant relativistic quantum field theory based on a SU(3) $\times$ SU(2) $\times$ U(1) local gauge symmetry.

[2] A charge is a quantum number associated with a fundamental force. For example, the electric charge for electromagnetic interactions.

[3] Spin refers to the intrinsic angular momentum carried by particles as another quantum number.

The twelve different types of fermions in the SM can be grouped into three generations (see Table 1–1), based on increasing fermion masses. The fermions within each generation are further classified as either leptons or quarks, the difference being that quarks are the only fermions interacting via the strong force. Furthermore, for each of these twelve types of fermions, a corresponding antiparticle exists, characterized by the exact same mass but opposite charges. For example, the antiparticle associated with the electron is the positron. The positron has a positive electromagnetic charge as opposed to the electron's negative charge. Throughout the thesis both particle and antiparticle states are implied when referring to fermions.

	Generation			Interaction
	I	II	III	
Quarks	u d	s c	t b	electromagnetic, weak, strong
Leptons	e	μ	τ	electromagnetic, weak
	ν_e	ν_μ	ν_τ	weak

Table 1–1: Summary of the different types of elementary fermions in the Standard Model and the forces through which they can interact. Each symbol represents a different type of fermion. The three generations arrange the fermions based on their difference in mass.

Interactions between fermions are described in the SM by the theory of the electromagnetic and weak force (electroweak theory) and the theory of the strong force (quantum chromodynamics) [2]. The forces are mediated through force-carrying spin-1 bosons. The photon (γ) is the carrier of the electromagnetic force. The mediator of the strong force is the gluon (g) and the $W^{\pm}$ and Z^0 are the force carriers

of the weak force[4] . Table 1–2 shows the mass[5] of these mediating particles and the relative strength of each force. Based on the energy dependence of the coupling strength of each force it is important to mention that the quoted values of the relative strength are based on interaction energies of a few GeV.

Interaction	Particle	mass [GeV]	Relative Strength
Electromagnetic	γ	0	$\frac{1}{137}$
Weak	$W^{\pm}, Z^0$	80, 91 [3]	10^{-6}
Strong	g	0	1

Table 1–2: Standard Model spin 1 gauge bosons.

1.2 Analysis Overview

The probability of producing at least one photon in high-energy proton-proton collisions is described by a quantity called cross-section. The inclusive isolated photon cross-section presented in this thesis is measured by counting the number of proton-proton collisions that resulted in the production of at least one photon. In addition, the number of photon events[6] is corrected for photon selection efficiencies and detector effects specific to the ATLAS detector. A large variety of sources of uncertainty are studied and included in the final cross-section results.

[4] The fourth known force of nature, gravity, is not described by the SM

[5] Throughout the thesis natural units, where c = 1, are used.

[6] An event refers to a proton-proton collision and its results.

The cross-section measurement is split into four regions of pseudorapidity[7] and measured as a function of transverse photon energy (E_{T}^{γ}) of up to 1500 GeV. The benefit of dividing this measurement into pseudorapidity regions is to probe different values of momentum transfer in proton-proton collisions.

Previous studies of prompt photon production were performed based on proton-proton collisions at the ISR [4](CERN) in 1978, and then followed up by measurements performed at subsequent particle colliders. This includes prompt photon production measurements at HERA [5][8] in electron-proton collisions, as well as the Tevatron [6, 7] based on proton-antiproton collisions at a centre-of-mass energy of $\sqrt{s} = 1.96\,\mathrm{TeV}$. The most recent measurements of the inclusive prompt photon production cross-section have been made by the CMS [8] and ATLAS [9–11] collaborations at the LHC, based on proton-proton collisions at a centre-of-mass energy of $\sqrt{s} = 7\,\mathrm{TeV}$.

The measurement presented in this thesis is based on proton-proton collisions at a centre-of-mass energy of $\sqrt{s} = 8$ TeV of the ATLAS collaboration. The photon production cross-section is measured for the first time at transverse photon energies beyond 1 TeV. In addition, the low E_{T}^{γ} region ($E_{\mathrm{T}}^{\gamma} = 25$ GeV) is explored, providing

[7] Pseudorapidity (η) is commonly used in high energy physics, since the particle flux resulting from inelastic collisions remains approximately constant in units of η. It is defined as: $\eta = -\ln\left(\tan\left(\frac{\theta}{2}\right)\right)$ ($\eta = 0$ for $\theta = 90°$ and $\eta = \infty$ for $\theta = 0°$, where θ represents the polar angle).

[8] An overview of prompt photon production measurements is given in this reference.

further insight into the poorly understood theoretical description of photons fragmenting (originating) off of a parton from the main interaction. The measurement presented not only revisits this region with increased statistics and precision, but is also able to push into phase space regions that were previously not accessible. The large reach in E_{T}^{γ} also results in a continuous precision measurement of the cross-section over ten orders in magnitude and provides a baseline for a variety of measurements, including photons either as signal or background. Another impact of this analysis concerns the Parton Distribution Function (PDF) of the colliding protons. In particular, due to the high probability of photon production from gluon-quark interactions at the LHC, the measurement of the photon cross-section can impact the understanding and extrapolation of the gluon PDF since it is a direct probe of the hard interactions.

The thesis is structured as follows: Chapter 2 presents an overview of the theoretical background related to the measurement presented in this thesis. Chapter 3 describes the experimental environment, from the location of the experiment to the specifics of the simulated and recorded data. A detailed explanation of the event and photon selection is then provided in Chapter 4. In Chapter 5, the signal efficiency and background subtraction method are introduced. The unfolding procedure used to remove detector effects from the measuring device (the ATLAS detector) is laid out in Chapter 6. The relevant uncertainties to the cross-section measurement are explained in Chapter 7. The final cross-section and comparisons to theoretical predictions, as well as previous results, are presented in Chapter 8. The conclusion and outlook are provided in Chapter 9.

CHAPTER 2
Theory

The relevant theoretical concepts beyond the general introduction of the Standard Model (SM) will be presented in this chapter. On the grounds that proton-proton collisions are the starting point of this measurement, the theoretical description of the proton and its constituents is of essential importance and will be the focus of the first section in this chapter. Following this, details of the photon production mechanism and its implication for the cross-section measurement presented in this thesis will be discussed.

2.1 The Proton and its Content

In 1917 Ernest Rutherford discovered that the atom was made out of a central positively charge nucleus [12]. In his experiment Rutherford studied the scattering angles of α-particles projected onto a thin gold foil. Based on his results, Rutherford constructed a new model of the atom. In his new model, the atom is described as being made up of a positively charged nucleus in its centre surrounded by a "cloud" of negatively charged particles later identified as being electrons. Following the discovery of the neutron in 1932 by James Chadwick [13] the nucleus was understood as being made up of protons and neutrons. In the late 1960's results of high energy electrons scattering off protons (deep inelastic scattering) at the Stanford Linear Accelerator Centre [14] suggested that the proton itself has a substructure and is

not a fundamental particle. The results were theoretically explained by the Parton Model introduced by Feynman [15] and Bjorken [16]. This model describes the proton consisting of loosely bound point-like particles and reduced the deep inelastic scattering with protons to an elastic scattering off a parton within the proton.

Today we know that these partons are the quarks and gluons of the SM, which make up the protons and neutrons. The theoretical description of quarks as loosely bound point-like particles within the theoretical framework of Quantum Chromo Dynamics (QCD) is achieved by introducing the hypotheses of asymptotic freedom and colour confinement [17]. Asymptotic freedom refers to the decreasing strength of the strong force (α_s) with decreasing distance between two partons. Conversely, the strength of the strong force is assumed to increase with increasing distance. The result is that quarks cannot be separated and therefore cannot be observed as single particles outside bound states consisting of multiple quarks. These bound states are generally and throughout this thesis referred to as hadrons (e.g. protons, neutrons, pions, etc.). The assumption of colour confinement is that all bound states in nature have to be neutrally charged with respect to the charge of the strong force called "colour". With the underlying assumption of asymptotic freedom and colour confinement, the Parton Model used to describe the deep inelastic scattering experiments could now be understood as a perturbative expansion of QCD in orders of α_s.

A visual representation of the perturbative expansion, often used in the calculation of physical observables in quantum field theories, such as QCD, has been developed by Richard Feynman and is referred to as Feynman diagrams [18, 19]. The particles in these diagrams are represented by lines and interaction points, as vertices. The

probability for an interaction to occur is proportional to the coupling strength of the force involved i.e. the interaction point can be an electromagnetic, weak or strong force vertex.

In summary, a proton is not a fundamental particle (without substructure). The proton is to first order made up of three so called "valence" quarks (two ups and one down quark). The term valence quarks is used because they are the fundamental particles that describe/carry the main properties of the proton i.e. electromagnetic charge, spin and momentum of the proton.

2.1.1 Parton Distribution Functions

A proton is a dynamic bound state. Although the three valence quarks within a proton behave as if they are very loosely bound with each other, these quarks continuously emit and absorb gluon radiation. Gluons may also split spontaneously into quark-antiquark pairs which can annihilate back into gluons. Therefore, the valence quarks of a proton may be thought of as "bathing" inside a sea of quarks and gluons. Interactions, inside the proton, between the proton constituents mostly involve small momentum transfers, which corresponds to large values of the coupling strength of the strong force. Therefore, these interactions between the proton constituents cannot be calculated using perturbative QCD. The internal dynamics of the proton's constituents are empirically modelled by Parton Distribution Functions (PDFs). These PDFs describe the probability of an incident particle to strike a parton inside the proton carrying a fraction x of the total proton momentum at a particular energy-momentum transfer value of Q^2. These PDFs are extracted

from a large number of experimental measurements of rates of different reactions involving a proton [20]. The Q^2 dependence of the PDFs is described using the Dokshitzer-Gribov-Lipatov-Altarelli-Parisi (DGLAP) equations [21–23]. PDF measurements obtained at a fixed value of Q^2 can be extrapolated to different Q^2 values using these equations. An example of PDFs extracted by the HERAPDF collaboration [24] using measurements obtained by the H1 [25] and ZEUS [26] experiments is shown in Figure 2–1. The PDFs are shown as function of the proton momentum fraction x at a fixed momentum transfer value of $Q^2 = 10$ GeV. It can be seen that, at large value of x, the three valence quarks each carry nearly 1/3 of the total proton momentum. The probability distribution function of up-type quark has a maximum value of approximately 0.6 corresponding to the two valence up quarks, and the probability distribution function of down-type quark has a value of 0.3 corresponding to the one valence down quark in a proton. Sea quarks and gluons make up the remaining fraction of the total proton momentum. For small values of x ($< 10^{-2}$) the probability to strike a gluon within a proton dominates by at least a factor of two compared to the probability of striking a quark.

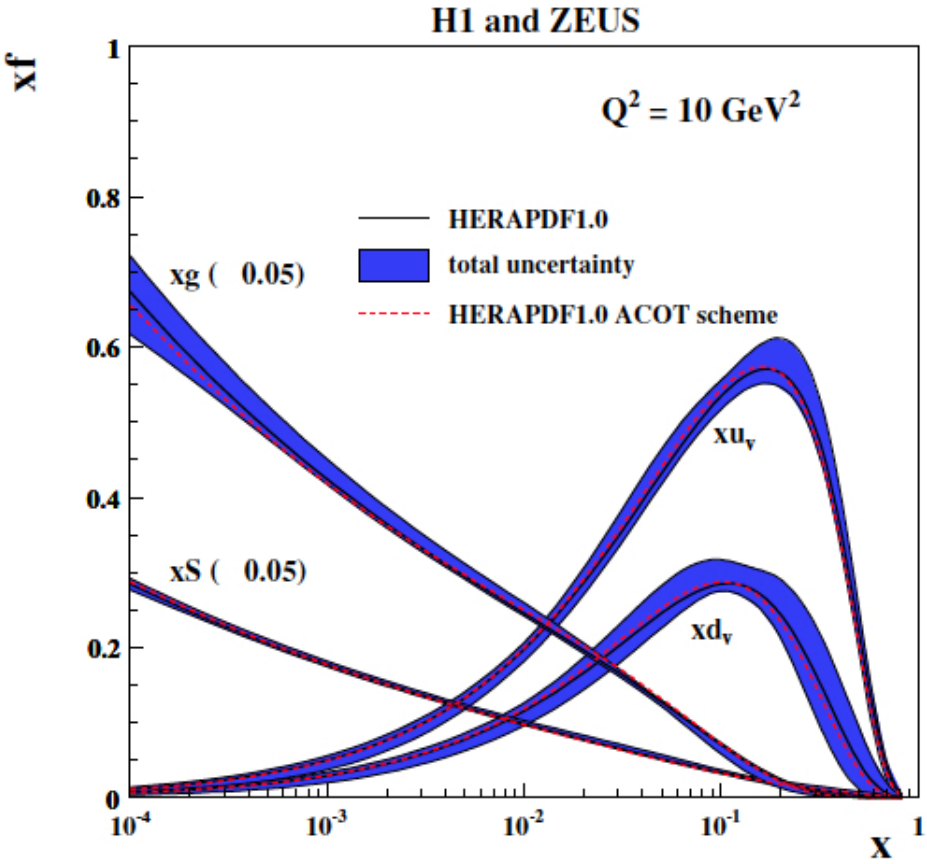

Figure 2–1: Probability distribution functions of different types of partons in the proton multiplied by the proton momentum fraction x, as function of x, at a $Q^2 =$ 10 GeV [24]. The symbols u_v, d_v, S and g represent the distribution functions for the valence up quark, valence down quark, sea quarks and gluons respectively. The gluon and sea quark contributions are scaled down by a factor of 20. The total uncertainties are overlaid as a band.

2.2 Photon Production in Proton-Proton Collisions

In proton-proton collisions, photons can either be produced directly in the hard scattering of two partons (*prompt*) or come from other origins (*non-prompt*) such as light mesons[1] decaying into photons

Examples of Feynman diagrams describing the production of prompt photons are shown in Figure 2–2. The prompt photon production is hereby further classified into *direct* photons and *fragmentation* photons. As shown in Figure 2–2, the direct contribution represents the photon production processes where the photon originated "directly" from the $2 \rightarrow 2$ parton scattering. The fragmentation contribution consists of processes where the final state photon originated from the fragmentation[2] of a final-state parton. At LO the fragmentation process, indicated by the "blob" in Figure 2–2, is included as part of the parton shower (see Section 2.3). The parton shower ensures that color and charge is conserved via soft parton emissions.

In the perturbative QCD expansion describing the photon production, Feynman diagrams depicting reactions with the highest probabilities of occurring are called leading order (LO) diagrams. Diagrams involving one more interaction vertex than

[1] Mesons are a subgroup of hadrons. They consist of a quark-antiquark bound state.

[2] The fragmentation of a parton into a photon corresponds to the situation where the photon momentum is collinear to the momentum of the parton. There are different methods used to deal with the singularity arising from this particular kinematic configuration, including the introduction of a fragmentation function.

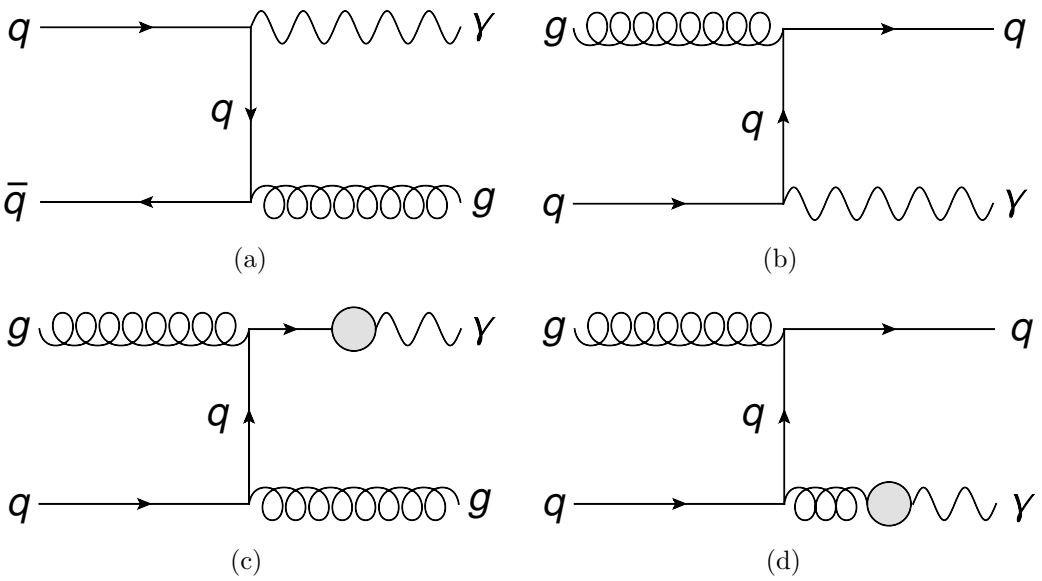

Figure 2–2: Examples of Feynman diagrams of the prompt photon production at the LHC. Diagrams (a) and (b) show examples of the direct, and (c) and (d) of the fragmentation, contributions. On these Feynman diagrams the time axis runs from left to right.

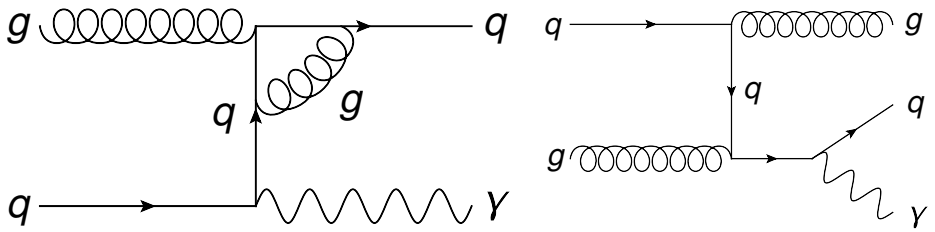

(a) (b)

Figure 2–3: Examples of next-to-leading order (NLO) Feynman diagrams of prompt photon production at the LHC.

LO are called next-to-leading order (NLO) diagrams and have a correspondingly smaller probability of occurrence. Examples of NLO diagrams for the production of prompt photons are presented in Figure 2–3.

The probability for a specific type of interaction to occur is expressed in terms of the cross-section of a process, expressed in units of barn[3] . The photon production cross-section of two incoming partons of a specific type can be calculated using perturbative QCD. The prompt photon production cross-section in proton-proton collisions is obtained by convoluting all the possible parton-level cross-sections with the proton PDFs.

$$\sigma_{AB\to\gamma+X} = \sum_{i,j} \int\int dx_{a_i} f_{a_i/A}(x_{a_i}, \mu_F^2) dx_{b_j} f_{b_j/B}(x_{b_j}, \mu_F^2) \sigma_{a_i b_j \to \gamma+X}(\mu_F^2, \mu_R^2), \quad (2.1)$$

[3] A barn is defined as $10^{-28}\,\mathrm{m}^2$ which corresponds to approximately the cross-sectional area of a uranium nucleus.

where A and B represents the incoming protons, each consisting of partons a_i and b_j. The symbols $f_{a_i/A}$ and $f_{b_i/B}$ represent the two PDFs of the colliding protons. The symbol $\sigma_{a_i b_j \to \gamma + X}$ represents the scattering probability of two partons into a photon (γ) and "anything" else (X). The symbol μ_F represents the factorization scale (units of energy) and reflects the energy boundary between the perturbative and non-perturbative regime. The non-perturbative contribution (i.e. proton PDFs), as already introduced, can be extracted from experimental measurements at fixed Q^2 and evolved to other energy regimes using the DGLAP equations. The parameter μ_R has no physical meaning but is needed to renormalize the calculations of perturbative QCD [19]. Renormalization is a commonly used theoretical concept to treat infinities arising within the calculations and has been tested in quantum electrodynamics [27].

2.3 Parton Shower and Hadronization

As a result of asymptotic freedom and colour confinement the final state gluons and quarks, of the hard scattering of protons, have to be further evolved into hadrons in order to become measurable physical objects and ensure colour and energy conservation. In essence the conservation is achieved by a cascade-like emission of gluons and quarks, of lower and lower energies; a phenomena called the parton shower. The partons produced in this parton shower then form hadrons in a process called hadronization. The dynamics of the parton shower and hadronization processes, as they involve long range non-perturbative QCD, can be combined into empirical fragmentation functions that can be experimentally measured. These fragmentation functions are proportional to the probabilities of producing a hadron from a

given parton. They are measured, similarly to the PDFs, at fixed Q^2 and evolved to different values of energy-momentum transfer using the DGLAP equations.

2.4 Underlying Event and Pile-Up

In addition to the hard scattering process producing a photon, the complete description of a proton-proton collision must also account for the *underlying event* and *pile-up*. The underlying event refers to the description of the remaining "spectator" partons inside the proton, excluding those from the hard scattering process. Collisions from other protons in the same bunch[4] , or proton collisions from a previous bunch crossing contribute to what is called pile-up.

2.5 Measurement of the Prompt Photon Production Cross-Section in Proton-Proton Collisions

In this thesis, the prompt photon production cross-section is measured as a function of the outgoing photon direction and transverse energy (transverse to the plane of the colliding beam). The measurement takes into account detector effects allowing for interpretations and comparisons of the results independent of the ATLAS detector. The photons in this measurement are constrained to transverse energies above 25 GeV and pseudorapidity values of less than 2.37. The measured parton-level cross-section is compared to perturbative QCD calculations at NLO as a test of QCD predictions.

[4] At the LHC protons are grouped together in bunches of approximately 10^{11} protons. More details can be found in Section 3.1.

Since the production cross-section of a physics reaction in proton-proton collisions depends on the content of the proton, cross-section measurements at parton-level can be used to further constrain the PDFs. Based on the high probability to strike a gluon within the proton at the energy regime of the LHC through the gluon induced photon production in proton-proton collisions (see Figure 2–2 and Figure 2–3), the prompt photon cross-section is particularly sensitive to the value of the gluon PDF [28–33]. Therefore, measurements of the photon production cross-section can be used to further constrain possible values of the gluon PDF and its uncertainty. A more precise measurement of the gluon PDF will in turn further reduce uncertainties in the prediction of proton-proton collision outcomes on which most measurements at the LHC rely.

CHAPTER 3
Experimental Environment

This chapter introduces the experimental setup used to perform a measurement of the prompt photon production cross-section. After a brief introduction of the Large Hadron Collider (LHC) [34] and its performance, the ATLAS detector is described with a particular focus on the detector subsystems most relevant for this analysis.

3.1 The Large Hadron Collider

The Large Hadron Collider (LHC) at CERN, the European Organization for Nuclear Research, is currently the world's largest particle accelerator, designed to operate at collision centre-of-mass energies of up to 14 TeV. The LHC is located in an underground tunnel of 27 kilometres in circumference at the Franco-Swiss border near Geneva, Switzerland. It is designed to accelerate and circulate two particle beams in opposite directions by having two parallel beam lines throughout the whole machine. At four different experimental sites along the LHC, the particle beams can be brought into collision. These collision points are occupied by the four main detectors placed at the LHC: ALICE [35], ATLAS [36], CMS [37], and LHCb [38].

The LHC relies on a series of linear and circular particle accelerators making up the injector complex (see Figure 3–1). This complex is capable of injecting protons into the LHC with an energy of 450 GeV. The protons are obtained from hydrogen gas, by removing the electron from the hydrogen atoms using an electric field. The

remaining protons are first accelerated in the linear accelerator (LINAC 2) [39] to an energy of 50 MeV, and then injected into the Booster [40] to be further accelerated to an energy of 1.4 GeV. The protons are next accelerated to an energy of 25 GeV by the Proton Synchrotron (PS) [41] and then up to an energy of 450 GeV by the Super Proton Synchrotron (SPS) [42]. Protons are accelerated in groups (so called bunches) of around 10^{11} protons [34]. It takes approximately 5 minutes to fill each LHC ring with proton bunches[1] and approximately 20 minutes to accelerate them to their final collision energy and prepare the two proton beams for collisions. The opposing proton beams are directed with magnetic fields to intercept at the interaction points. The proton beams remain in collision mode continuously for approximately 20 hours of data taking. During this time, the number of protons per bunch gradually decreases down to a level at which it is more efficient to refill the rings in order to maximize the amount of recorded data (integrated over time). The proton losses are mainly driven by the proton-proton interactions, protons scattering off residual gas molecules in the beam pipes and machine imperfections [44].

Two key parameters defining the operation of a particle accelerator are:

- The maximum centre-of-mass energy of particle collisions ($\sqrt{s}$);
- The instantaneous luminosity, $\mathcal{L}$, defined as [34]

[1] In 2012 a total of 1380 bunches were filled into each ring [43].

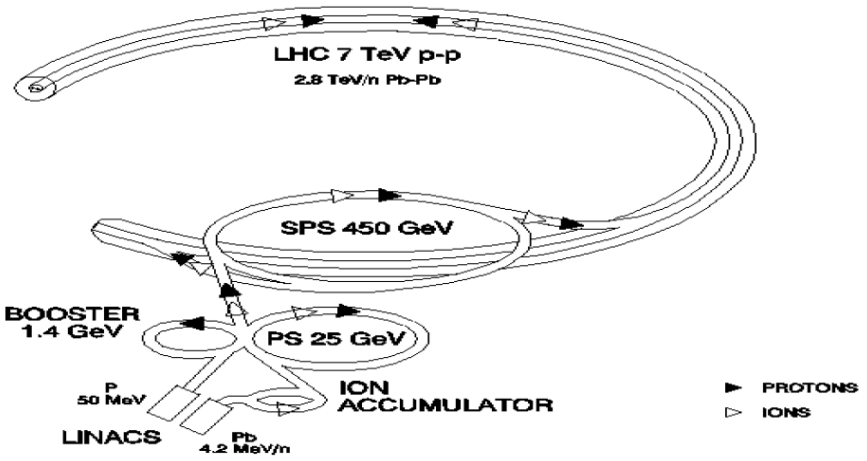

Figure 3–1: Schematic diagram of the CERN particle accelerator complex [34].

$$\mathcal{L} = \frac{f_{\text{rev}} n_b N_1 N_2}{A} \tag{3.1}$$

where f_{rev} is the revolution frequency of the beam, n_b the number of bunches per beam and N_1, N_2 the number of protons in each bunch of the two colliding beams. The cross-sectional area (A) incorporates details of the angle and the size of the beams at the interaction points. The instantaneous luminosity is measured in units of $\text{cm}^{-2}\text{s}^{-1}$.

The rate at which a particular physics process occurs is proportional to the cross-section (σ) of the physics process (measured in units of barns) and the instantaneous luminosity of the accelerator

$$\frac{dN}{dt} = \sigma \mathcal{L}. \tag{3.2}$$

The LHC is designed to achieve a centre-of-mass energy of 14 TeV and a maximum instantaneous luminosity of $10^{34}\,\mathrm{cm}^{-2}\mathrm{s}^{-1}$ for proton-proton collisions[2] .

3.1.1 Running Conditions in 2012

The LHC collided protons at a centre-of-mass energy of 8 TeV from the beginning of April 2012 until December 2012. A maximum of 1380 colliding bunches [43] resulted in maximum instantaneous luminosity of $7.73 \times 10^{33}\,\mathrm{cm}^{-2}\mathrm{s}^{-1}$ [43]. Overall a total time-integrated luminosity of $22.8\,\mathrm{fb}^{-1}$ was delivered to both ATLAS and CMS. The integrated luminosity is a measure of the total number of collisions recorded. Figure 3–2 shows the delivered integrated luminosity for both the 2011[3] and 2012 data taking periods.

As a result of grouping protons into bunches, more than one proton-proton collision can occur when two proton bunches cross at an interaction point. Additional proton collisions coming from the same colliding proton bunches or from neighbouring bunches are generically called pile-up. Figure 3–3 shows the mean number of proton-proton interactions per bunch crossing for the 2011 and 2012 data taking periods. In

[2] The LHC is also capable of colliding heavy ions (lead) at a centre-of-mass energy of 5.5 TeV.

[3] In 2011 the LHC operated at a collision centre-of-mass energy of $\sqrt{s} = 7$ TeV.

2012, an average of approximately 20, and a maximum of 70, interactions occurred per bunch crossing [43].

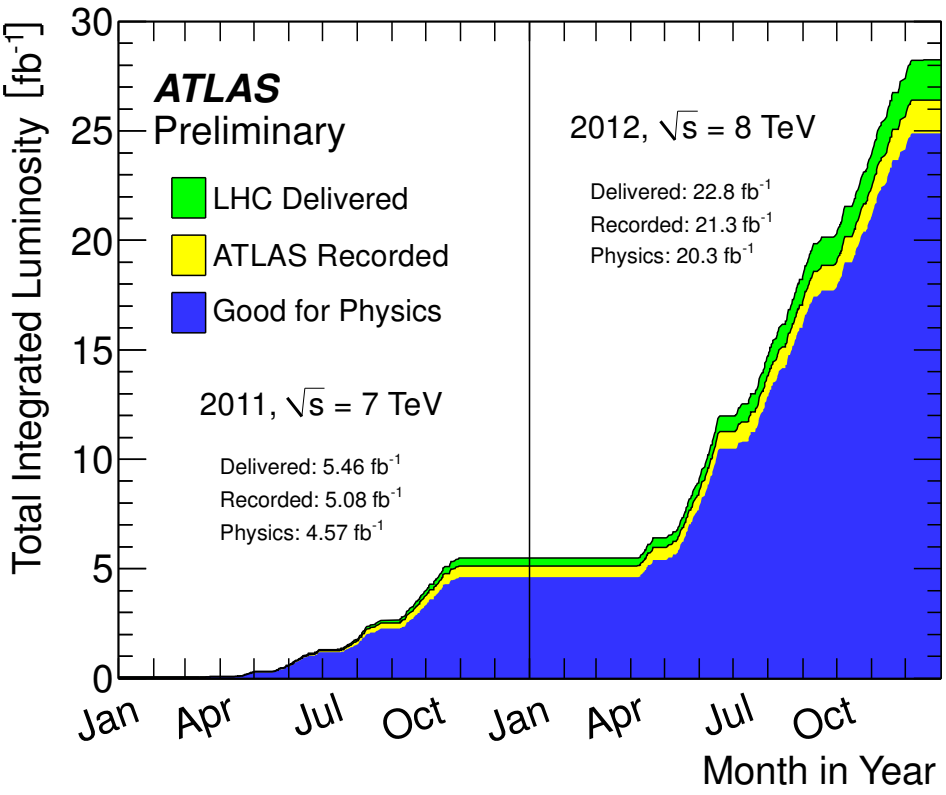

Figure 3–2: Integrated luminosity as a function of time, showing both the 2011 ($\sqrt{s} =$ 7 TeV) and 2012 ($\sqrt{s} = 8$ TeV) data taking periods [45]. The overall integrated luminosity delivered by the LHC to the ATLAS experiment is shown (green) as well as the ATLAS recorded luminosity (yellow) and fraction of the recorded data used for physics analysis (blue).

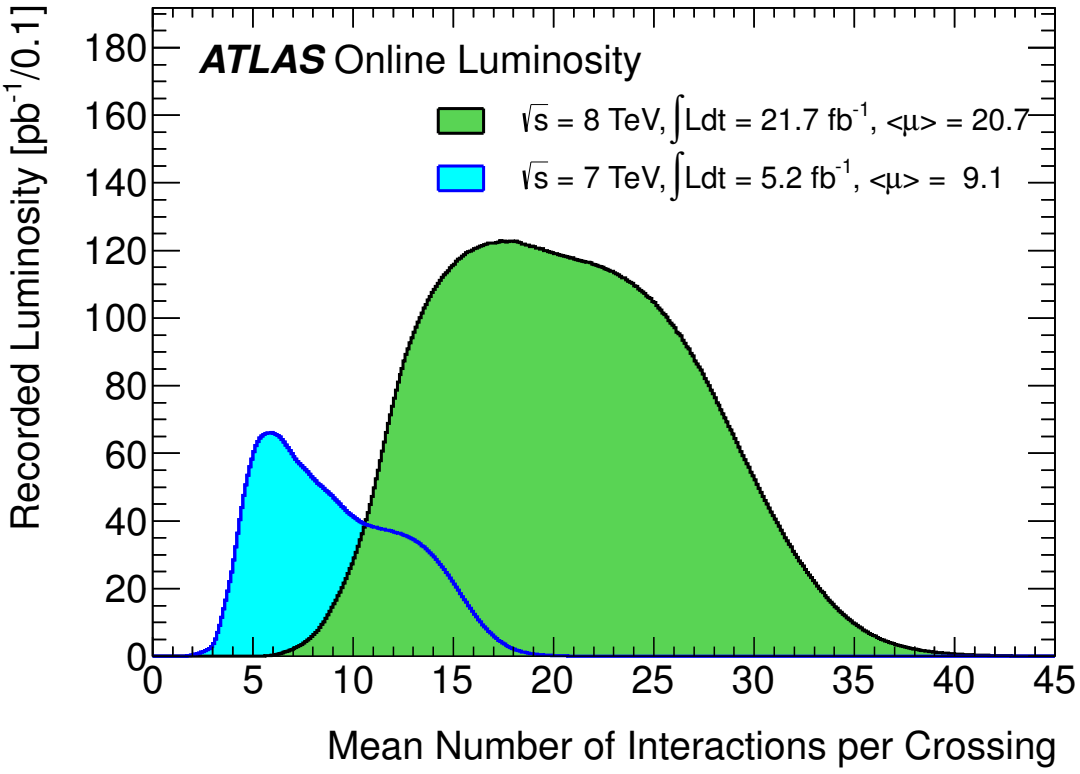

Figure 3–3: Distribution of the mean number of proton-proton interactions per bunch crossing during the 2011 ($\sqrt{s} = 7$ TeV) and 2012 ($\sqrt{s} = 8$ TeV) data-taking periods [45].

3.2 The ATLAS Detector

The ATLAS[4] detector [36] was specifically designed to study high-energy proton-proton collisions produced at the LHC. The ATLAS detector has a length of 44 m, diameter of 25 m and weighs over 7000 tonnes. The goals of the ATLAS experiment are to measure properties of the Higgs boson, test predictions of the Standard Model, and search for the existence of new physics phenomena. In order to achieve these goals, the ATLAS detector was designed to have the ability to measure the energy, direction and identify the type of all particles produced in proton-proton collisions over a wide range of particle energies. The following sections describe the ATLAS detector with particular emphasis on the parts most relevant for the work presented in this thesis.

3.2.1 ATLAS Geometry

The ATLAS detector is forward-backward symmetric about the interaction point. It is divided into a central barrel and two end-cap regions. The barrel is made of an inner tracking detector, surrounded by a superconducting solenoid, electromagnetic and hadronic calorimeters. The muon spectrometer, with its three large superconducting toroid magnets (one barrel and two end-cap magnets), surrounds the calorimeters. A schematic diagram of the ATLAS detector is shown in Figure 3–4. The coordinate system of the detector is defined with its origin located at the nominal proton-proton interaction point (centre of the detector), the z-axis points counterclockwise along

[4] A Toroidal LHC Apparatus.

the LHC ring (looking down at the ring from the surface), and the x-y plane is defined to be transverse to the beam direction. The coordinate system is chosen to be right-handed, with the positive x-axis pointing towards the centre of the LHC ring and the positive y-axis pointing away from the centre of the earth. In addition, the azimuthal angle ϕ is defined as the angle in the x-y plane and the polar angle θ, as the angle with respect to the z-axis. The pseudorapidity, defined as $\eta = -\ln\left(\tan\left(\frac{\theta}{2}\right)\right)$, is commonly used to describe hadron-hadron collisions. This quantity is useful since the particle flux from inelastic collisions is approximately constant in units of pseudorapidity[5] .

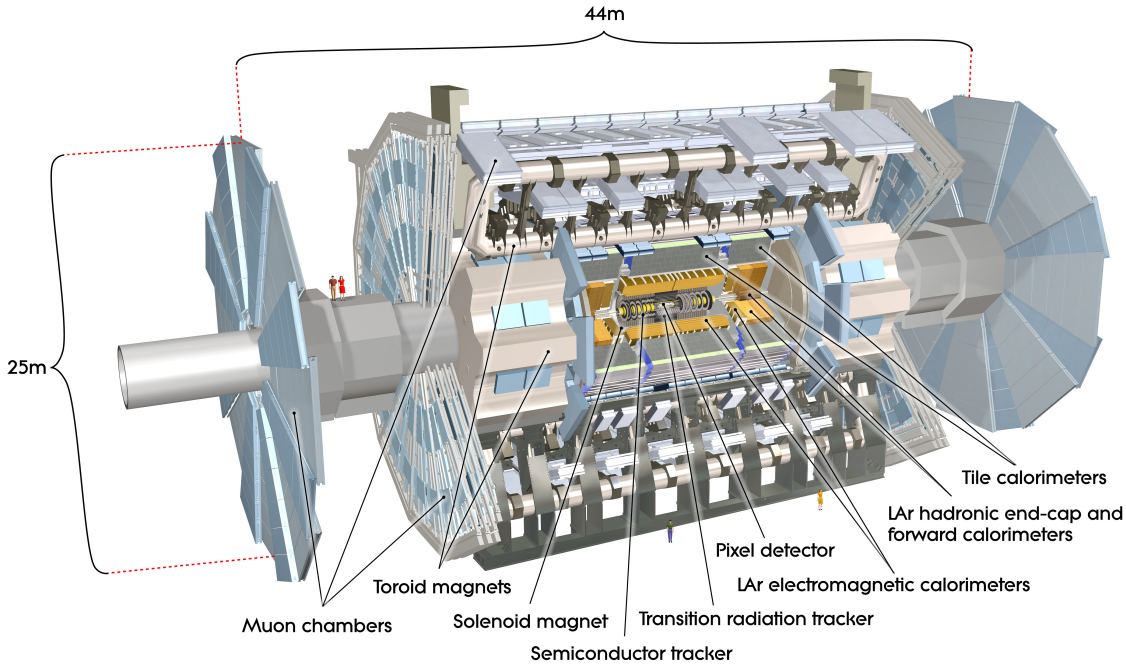

Figure 3–4: Cutaway drawing of the ATLAS detector [36].

[5] The particle flux is constant as a function of rapidity ($y = \frac{1}{2}\ln\left(\left(\frac{E+p_Z}{E-p_Z}\right)\right)$) and in the limit of massless particles, rapidity and pseudorapidity are equivalent.

3.2.2 Inner Detector

The inner detector [46] is the part of ATLAS closest to the beam pipe and the interaction point. It is designed to measure the trajectories (tracks) of electromagnetically charged particles. Tracks are reconstructed from precisely measured spatial position of small energy deposits (hits), left by electromagnetically charged particles as they traverse the inner detector. Based on the track bending imposed by the strong magnetic field of the superconducting solenoid of 2 T, the momentum of electromagnetically charged particles can be measured. In addition, the inner detector allows to reconstruct the position of a vertex[6] down to the µm range.

The inner detector is composed of the following three subsystems. The subsystems make it possible to adjust the design and materials to the different available volume and radiation conditions[7] :

- The innermost subsystem of the inner detector is the pixel detector [47]. The central part (barrel) consists of three layers placed at increasing radii. In addition, three end-cap discs are placed on each side of the barrel increasing the pseudorapidity coverage from $|\eta| < 1.9$ to $|\eta| < 2.5$. The sensors for the

[6] A vertex is a three-dimensional location where two or more reconstructed tracks appear to originate from.

[7] Radiation hardness is a substantial criteria for the material and technology used in ATLAS since the detector is build to last for decades of operation. The high particle fluxes, in particular close to the beam pipe and in the forward direction, require detectors in those regions to be able to function under high instantaneous and integrated doses of radiation.

pixel detector are made of 1,744 thin silicon layers, each divided into 47,323 pixels of 50 μm by 400 μm. This leads to about 80.4 million readout channels and a spatial resolution in $R - \phi$ of 10 μm and 115 μm in the z-direction [36].

- The Semi-Conductor Tracker [36] (SCT) just outside the pixel detector is also divided into a barrel (four layers) and end-cap (each consisting of nine disks) subsystems. The end-caps extend the pseudorapidity coverage of the barrel sector from $|\eta| < 1.1$ to $|\eta| < 2.5$. The SCT utilizes 15,912 silicon sensors, each composed of a collection of 768 active strips, leading to a total of over 6 million readout channels. The strips are 12 cm in length, with an average pitch of 80 μm. They are arranged in modules of two strips on the top and two on the bottom side, with a small relative stereo angle of about 40 mrad between the two sides. This allows for a spatial resolution per module of 17 μm in $R - \phi$ and 580 μm in the z-direction [36].

- The last part of the inner detector installed at a larger radius is the Transition Radiation Tracker [48] (TRT). It consists of polyamide drift tubes (straws) of 4 mm in diameter, covering the pseudorapidity range of $|\eta| < 2.0$. Each of these straws is filled with a gas mixture (70 % Xenon, 27 % CO_2 and 3 % O_2 [49]) and has a tungsten anode wire running through its centre. The TRT serves two purposes: firstly it measures in each straw the ionization of the gas by a charged particle passing through the straw, thereby providing a position measurement; secondly it distinguishes between electrons and hadrons. The latter is achieved by measuring transition radiation photons. Transition radiation photons are created as an incident charged particle traverses the interface

of different dielectric properties. The number of transition radiation photons emitted is proportional to the relativistic gamma factor of the charged particle, which in turn is inversely proportional to the mass of the particle ($\gamma = E/m$). Therefore, electrons of the same energy as a hadron will emit significantly more transition radiation photons. Plastic fibres are placed between the cylindrical straws (into the existing gaps), enhancing the number of transition radiation photons generated. Ionization signals from a charged particle are distinguished from transition radiation photon ionization signals using two different signal thresholds. Transition radiation photons deposit a larger amount of energy in the straws compared to the amount deposited by a charged particle.

The TRT consists of a barrel and two end-cap sections, with its tubes arranged parallel to the beam line in the barrel, and tubes extending radially around the beam line in the end-cap sections. The TRT has approximately 351,000 readout channels and a $R - \phi$ spatial resolution of 130 µm per straw [36].

A computer generated drawing of the inner detector is shown in Figure 3–5.

3.2.3 Calorimeter System

The electromagnetic and hadronic sampling calorimeters (split into barrel and end-cap sections) [50] are located further away from the interaction region. The general concept of a calorimeter is to measure the energy of a particle of interest via total absorption within the calorimeter material. In addition, measurements of a particle position are generally obtained by segmenting the calorimeter. A sampling calorimeter divides the absorption and energy measurement by having alternating layers of

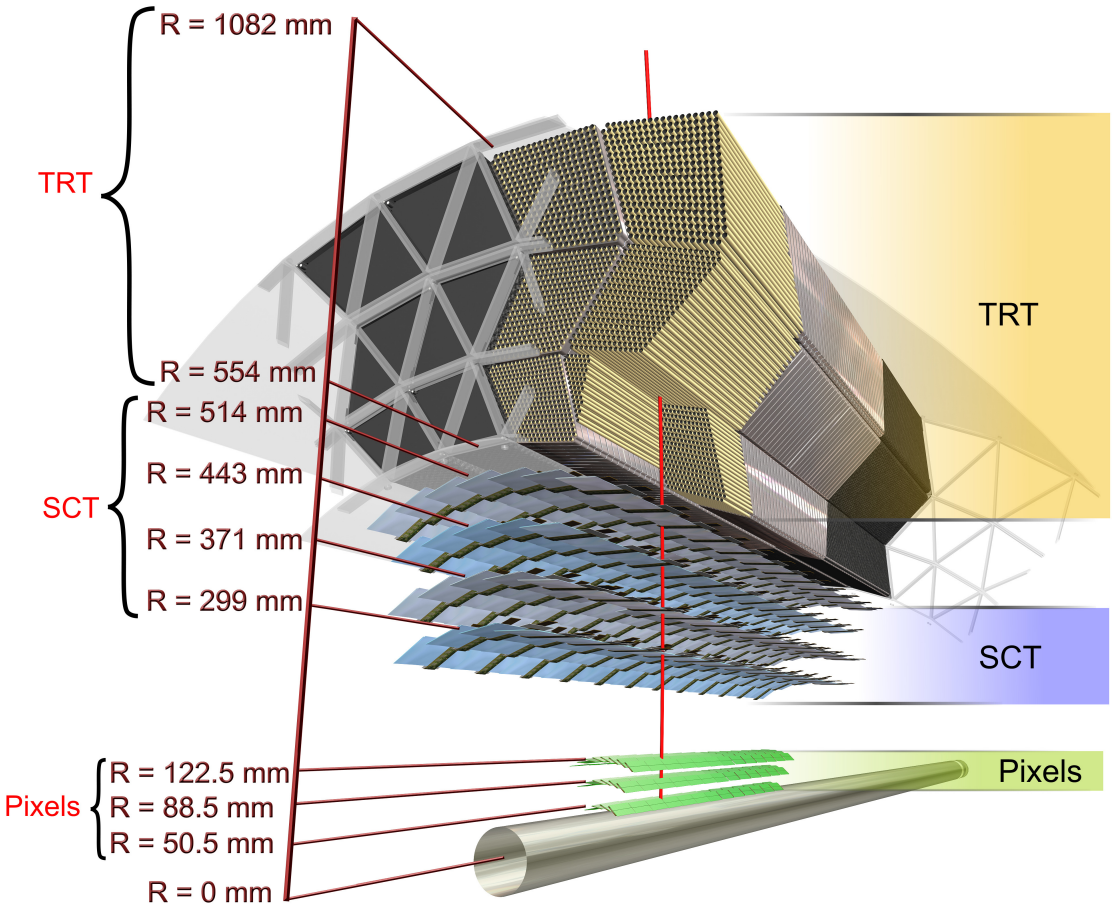

Figure 3–5: Drawing showing the sensors and structural elements of the inner detector in the barrel region [36]. The inner detector is composed of the Pixel detector, Semi-Conductor Tracker (SCT) and Transition Radiation Tracker (TRT). The red line represents a charged particle with a transverse momentum of 10 GeV traversing the inner detector at $\eta = 0.3$.

active and dense absorber materials. In this case, the energy measurement, which only corresponds to part of the total energy deposited in the calorimeter, must be corrected offline using calibration data. Both hadronic and electromagnetic particles interact with the dense material of the calorimeter, producing a cascade of secondary particles with decreasing energy, spread around the direction of the initial incoming particle. The lateral size and depth of penetration of these so called *showers* is different for hadrons compared to electrons and photons. It is generally quantified by the (larger) hadronic interaction length[8] (λ_I) and the electromagnetic radiation length[9] (X_0). Therefore, the hadronic calorimeter surrounds the electromagnetic calorimeter, as seen in a cutaway view of the entire calorimeter system shown in Figure 3–6.

The electromagnetic calorimetry uses Liquid Argon (LAr) as the active medium and lead as the absorber material. The lead plates are accordion shaped and stacked together with gaps for the LAr. This geometry makes it possible to place readout electronics at small and large radii of the structure, ensuring a full coverage in the azimuthal angle ϕ. The electromagnetic calorimeter is designed to measure the total energy of electrons and photons, making it, combined with the presence (electrons)

[8] The mean path length of particles between two inelastic interactions. For commonly used materials such as lead, steel or copper, one nuclear interaction length represents a thickness of 17.6 cm, 16.8 cm and 15.3 cm respectively [3].

[9] The mean distance over which a high energy electron loses 1/e of its initial energy via bremsstrahlung. For commonly used materials such as lead, steel or copper one radiation length represents a thickness of 0.6 cm, 1.8 cm and 1.4 cm respectively [3].

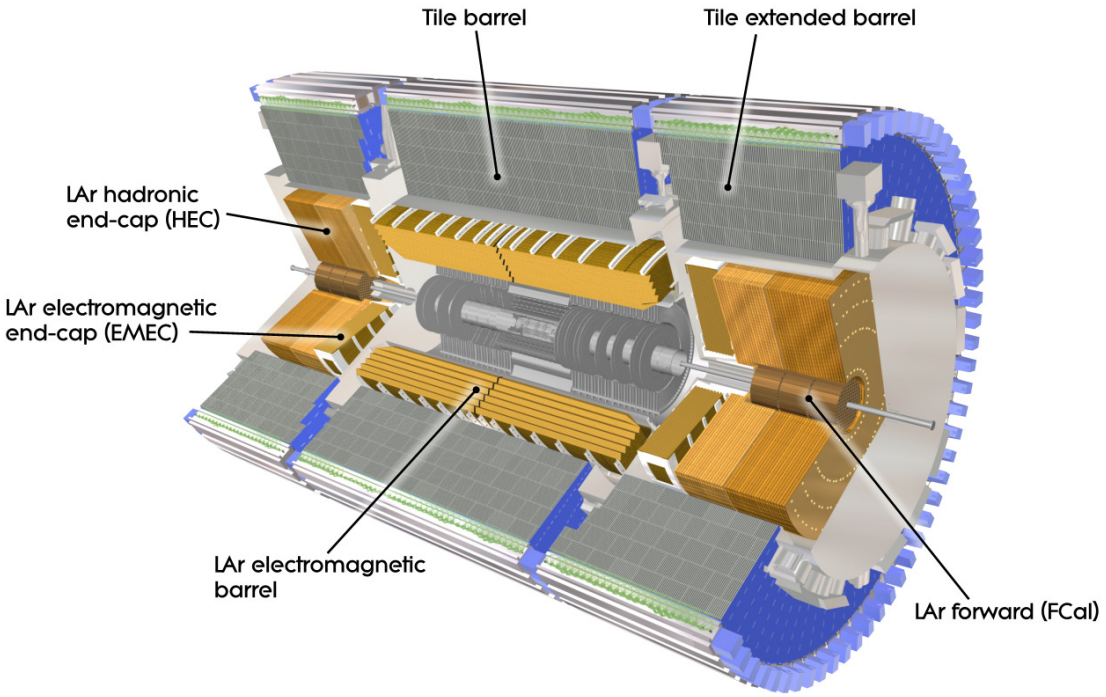

Figure 3–6: Cutaway drawing of the ATLAS calorimeter system [36].

or absence (photons) of inner detector tracking information, the most important detector system for the measurement presented in this thesis. The electromagnetic calorimeter is made of three layers, finely granulated in $\eta - \phi$, covering the same region $|\eta| < 2.5$ as the inner detector and two layers covering the more forward regions of $2.5 \leq |\eta| < 3.2$.

The accordion structure of the barrel module shown in Figure 3–7 is oriented radially and normal to the beam line with the "waves" of the accordion structure pointing radially outwards. For the end-cap modules, the lead plates are oriented similarly but with the "waves" of the accordion structure pointing along the direction of the beam line. The thickness and the bending angle of the lead plates depends on the radial distance from the beam line and the pseudorapidity region (calculated with respect to the geometrical centre of the detector). Therefore, the thickness ratio of active and absorber material is uniform in ϕ, but varies as a function of η. As a result, the energy resolution is kept uniform as a function of ϕ and varies as a function of η. A schematic view of one of the 32 barrel modules is shown in Figure 3–7, showing the overall size of each layer, their radiation lengths, and cell sizes. The overall thickness of the electromagnetic calorimeter in the barrel region varies as a function of η with a minimum value of $25\,X_0$, and then increases in the end-cap regions to around $35 - 40\,X_0$. This ensures that the shower induced by electrons and photons up to energy of several TeV are either fully absorbed or only have minimal leakage outside of the volume of the electromagnetic calorimeter.

The cell granularity shown in Figure 3–7 is kept constant as a function of ϕ and η for the whole three layer region of the barrel electromagnetic calorimeter. The

first layer is made of narrow strip cells providing a precise position measurement in η. This fine η granularity provides the ability to distinguish between a single photon and photon pairs originating from the decay of neutral mesons (π^0, η). The second layer is physically the largest in volume and absorbs the main part of the electromagnetic shower. The third layer has a slightly coarser granularity than the second layer. Its main purpose is to measure the energy of showers originating from the highest energy electrons/photons potentially leaking out of the electromagnetic calorimeter. A further separate thin layer of LAr (11mm in depth) with a readout electrode granularity of 0.025×0.1 ($\Delta\eta \times \Delta\phi$) is added in front of the electromagnetic calorimeter in the region $|\eta| < 1.52$ (barrel). This additional layer is designed to measure the energy loss of particles prior to entering the electromagnetic calorimeter. Overall, the design of the electromagnetic calorimeter provides an energy resolution of $\frac{\sigma_E}{E} = \frac{10\%}{\sqrt{E}} \oplus 0.7\%$[10] [36], an η position resolution of 3×10^{-4} [36], and a ϕ position resolution between 5×10^{-4} and 2×10^{-3} radians [36] (depending on the amount of material in front of the electromagnetic calorimeter).

The Hadronic Calorimeter, designed to measure the energy of hadrons by total absorption, is used in the scope of this analysis as a discriminator for photons that are likely not produced in the main interaction but rather originate from hadronic decays or within showers.

[10] $\oplus$ indicates that the two terms have to be added in quadrature.

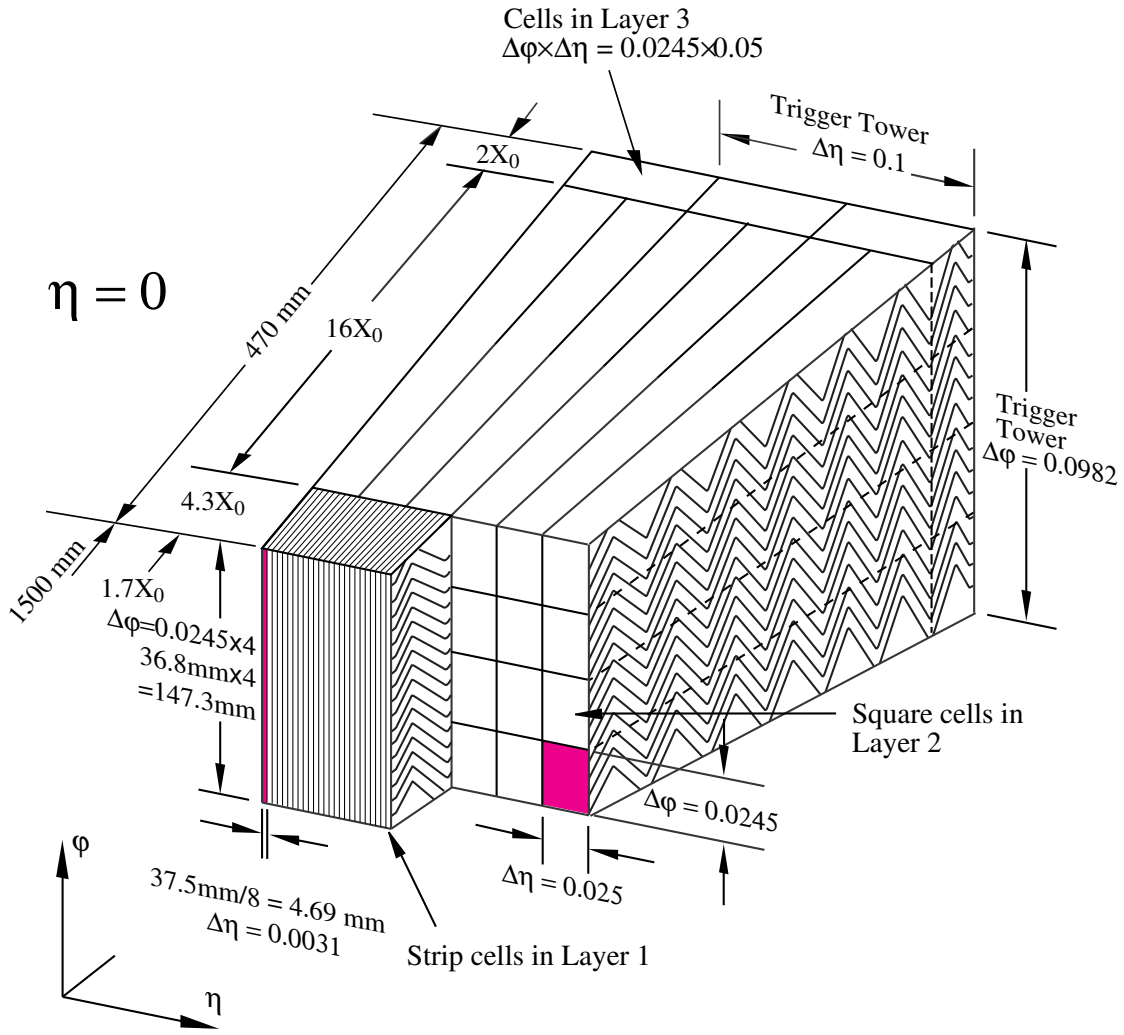

Figure 3–7: Sketch of an electromagnetic calorimeter barrel module showing the accordion structure [36]. Particles originating from the interaction region enter the calorimeter in Layer 1.

For the same particle energy a hadron penetrates much further in matter than an electron or photon before it starts to shower. Furthermore, a hadron initiated shower is generally larger in size, as secondary particles produced in the hadron shower can be hadrons, electrons and photons, as well as muons and neutrinos. In addition, excitation and splitting of the atomic nuclei can occur (sometimes below the sensitive energy threshold of the calorimeter). Therefore, unlike an electromagnetic shower, some fraction of the total energy of the incident hadron escapes the measurement of the hadronic calorimeter. Due to this difference in the showering process, the response of a calorimeter to an incident electron/photon versus the response to an incident hadron is typically different. A calorimeter with a response ratio of electron/photon to hadron (e/h) greater than one is said to be non-compensating. The measured energy in a non-compensating calorimeter therefore needs to be further corrected in order to be able to reconstruct the true energy of the original incident particle. Specific software based calibration procedures are developed and used within the ATLAS collaboration in order to correct the measured energy of hadrons. The hadronic calorimeter is divided into a Tile Calorimeter in the barrel region, Hadronic End-Caps (HEC) and the Forward Calorimeter (FCal), covering all together the region $|\eta| < 4.9$.

The Tile Calorimeter covers the pseudorapidity region of $|\eta| < 1.7$ and is subdivided into a central barrel and two extended barrel modules. It is made of steel absorber plates and scintillating tiles as the active material. Steel has a shorter interaction length than lead and is therefore more suitable for a hadronic calorimeter.

The thickness of the Tile Calorimeter (including all its service and support structures) corresponds to an interaction length of $\lambda = 9.7$ (at $\eta = 0$). The scintillator tiles are oriented radially and normal to the beam line and are stacked into modules, as shown in Figure 3–8.

The Hadronic End-Caps use liquid argon as active material, to provide the required radiation hardness in this region that sees a higher particle flux. In order to reach the required interaction length to contain hadronic showers within a limited amount of space, copper is used as the absorber material, which has an even shorter λ than steel. The Hadronic end-caps absorber material corresponds to about 12 interaction lengths allowing for enough thickness in terms of interaction length to be able to contain the shower of hadronic particles. The Hadronic end-cap is made of two wheels in each end-cap: a front wheel and a rear wheel. Each wheel is made out of 32 identical wedge-shaped modules with a layer structure of active and absorber material. The design energy resolution for the Tile Calorimeter and the HEC is $\frac{\sigma_E}{E} = \frac{50\%}{\sqrt{E}} \oplus 3\%$ [36].

The Forward Calorimeter (FCal) provides additional angular coverage in the forward region, which is important for the measurement of possible missing energy in a collision. Due to very high particle fluxes, the Forward Calorimeter has to be made out of radiation hard material. It consists of a metal[11] matrix (absorber) with tubular electrodes running through its holes in the direction parallel to the beam

[11] Copper in the first module, tungsten in the second and third modules

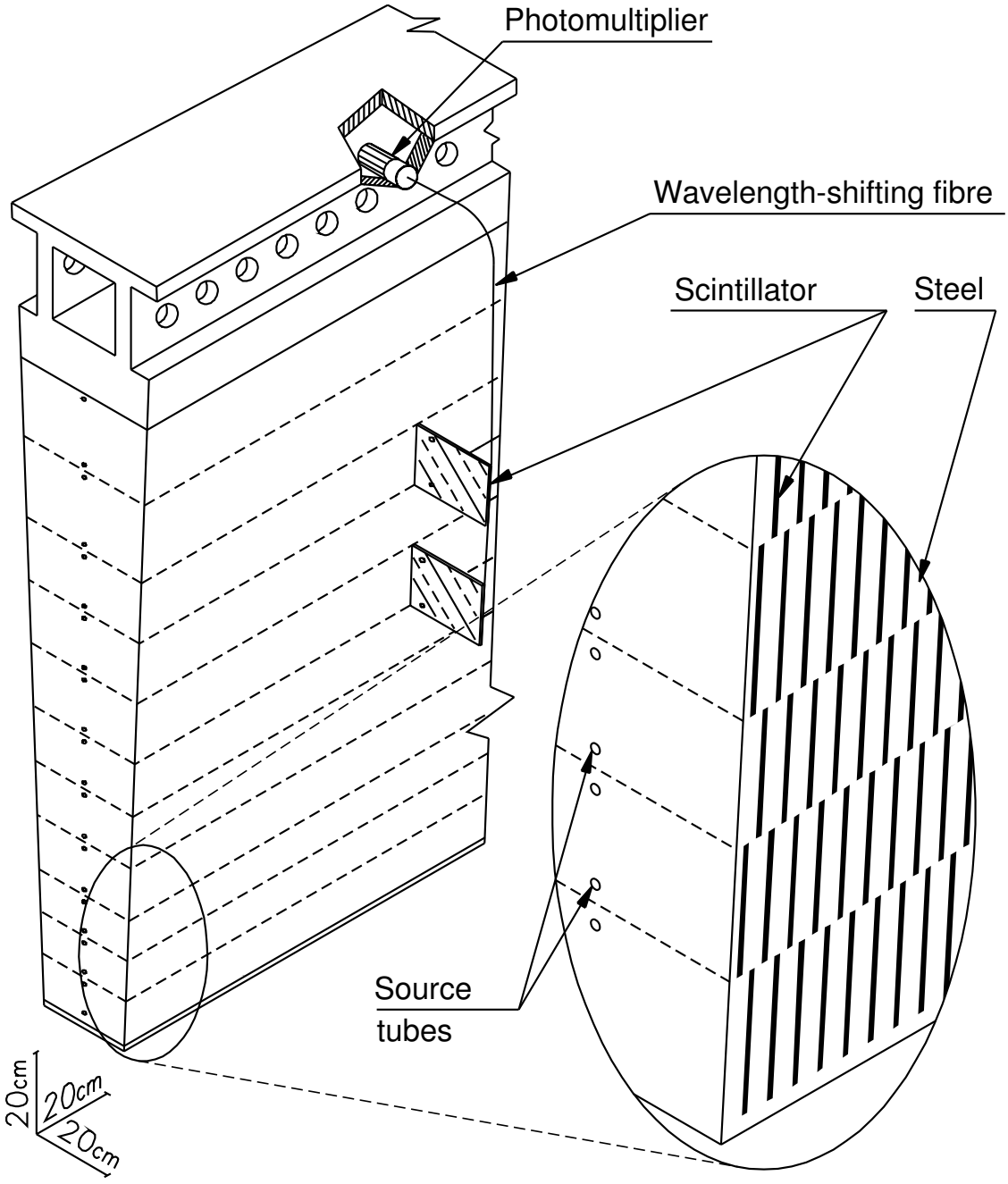

Figure 3–8: Schematic drawing of a tile calorimeter module in the barrel part of the ATLAS hadronic calorimeter [36].

pipe. The electrodes are composed of tubes (anodes) surrounding rods (cathodes) with LAr as the active material filled into the remaining gap.

3.2.4 Muon System

The muon system [51] is the outermost detector system and is made of high precision tracking chambers and different type of triggering chambers. The magnetic bending of charged muons that reach the muon system is provided by the large barrel toroids and two smaller end-cap magnets located at the end of the barrel region. The muon system covers a pseudorapidity range of $|\eta| < 2.7$ with a transition region $1.4 < |\eta| < 1.6$ where the magnetic fields between the toroid barrel and end-caps overlap. The trigger system is composed of "resistive plate chambers" [51] in the barrel region and "thin gap chambers" [51] in the end-cap regions. Precise position measurements are provided by "monitored drift tubes" [51] and "cathode strip chambers" [51]. A drawing of the position of the different parts of the muon system within the ATLAS detector is shown in Figure 3–9.

3.2.5 Trigger

The high bunch crossing rate of 40 MHz, with approximately 20 interactions per bunch crossing at the LHC, requires a highly selective trigger system for ATLAS. Trigger in this context refers to the decision making process of whether to record or reject the information recorded from a given bunch crossing called an *event*. The ATLAS trigger system [36] is split into a hardware-based first Level (L1) and two software-based systems, the Level 2 (L2) and Event Filter (EF). Together they are designed to reduce the high event rate (40 MHz) to a manageable recording rate of

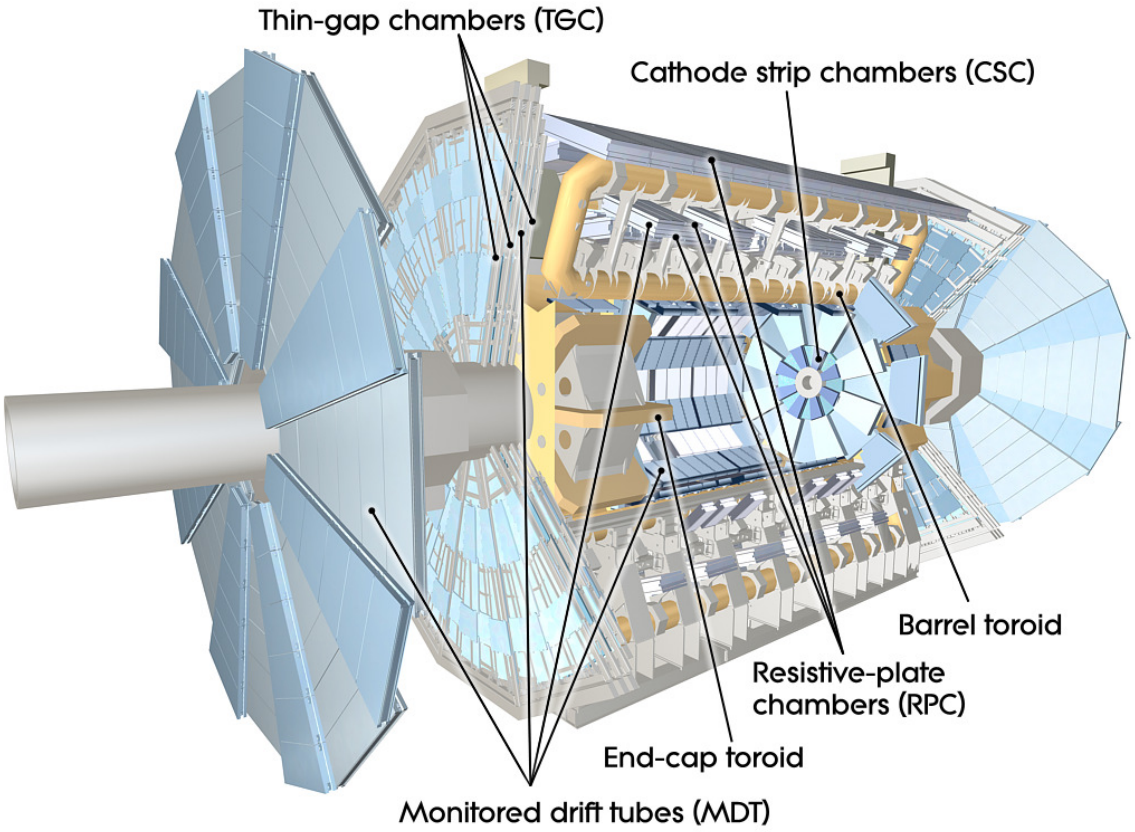

Figure 3–9: Cutaway view of the ATLAS muon system [36].

less than 1 kHz. Recorded events have a size of about 1.5 MB (mega byte), leading to a data stream (recorded to permanent storage) of roughly 1 GB per second during regular data taking. The three systems build upon one another's decision, reducing the overall rate in steps. In the following section, the photon trigger setup for these three levels is introduced.

- **The L1 Photon Trigger** [52] is based on the position and energy measurements of the electromagnetic calorimeter. The trigger decision is formed for a set of fixed transverse energy thresholds following a coarse scan of the entire calorimeter. This scan uses a reduced granularity of the calorimeter information to ensure that a L1 trigger decision is formed within less than 2.5 µs (based on the 40 MHz input rate). The individual electromagnetic calorimeter cells (see Figure 3–7) are grouped into *trigger towers* of an approximate size of 0.1×0.1 in $\Delta\eta \times \Delta\phi$. The energy of all cells within these trigger towers is summed up. The scan uses a sliding window of size 4×4 trigger towers to locate local maxima of energy depositions (in the following referred to as regions of interest). The energy sum of the trigger towers in the core region (2×2 trigger towers) around a local energy maximum is compared to the set of predefined transverse energy[12] thresholds of the L1 trigger. The η and ϕ position of all

[12] The transverse energy is calculated from the position and the energy of the core region using $E_{\mathrm{T}} = |\vec{E}|/\cosh(\eta)$.

regions of interests that satisfy at least one of the predefined minimum transverse energy threshold requirements is passed on to the L2 trigger for further processing of the event information.

- **The L2 Photon Trigger** [52] uses an algorithm to build cluster(s) of deposited energy within each region of interest found by the L1 trigger. A cluster consists in a region of 3×7[13] cells in $\Delta\eta \times \Delta\phi$ of the second layer of the electromagnetic calorimeter. It is centred around the calorimeter cell with the highest measured value of deposited energy. The cluster energy is defined as the sum of energy measured by all cells belonging to the cluster in the second layer of the calorimeter. The cluster position is determined as the energy weighted position of the cluster cells. The set of predefined transverse energy thresholds of the L2 photon triggers are applied to the transverse energy of the cluster. In addition, information from the inner detector is used to build tracks from the measured space points (limited to the regions of interest). These tracks are used to distinguish between electrons and photons as photons are electrically neutral particles and do not produce a track in the inner detector. Additional cluster quality criteria outlined in Reference [52] are applied.

- **The EF Photon Trigger** [52] is the final trigger selection. For this selection, the entire detector information is available. Reconstruction algorithms nearly

[13] 3×7 cells in the barrel ($|\eta| < 1.4$) and of 5×5 cells in the end-cap ($1.4 < |\eta| < 2.47$).

identical to those used in offline analysis are used to reconstruct photons. Photons reconstructed by the EF are required to satisfy at least one of a predefined set of transverse energy thresholds.

3.3 Data and MC Samples

The data and simulation samples used for the measurement presented in this thesis are described in this section. Simulation samples are used to calculate various correction factors required for the cross-section measurement that cannot be obtained using only data. NLO calculations of the inclusive photon cross-section are compared with the measurement to assess the level of agreement between perturbative QCD predictions and data.

3.3.1 Data Sample

The data considered for offline analysis are required to have been recorded while both the ATLAS detector and LHC were operating in nominal conditions. Out of the total recorded integrated luminosity of $21.3\,\text{fb}^{-1}$, a total of $20.2\,\text{fb}^{-1}$of data were collected under nominal data taking conditions and are used in the measurement presented in this thesis.

3.3.2 Leading-order MC samples

Two well established leading-order (LO) event generators (`PYTHIA` [53] and `SHERPA` [54]) are used to generate MC event samples of the photon production at the LHC at a centre-of-mass energy of 8 TeV. Both generators can be interfaced with a full

simulation of the ATLAS detector. This allows for direct comparisons of data and MC quantities and distributions.

- PYTHIA is perhaps the most commonly used LO event generator for collider physics and is capable of generating a wide range of event topologies arising from the Standard Model or various models of new physics. It is a parton shower Monte Carlo program. Events generated with PYTHIA are run through a simulation of the ATLAS detector. This simulation of the ATLAS detector, including the conversion of generated events into detector signals, is performed using GEANT4 [55]. The PYTHIA event generation is done using the CTEQ6L1 [56] parton distribution functions and includes the simulation of QED initial and final state radiation. The modelling of the hadronization is based on the Lund string model [57] and the simulation of the underlying event uses a special ATLAS tune based on the multiple parton interaction [58] (MPI) model. The LO direct contribution of the prompt photon production is fully included in the main matrix element calculation, whereas the fragmentation contribution is modelled as part of the final state radiation process.

- SHERPA is also a LO parton shower event generator widely used to simulate a large variety of physics processes. It can be fully linked to the GEANT4 detector simulation. It is used in this analysis as a second independent prediction to quantify uncertainties. A matrix element calculation is used to model all possible LO direct photon production processes. SHERPA, unlike PYTHIA, accounts for the fragmentation contribution to photon production in the parton

showering process of the simulation event generation. The SHERPA event simulation includes QED initial and final state radiation. Events are generated using the CT10 [59] parton distribution functions. The underlying event is modelled using the recommended parameter tune provided by the SHERPA authors[14] . Finally, hadronization is modelled using a modified version of the cluster model [60].

For both event generators a MC event weight is applied in order to normalize the total number of events simulated to the predicted cross-section. The weight is defined as

$$\mathrm{w_{MC}} = \frac{\sigma}{N_{\mathrm{entries}}}, \tag{3.3}$$

where σ is the calculated cross-section for the process and N_{entries} is the total number of generated events.

The entire photon E_{T} spectrum is created using simulated event samples for which different minimum $E_{\mathrm{T}}^{\gamma,\mathrm{min}}$ cuts are applied at the simulation stage. This procedure reduces significantly the overall processing time for the event generation, while maintaining high statistics at high E_{T}^{γ}. In order to avoid overlap between these simulation samples and to ensure that the E_{T}^{γ} spectrum is fully populated, event samples are

[14] This tune is the nominal tune of the SHERPA software package [54].

combined by defining exclusive E_{T}^{γ} regions for each of these samples. The details of the total number of generated events, the sample cross-section, the generator $E_{\mathrm{T}}^{\gamma,\mathrm{min}}$ cut, and its exclusive E_{T}^{γ} range are listed in Table 3–1. The minimum photon transverse energy requirement ($E_{\mathrm{T}}^{\gamma,\mathrm{min}}$) for each simulated sample is chosen to be well below the corresponding E_{T}^{γ} range of the measurement in order to ensure that all possible contributions to the cross-section within the given E_{T}^{γ} range are included in the simulated sample. The $E_{\mathrm{T}}^{\gamma,\mathrm{min}}$ values were chosen such that the ratio of the predicted cross-section within a E_{T}^{γ} measurement range from a specific sample and the sample with the next highest $E_{\mathrm{T}}^{\gamma,\mathrm{min}}$ requirement was equals to unity within statistical uncertainties.

3.3.3 Next-to-Leading Order MC sample

In addition to the LO MC samples described above, `JETPHOX` [61], a next-to-leading (NLO) order Monte Carlo (MC) generator, is used to compare the measured photon production cross-section to NLO predictions obtained from perturbative QCD using different types of parton distribution functions. `JETPHOX` is a well established NLO generator for photon processes and has shown good agreement with previous results of the prompt photon cross-section measurements [5–11, 62]. `JETPHOX` is capable of calculating the double-differential inclusive prompt photon cross-section $d^2\sigma/(dE_{\mathrm{T}}^{\gamma}d\eta^{\gamma})$ at parton (also called truth) level (before hadronization and parton showering). It can be interfaced with different sets of PDFs, to allow the possibility to study the sensitivity of experimental results to different choices of PDFs. The nominal PDF used with `JETPHOX` for this analysis is CT10. `JETPHOX` is capable of

Monte Carlo	N_{events}	σ_{MC} [nb]	$E_{\text{T}}^{\gamma,\text{min}}$ Generator [GeV]	E_{T}^{γ} range [GeV]
PYTHIA	3M	$2.9{\cdot}10^{02}$	17	$20-55$
	3M	$2.4{\cdot}10^{01}$	35	$55-105$
	6M	2.0	70	$105-200$
	2M	$1.2{\cdot}10^{-01}$	140	$200-400$
	1M	$4.8{\cdot}10^{-03}$	280	$400-650$
	1M	$2.1{\cdot}10^{-04}$	500	$650-1100$
	0.1M	$9.4{\cdot}10^{-06}$	800	$1100-1500$
SHERPA	10M	$3.9{\cdot}10^{02}$	15	$20-55$
	10M	$2.4{\cdot}10^{01}$	35	$50-100$
	5.5M	2.2	70	$100-200$
	2.5M	$1.4{\cdot}10^{-01}$	140	$200-400$
	1M	$6.0{\cdot}10^{-03}$	280	$400-650$
	1M	$2.8{\cdot}10^{-04}$	500	$650-1100$
	0.1M	$1.3{\cdot}10^{-05}$	800	$1100-1500$

Table 3–1: List of simulation samples used in this analysis to describe the inclusive prompt photon production in proton-proton collisions. For each sample, the number of events generated (N_{events}), the cross-section of the process calculated for the given phase space (σ_{MC}) and the minimum transverse photon energy required at parton level ($E_{\text{T}}^{\gamma,\text{min}}$) are shown. The rightmost column shows the reconstructed photon transverse energy range for which each sample is used.

including the transverse isolation energy (explained in Section 4.3.4) at NLO and has the flexibility of selecting an E_{T}^{γ}-dependent cut value.

CHAPTER 4
Event and Photon Selection

In this chapter the criteria used to identify photons and select events are introduced. A definition of the region of phase space for which the cross-section is measured is given at the end of the chapter.

4.1 Event Preselection

Only events recorded while the whole ATLAS detector was operational are considered in this analysis. The ATLAS data quality group provides a list of "good" data to be used in analyses. This list is based on all available monitoring information from the detector subsystems and readout electronics, and incorporates detector problems identified after the data was recorded. Data is either identified as "good" or "bad" for data analyses in units of one minute of data taking, which is called a "Luminosity block". A total integrated luminosity of $20.3\,\mathrm{fb}^{-1}$ of good data is used in this analysis, out of the $21.3\,\mathrm{fb}^{-1}$ recorded in 2012. Additional quality requirements are applied to remove events collected during short noise bursts in the detector or events that encountered processing problems in the trigger or offline reconstruction. After these event quality criteria are applied, a total integrated luminosity of $20.2\,\mathrm{fb}^{-1}$ remains for the measurement of the photon cross-section presented in this thesis.

4.2 Trigger Selection

Data used to measure the photon cross-section are required to have satisfied at least one of the single photon trigger criteria. In 2012, the single photon trigger transverse energy thresholds were set at 20, 40, 60, 80, 100 and 120 GeV. The 120 GeV trigger represents the lowest threshold for which no prescaling[1] was necessary, while still respecting the allocated data taking bandwidth for the photon triggers. The prescale factors applied to the other photon triggers were adjusted as a function of time during a proton-proton fill according to the instantaneous luminosity in order to maximize the amount of data recorded within the allocated bandwidth. The photon trigger efficiency is defined as

$$\epsilon_{trig} = \frac{N^{\text{pass}}}{N^{\text{total}}}, \tag{4.1}$$

where N^{total} is the number of events in which the photon with highest transverse energy falls in a particular E_{T}^{γ} bin. The symbol N^{pass} represents the number of these events that satisfy a specific trigger criteria. Trigger efficiencies are measured using event samples that were recorded by a different trigger than the one for which the efficiency is being measured. The resulting efficiencies for each photon trigger relevant to this analysis are shown in Figure 4–1 as a function of reconstructed E_{T}^{γ}.

[1] A prescale value refers to the fraction of events having satisfied a trigger selection that is actually selected for further processing.

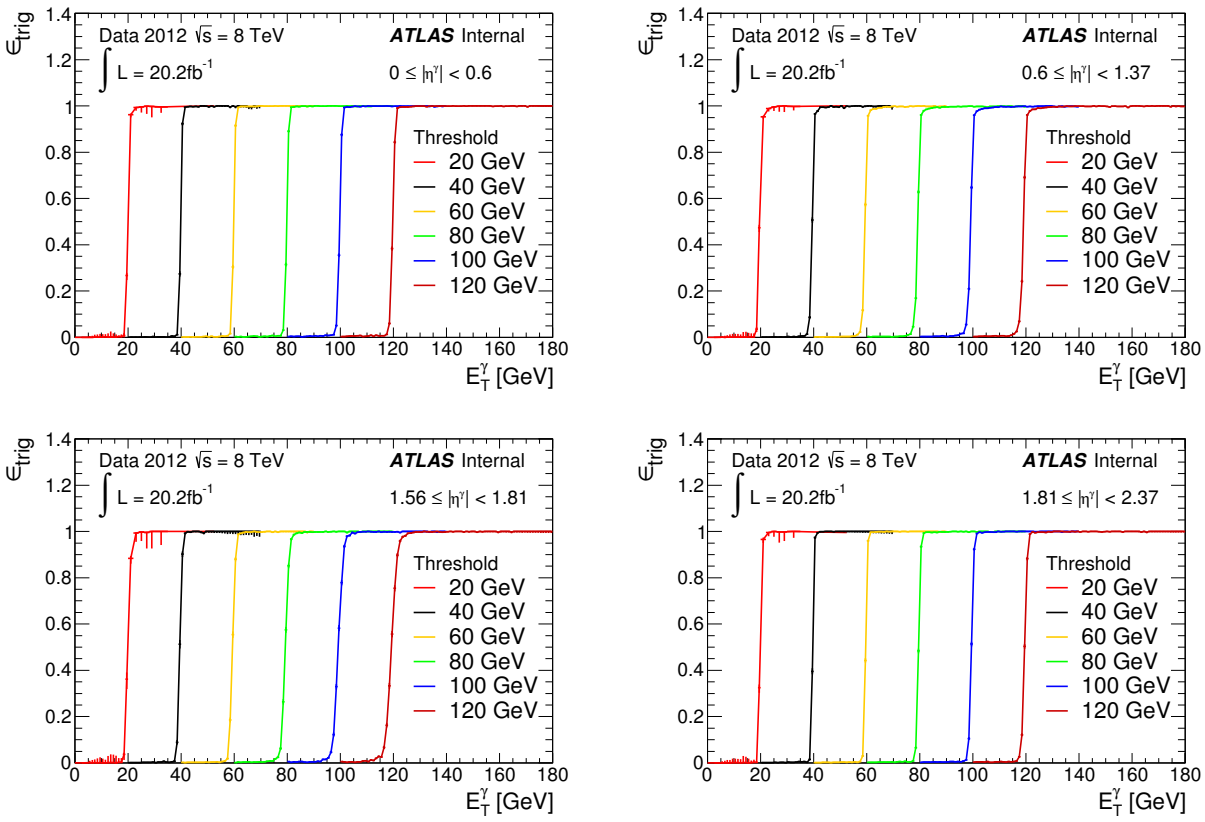

Figure 4–1: Photon trigger efficiencies as a function of E_{T}^{γ} for all triggers relevant to this analysis. The trigger efficiencies are measured in four different pseudorapidity regions.

E_{T}^{γ} Threshold [GeV]	Rec. E_{T}^{γ} Range [GeV]	Efficiency (%)	Average Prescale Factor
20	[25-45)	$100_{-0.1}$	4400
40	[45-65)	$99.8^{+0.1}_{-0.1}$	350
60	[65-85)	$99.8^{+0.1}_{-0.1}$	81
80	[85-105)	$99.7^{+0.1}_{-0.1}$	28
100	[105-125)	$99.7^{+0.1}_{-0.1}$	13
120	[125-1500)	$99.6^{+0.1}_{-0.1}$	1

Table 4–1: List of single photon triggers used in the analysis with the range of E_{T}^{γ} for which each trigger is used. The efficiencies quoted correspond to the trigger efficiency integrated over the E_{T}^{γ} range for which the trigger is used. In addition, the average prescale factors of each trigger are listed as well.

To avoid double-counting of events, each E_{T}^{γ} bin of the photon production cross-section measurement is populated with events that satisfy one specific photon trigger. Each photon trigger is used for values of reconstructed E_{T}^{γ} greater than 5 GeV above the E_{T}^{γ} threshold of the respective photon trigger. This ensures a trigger efficiency of almost 100% and only small corrections need to be applied to account for residual trigger efficiencies. Table 4–1 shows the E_{T}^{γ} region for which each photon trigger is used. The trigger efficiencies listed in the table correspond to the trigger efficiency integrated over the E_{T}^{γ} range for which the trigger is used. The prescale values quoted for each photon trigger are accounted for in the calculation of the final measurement of the photon production cross-section.

4.3 Photon Identification

The photon identification criteria are designed to obtain a high identification efficiency for prompt photons, while rejecting as much background as possible (mainly electrons and non-prompt photons).

4.3.1 Photon Preselection

The photon identification is seeded by identifying a cluster of projective towers[2] in the electromagnetic calorimeter[3] . The size is based on the granularity of the second layer of the calorimeter and corresponds to 3×5^4 cells of this layer in $\eta \times \phi$. Next, reconstructed tracks by the inner detector are extrapolated to the electromagnetic calorimeter for a possible association with an identified electromagnetic cluster. Clusters without matching tracks are classified as "unconverted"[5] photons. "Converted" photon candidates ($\gamma \to e^+e^-$) are identified by the presence of one or

[2] A projective tower is a slice of 0.025×0.025 in $\eta \times \phi$ through the entire electromagnetic calorimeter. This size of the cluster corresponds to the cell size of the second layer of the calorimeter.

[3] At this stage of the analysis bad quality clusters/cells or fake clusters/cells originating from calorimeter problems not already rejected by the general event selection requirements are removed.

[4] In the barrel a projective size of 3×5 cells is used while in the end-cap regions it is increased to 5×5 cells.

[5] Photon conversion refers to the electron-positron pair production that occurs through the interaction of a photon with matter.

two nearby tracks in the inner detector[6] pointing to the identified electromagnetic calorimeter cluster. Approximately $25 - 35\%$ of all identified photons are classified as converted photons.

The photon energy is calculated as the sum of the cell energies within the electromagnetic cluster. In the barrel a projective tower size of 3×5 cells and 3×7 cells in $\eta \times \phi$ is used for unconverted and converted photons respectively. In the end-cap regions the photon energy is calculated using a projective tower size of 5×5 cells in $\eta \times \phi$ for both unconverted and converted photons.

The pseudorapidity of a photon candidate is taken as the cluster barycentre[7] position in the second layer of the EM calorimeter.

4.3.2 Photon Energy Calibration

The photon energy calibration [63] is necessary to extract the true energy of the photon from the measured cluster energy within the electromagnetic calorimeter. This calibration starts at the cell level of the calorimeter of the ATLAS detector. In testbeam studies [64], calibration factors have been established to account for the unmeasured electromagnetic energy deposition in the absorber layers of the calorimeter. These calibrated cell energies are used to calculate the total energy of photon

[6] A dedicated vertex algorithm is used to reconstruct conversion vertices from all reconstructed tracks based on the specific nature of the photon (massless and electromagnetically neutral).

[7] The cluster barycentre is the energy weighted cell position.

candidates identified through the procedure explained in the previous Section 4.3.1. Additional corrections are applied to obtain a precise calibration of the energy measurement of photons. The calibration procedure consists in the following four steps:

- Uniformity corrections: To account for variations in the calorimeter response, not included in the simulation in specific regions of the calorimeter, uniformity corrections are applied to the measured cluster energy. These photon energy correction factors account for effects such as high-voltage inhomogeneity in the electromagnetic calorimeter, differences in the geometrical gap between electromagnetic calorimeter modules in azimuthal direction due to gravity, and biases in the electromagnetic calorimeter electronics calibration.

- Intercalibration of the electromagnetic calorimeter layers: The ratio of energy scales in the first and second layers of the electromagnetic calorimeter in data is corrected to match that in simulation. To achieve this, an η-dependent correction factor is applied to the measured cluster energy in the second layer of the calorimeter. The correction is applied to account for residual differences in the first and second electromagnetic calorimeter layer response that are not accounted for by the initial cell-level calibration described above. No corrections are applied to the measured energy of the third electromagnetic calorimeter layer since its contribution to the overall photon energy is negligible in the photon energy range considered in this analysis.

- Corrections of the overall photon response of the electromagnetic calorimeter: These corrections are based on simulated photon events. Per photon correction

factors are obtained using a multivariate algorithm[8] (MVA) by comparing the measured energies of electromagnetic clusters to the true incident photon energies. The simulated events allow the MVA to extract correlated distributions of photon shower shape variables both at truth and detector level. Based on these distributions, the MVA is used to find the most probable true photon energy given the values of a photon at detector level. The measured photon energy is thus corrected to the most probable true photon energy.

- Energy scale and resolution corrections: Per photon energy scale and resolution corrections [63] are applied to MC simulated events to match the electromagnetic calorimeter response observed in data. These corrections are obtained from a comparison of the reconstructed invariant mass distribution of $Z \to ee$ events in data and MC simulated events. The electromagnetic calorimeter response to electrons is assumed to be identical to that of photons.

4.3.3 Photon Shower Shape Selection

The final step of the photon identification exploits specific differences between prompt and non-prompt photons in order to significantly reduce this dominant background. A prompt photon has no other particles linked to its direction of flight, whereas photons originating from secondary particles have a high probability to be accompanied

[8] Approximately nine variables (extracted from the available detector energy measurements and subsystems defining the position and shower shape) are identified and used to perform this MVA to extract calibration factors, which are separately tuned for converted and unconverted photons.

by additional particles. Therefore, differences in the shower shapes are exploited. For prompt photons, the energy is expected to be fully contained within the electromagnetic calorimeter, typically within a narrow cluster with one energy maximum. For background photons the shower profile is expected to be broader and significant energy in the hadronic calorimeter may be present, due to additional overlapping energy deposited in the calorimeter by accompanying particles. Quality requirements on the shape of the photon energy cluster provides some discrimination between a cluster of energy produced by one photon and that produced by two overlapping photons likely originating from the decay of a light meson. Therefore in total, nine longitudinal and lateral shower shape variables are used to reject background photons originating from hadronic particles. More details can be found in Appendix F and Reference [65].

- w_{s3}: The width of the shower, measured in units of cells, within 3 cells (strips)[9] of the first layer of the calorimeter. w_{s3} quantifies the drop in energy of the two surrounding strips compared to the most energetic strip. For prompt photons, for which the energy is deposited very centrally, the energy drop is expected to be higher and therefore yield smaller values of w_{s3}.

- w_{stot}: The "total" shower width measured in units of cells in a region of 20×2 strips in $\Delta\eta \times \Delta\phi$ of the first layer of the calorimeter and centred around the

[9] As mentioned in Section 3.2.3, the first layer of the electromagnetic calorimeter is designed with a high granularity in η while having a coarser spacing in ϕ, thus leading to strip-like cells.

strip with the maximum energy. The energy of each strip is weighted by the cell distance and normalized to the energy of the most energetic strip. Similarly to w_{s3}, this variable typically yields smaller values for prompt photons compared to background photons since the energy is more centralized.

- w_2: The lateral width of the shower (second layer of the electromagnetic calorimeter) defined as

$$w_2 = \sqrt{\frac{\Sigma E_i \Delta\eta_i^2}{\Sigma E_i} - \left(\frac{\Sigma E_i \Delta\eta_i}{\Sigma E_i}\right)^2}, \tag{4.2}$$

  where the summation, i, runs over all cells in the cluster of 3×5 cells in $\Delta\eta \times \Delta\phi$. The distribution of w_2 is expected to be narrowly peaked as opposed to the distribution of background photons. In essence, this reflects a fairly constant $\Delta\eta$-weighted energy variance for prompt photons.

- F_{side}: The fraction of energy measured in the first layer of the calorimeter outside a core of three central strips, but within seven strips of the strip with the maximum measured energy deposition. For prompt photons this energy fraction outside the core region is below a few tenths of a percent.

- R_η: The energy measured in the second layer of the calorimeter in a cluster of 3×7 cells divided by the cluster energy of 7×7 cells ($\Delta\eta \times \Delta\phi$). The value of this variable is expected to be close to 1 for prompt photons that deposit most of their energy within a cluster size of three cells in the η direction.

- R_ϕ: The energy measured in the second layer of the calorimeter in a cluster 3×3 cells divided by the cluster energy of 3×7 cells ($\Delta\eta \times \Delta\phi$). The value of this variable is expected to be close to 1 for prompt photons that deposit most of their energy within a cluster size of three cells in the ϕ direction.

- R_{had}: The ratio of transverse energy measured in the first layer of the hadronic calorimeter and the measured transverse energy of the electromagnetic cluster[10] . This variable is expected to be close to 0 for prompt photons as they are expected to be fully absorbed in the electromagnetic calorimeter and are not accompanied by hadronic activity.

- ΔE: This quantity is measured in the first layer of the electromagnetic calorimeter. ΔE is the energy difference of the strip with the 2^{nd} maximum energy and the energy of the strip with the minimum energy located between the strip with the highest and second highest energy measurements. This variable is zero if the strip with the second largest energy is adjacent to the strip with the maximum energy. ΔE quantifies the presence or not of a second peak within the cluster. The value of this variable is expected to be zero for prompt photons. This variable provides rejection against π^0 decaying to two photons.

[10] For the pseudorapidity range $0.8 < |\eta| < 1.37$ that is not covered by the first hadronic layer), the total hadronic transverse energy is used.

- E_{ratio}: Measured in the first layer of the electromagnetic calorimeter. E_{ratio} is the ratio of the energy difference between the strip with the largest and second-largest energy deposition over their sum. For prompt isolated photons, most of the cluster energy is expected to be deposited within one strip and therefore a value close to 1 is expected.

The particular cut values of each of the nine variables are tuned for converted and unconverted photons separately, as well as adjusted depending on the transverse energy of the photon and its pseudorapidity (matching the four η-regions of the differential cross-section measurement of this analysis).

4.3.4 Photon Transverse Isolation Energy

At this point of the photon selection, some fraction of photon candidates are still not real prompt photons but background photons originating from secondary decays or radiation processes. A known source for such background photons are neutral light mesons (π^0, η, etc.) decaying into photon pairs. Considering that those light mesons are generally created as part of the hadronization process, they are typically accompanied by additional particles surrounding the decay photons. A common technique to exploit this feature is to restrict the allowed additional transverse energy measured around the photon candidate. The transverse isolation energy ($E_{\text{T}}^{\text{iso}}$) is defined as the amount of additional energy measured around the photon candidate calorimeter cluster, within a fixed geometrical cone of size $\Delta R = 0.4$. At the truth (MC) level $E_{\text{T}}^{\text{iso}}$ is calculated as the energy sum of all particles inside the geometrical cone of $\Delta R < 0.4$ (excluding the photon itself). At the reconstruction (i.e. detector)

level, the distinction between the additional calorimeter activity and the measured energy deposited by the photon candidate is more complicated. Inside a geometrical region of $\Delta R < 0.4$ a rectangular region of projective tower size of 5×7 cells in the $\eta - \phi$ plane centred around the position of the photon candidate position is removed from the calculation of $E_{\mathrm{T}}^{\mathrm{iso}}$. The size of this rectangular region is chosen to encompass most of the photon energy cluster[11] . A graphical representation of the geometrical area included in the calculation of $E_{\mathrm{T}}^{\mathrm{iso}}$ is shown Figure 4–2. The calorimeter cells falling within the grey area are grouped into topological clusters[12] , including cells from both the electromagnetic and hadronic calorimeter to determine $E_{\mathrm{T}}^{\mathrm{iso}}$. This energy is then corrected for any energy from the photon itself that was not captured by the exclusion of the core region. This correction is evaluated as a function of E_{T}^{γ} and η, using simulated photon samples. Furthermore, to account for effects such as underlying-event modelling and pile-up, a correction based on the so-called "jet-area" method is applied [66, 67]. This technique uses low-energy jets

[11] The electromagnetic shower is commonly characterized by the Molière radius, referring to its radial width in the $\eta - \phi$ plane containing 90% of the shower energy. The Molière radius in the electromagnetic calorimeter is approximately 4.3 cm corresponding to 1.3 cells in the barrel. The exclusion of the central 5×7 projective towers ensures that almost the entire shower (over 95%) is contained inside this core region.

[12] Instead of combining detector cells together into fixed cluster towers, they are combined depending on their relative energies, allowing for almost a three dimensional representation of the shower. For example, in a three dimensional topological cluster, the number of cells associated with the cluster can vary as function of calorimeter layer.

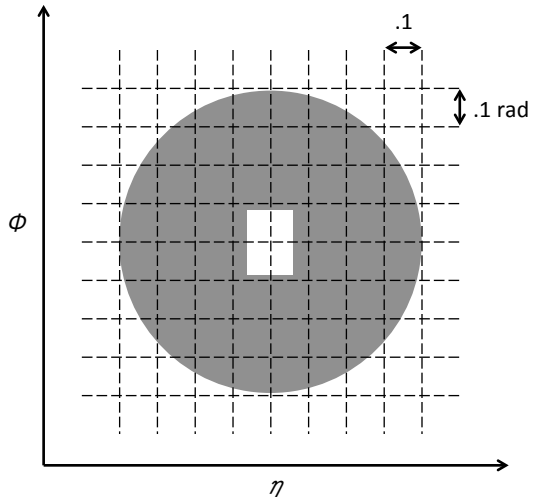

Figure 4–2: Graphical representation of the geometrical area of the calorimeter considered (in grey) when calculating the transverse isolation energy in reconstructed events. The area is defined by a circle of diameter $\Delta R = 0.4$ around the position of the photon candidate. A rectangular region of 5×7 (approximately 0.125×0.175 rad in $\eta - \phi$) projected towers centred along the photon candidate direction is excluded from the calculation.

to compute an ambient energy density event-by-event, which is multiplied by the area of the isolation cone and subtracted from the isolation energy. The correction applied to the isolation energy is typically of the order of 1.5 - 2.0 GeV per photon candidate in the 2012 data sample.

This analysis utilizes an E_{T}^{γ}-dependent isolation requirement, in order to keep the signal to background ratio as high as possible throughout the large photon transverse energy range considered. The E_{T}^{γ}-dependent isolation requirement also ensures a constant and high photon identification efficiency as a function of E_{T}^{γ}. The selected E_{T}^{γ}-dependent cut is used both at truth and detector level and is defined as:

$$E_{\mathrm{T}}^{iso} < 4.8 \text{ GeV} + (4.2 \times 10^{-3}) \times E_{\mathrm{T}}^{\gamma} [\text{ GeV}]. \tag{4.3}$$

Figure 4–3 shows a representative example of the isolation energy distribution measured in data in the range $250 \leq E_{\mathrm{T}}^{\gamma} < 300$ for the different pseudorapidity regions. The normalized background and signal distribution from MC simulation are overlaid to show their contributions. The E_{T}^{γ}-dependent isolation cut value is visualized through the vertical black line.

Figure 4–4 presents the performance of the E_{T}^{γ}-dependent isolation cut on signal photons (from MC) by showing the efficiency versus E_{T}^{γ} for a given photon to pass the cut. This transverse isolation energy cut efficiency is defined as

$$\epsilon_{\mathrm{iso}} = \frac{N^{\mathrm{reco,iso,matched}}}{N^{\mathrm{reco,matched}}}, \tag{4.4}$$

where $N^{\mathrm{reco,matched}}$ is the number of reconstructed photon candidates that are also identified to fall within a geometrical cone radius of $\Delta R < 0.2$[13] of a true simulated photon. The symbol $N^{\mathrm{reco,iso,matched}}$ is the number of such reconstructed photons that also satisfy the transverse isolation energy cut.

[13] The specific value was chosen from checking the ΔR distribution (see appendix B) between the two photon objects. The distribution peaks at zero and a negligible number of photons fall beyond a value of 0.2.

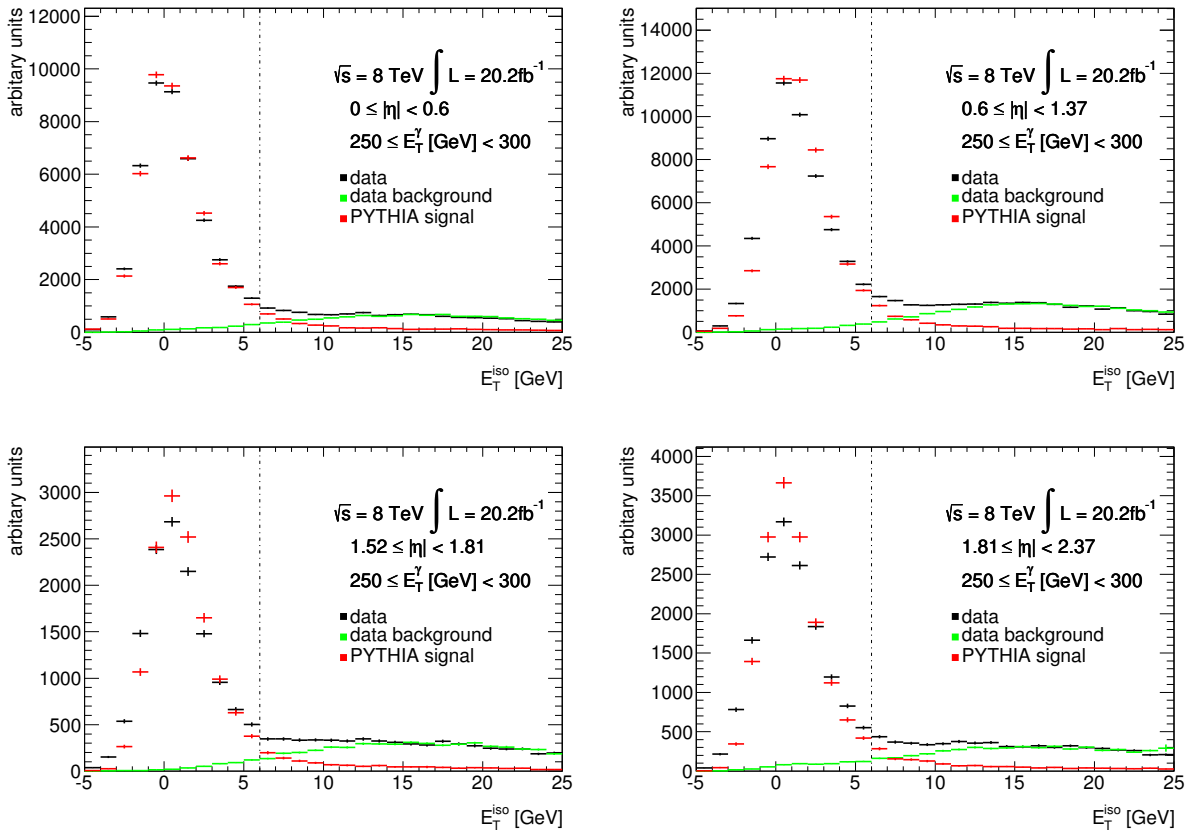

Figure 4–3: Transverse isolation energy distribution for photons with $250 \leq E_{\mathrm{T}}^{\gamma} < 300$ in the four pseudorapidity regions considered in the analysis. Three different $E_{\mathrm{T}}^{\mathrm{iso}}$ distributions are shown: identified photons as selected in this analysis (red), identified photons within the simulated events using `PYTHIA` (black), as well as background photons measured in data (blue). The vertical dashed line represent the chosen $E_{\mathrm{T}}^{\mathrm{iso}}$ cut value for the E_{T}^{γ} range shown.

In general a constant value of efficiency as a function of E_{T}^{γ} is favourable since this significantly reduces the E_{T}^{γ} dependence of the modelling of the isolation energy in the MC simulation. Figure 4–4 shows the $E_{\mathrm{T}}^{\mathrm{iso}}$ cut efficiency as function of E_{T}^{γ} for both the E_{T}^{γ}-dependent transverse isolation energy cut and a cut at a fixed value of $E_{\mathrm{T}}^{\mathrm{iso}}$. The drop at $E_{\mathrm{T}}^{\gamma} \gtrsim 500$ GeV in Figure 4–4 for the choice of fixed $E_{\mathrm{T}}^{\mathrm{iso}}$ cut values shows that the reconstruct energy cluster of prompt photons at these energies has an increased probability to be accompanied by additional energy deposited nearby, resulting in values of photon transverse isolation energy of a few GeV which are sometimes larger than the fixed isolation energy cut values.

4.3.5 Corrections Applied to Simulated Event Samples

In order to consistently define a kinematic region for the cross-section measurement that is closely related to the analysis selection cuts, the same isolation energy requirement and pseudorapidity boundaries are applied to the properties of true photons in simulated events.

Furthermore, to match the overall event conditions of the data sample studied, and to account for known residual discrepancies between data and simulation, the following corrections are applied:

- In order to reproduce the pile-up conditions that existed in the LHC during the data taking in 2012, the MC simulated events are individually weighted. Event weights are derived from the distribution of the average number of interactions per bunch crossing (μ) and are defined as

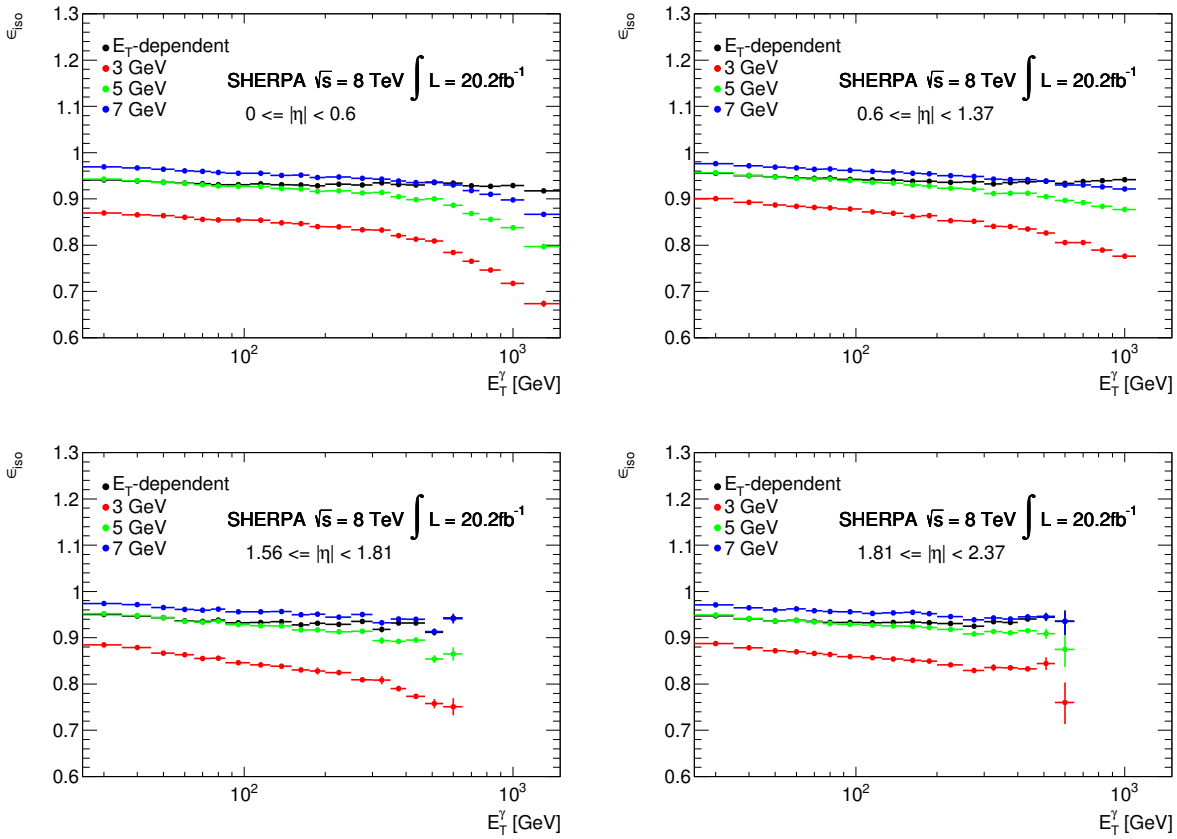

Figure 4–4: Probability of a signal photon passing the transverse isolation energy cut in the four pseudorapidity regions considered and as a function of E_{T}^{γ}. In addition to the E_{T}^{γ}-dependent isolation energy cut (black) used in this measurement, the efficiency obtained using three fixed cut values is shown. The fixed cut values of 5 GeV (green) and 7 GeV (blue) are chosen to match the range of cuts obtained using the E_{T}^{γ}-dependent isolation energy cut. The efficiency obtained using a fixed cut of $E_{\mathrm{T}}^{\mathrm{iso}} < 3$ GeV is also shown in red. This cut value was used in a previous ATLAS photon cross-section measurement [9, 10].

$$\mathrm{w}_i = \frac{N_i^{\mathrm{data}}}{N_i^{\mathrm{MC}} \cdot 1.09}, \tag{4.5}$$

where N_i^{data} and N_i^{MC} represent the number of data and MC simulated events, respectively, in each bin i of the distribution of μ. The factor 1.09 is introduced to improve the agreement between the data and MC distributions of the number of primary vertices[14] .

- The distributions of shower shape variables used for the identification of photon candidates are shifted in the MC simulation in order to match the measured distribution in data. This allows the same photon reconstruction quality cuts to be applied to both data and MC simulated events.

- The transverse isolation energy of photon candidates in MC simulated events is shifted such that the peak of the distribution obtained using MC simulated events matches that measured in data. A value for this correction is obtained in each bin of photon transverse energy and pseudorapidity considered in the analysis. Correction values vary from a few hundred MeV up to 4 GeV and are consistent for both LO generators (`PYTHIA` and `SHERPA`). The exact shift values for each photon E_{T}^{γ} and η bin are listed in Appendix D.

[14] It is important that the MC simulation describes well the distribution of the number of primary vertices reconstructed since one of the correction factors applied to the calculation of the transverse isolation energy of a photon depends on the number of reconstructed vertices.

- Event weights are applied to MC simulated events to improve the agreement between the distributions of the z-vertex position of the hard interaction in MC and data. This ensures that the η distribution of MC simulated photon candidates matches that measured in data.

- Event weights are applied to MC simulated events in order to remove small residual differences between the photon identification efficiency measured by the photon performance group in data and MC simulated events [71]. The photon identification efficiency is extracted through a combination of three data-driven methods. The first method is used for $E_{\mathrm{T}}^{\gamma} < 80$ GeV and is based on a photon sample selected from radiative decays of the Z boson. The second method provides a photon identification measurement in the region $30 \leq E_{\mathrm{T}}^{\gamma} < 100$ GeV. This method is based on a pure sample of electrons from Z boson decays and relies on the assumption that energy clusters originating from electrons have the same shower shape than that of photons. The third method relies on the number of tracks reconstructed in a cone centred around the barycentre of the electromagnetic cluster. The number of tracks is used as a discriminating variable between background and prompt photons to extract the sample purity before and after the shower shape cuts introduced in Section 4.3.3 are imposed. This method allows to cover a large E_{T}^{γ} range and provides a photon identification measurement up to $E_{\mathrm{T}}^{\gamma} = 1500$ GeV.

4.3.6 Photon Identification Efficiency

Photon candidates considered for the measurement of the inclusive prompt photon production cross-section are required to satisfy all the criteria described in Sections 4.3.1 to 4.3.5. The impact of this selection is quantified by measuring the overall photon identification efficiency using MC simulated events. The photon identification efficiency is defined as

$$\epsilon_{\text{id}} = \frac{N^{\text{id,matched}}}{N^{\text{true}}}, \tag{4.6}$$

where N^{true} is the number of true prompt photon in the simulation satisfying the transverse isolation energy cut applied at the truth level, and $N^{\text{id,matched}}$ is the number of these true photons that have a reconstructed photon candidate satisfying all the photon identification selection within a cone of radius $\Delta R < 0.2$.

The overall photon identification efficiency as function of E_{T}^{γ} and η is shown in Figure 4–5. A maximum efficiency of approximately 92 % is obtained for medium energy photons at an transverse photon energy of order 100 GeV. For all pseudorapidity regions, the efficiency decreases for lower E_{T}^{γ} since in this region a relatively higher fraction of background photons exist and a balance between efficiency and rejection is preferable. Figure 4–5 also shows the identification efficiency separately for converted and unconverted photon candidates. The identification efficiency for converted photon candidates decreases by typically more than 10% at high values of E_{T}^{γ} in all η regions. Converted photon candidates ($\gamma \to e^{+}e^{-}$) are identified by

the presence of two nearby tracks in the inner detector pointing to the identified electromagnetic calorimeter cluster. The two e^+e^- tracks are more collimated for higher values of photon energy. The decrease in identification efficiency at high E_{T}^{γ} for converted photons is therefore due to a decrease in the efficiency at reconstructing two nearby tracks. The efficiency in the pseudorapidity regions $1.56 \leq |\eta| < 1.81$ and $1.81 \leq |\eta| < 2.37$ is also lower than that measured in the region $|\eta| < 1.37$. This difference in efficiency is again due to an overall lower converted photon identification efficiency. The efficiency to reconstruct two nearby tracks is reduced in the region $1.56 \leq |\eta| < 1.81$ because it corresponds to the overlap between different inner detector modules, and tracking in the region $1.81 \leq |\eta| < 2.37$ is limited to the information obtained from the forward disks of the SCT detector, the pixel end-caps, and has no TRT ($|\eta| \geq 2$).

A separate study following the observation of the significant E_{T}^{γ} dependence of the converted photon identification efficiency was performed. Preliminary results have shown that it is possible to significantly improve the converted photon identification efficiency by adjusting the identification requirements for converted photons at high E_{T}^{γ}. These adjustments will be further tested and deployed during future data recording.

4.4 Event Selection

The cross-section measurement presented here only considers events that have at least one photon satisfying the criteria described in Section 4.3 with a minimum transverse energy of 25 GeV and within $\eta < 2.37$ (excluding the region $1.37 \leq \eta < 1.56$).

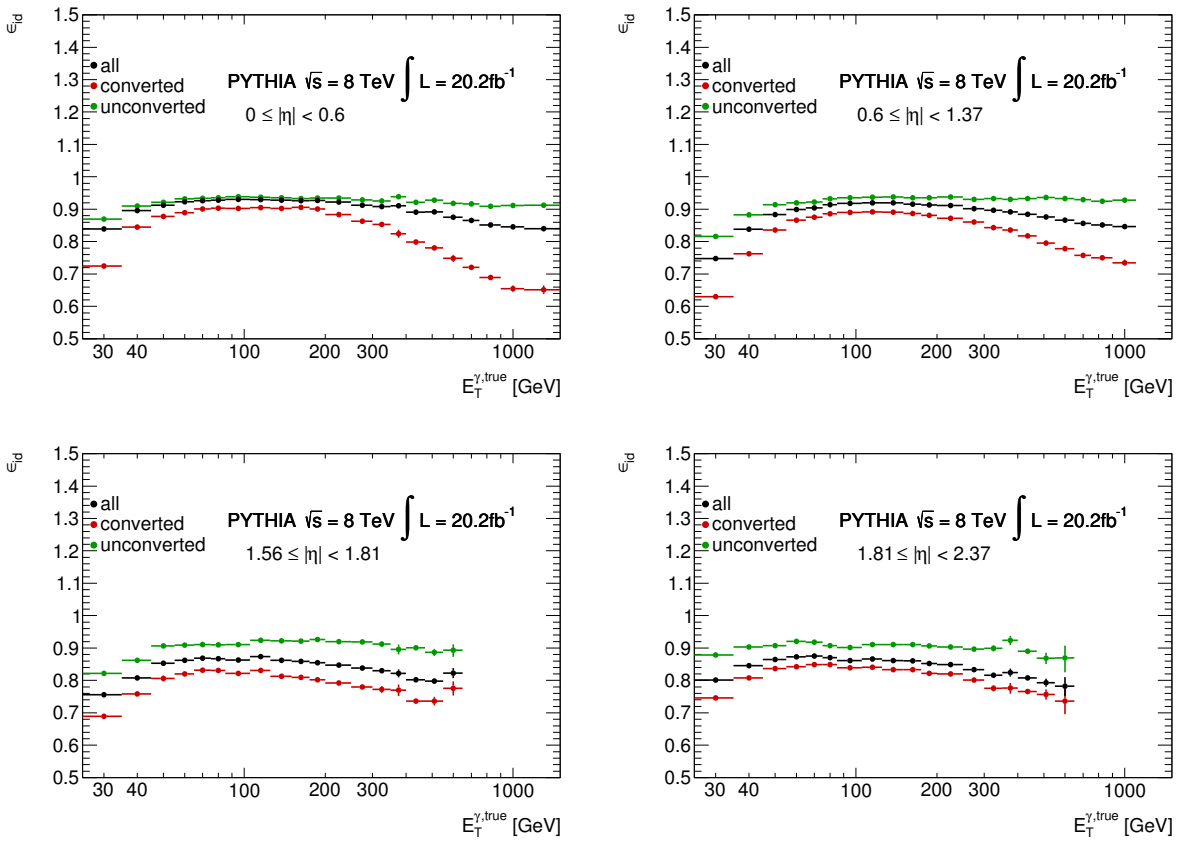

Figure 4–5: Photon identification efficiency as function of transverse energy in each of the four pseudorapidity regions considered in the analysis. The total identification efficiency (black), as well as the identification efficiency for converted (red) and unconverted (green) photons is shown.

For events containing multiple photons passing these criteria, only the photon with the highest transverse energy is considered. The measurement is performed as a function of E_{T}^{γ} and split into four regions of pseudorapidity related to the geometry of the calorimeter. The inner barrel with the least amount of extra material such as supporting structure cooling systems and readout electronics corresponds to the first region of $|\eta| < 0.6$. The second region covers the remainder of the barrel part of the detector up to a pseudorapidity of 1.37. The region $1.37 \leq |\eta| < 1.56$ is excluded from this measurement since it is the transition region between the barrel and end-cap modules of the electromagnetic calorimeter with poor energy scale and resolution measurement, the reason being that a sizeable amount of supporting structures and cooling systems of the ATLAS detector is placed in this pseudorapidity region. The higher values of photon pseudorapidity are measured in two regions of $1.56 \leq |\eta <$ 1.81 and $1.81 \leq |\eta < 2.37$. This separation is based on the overall angular coverage of the inner detector up to a pseudorapidity of 2.4 and the presampler[15] of the calorimeter that reaches a maximum of $\eta < 1.82$.

[15] The presampler is an additional layer of liquid argon in front of the electromagnetic calorimeter used to measure the energy lost by the particles as they pass through the material preceding the calorimeter system.

CHAPTER 5
Background Subtraction

Following the event selection and quality criteria introduced in the previous chapter, the next step towards the cross-section measurement is to remove any remaining background that would contribute to the total number of photon events measured in the data set. There are two background sources that have to be considered. The first type of background events are events where the most energetic photon originates from the decay of a light meson or is radiated off a charged particle. The second type of background consists in events where an electron is mis-reconstructed as a photon. Secondly, considering that the signature of electrons measured in the detector is very similar to photons, it is necessary to quantify if and how often an electron can pass the whole photon selection. This chapter explains how these two sources of background are estimated and subsequently subtracted from the number of photon candidates observed in data.

5.1 Background Estimation and Subtraction

As presented in Chapter 4, the differences in shower shape and transverse isolation energy between non-prompt and prompt photons are exploited to increase the purity of the sample of photon candidates selected. Thus, photon candidates failing to satisfy the identification requirements on the shower shape or transverse isolation energy provide samples of events highly enriched in non-prompt and fake photons.

Therefore, it is possible to define four exclusive regions of phase space (see Figure 5–1), consisting of one signal region and three control regions.

- Region A: The signal region consists in all the events containing a leading photon candidate that satisfies all selection criteria defined in Chapter 4.
- Region B: Events with a leading photon candidate that satisfies all selection criteria including the shower shape cuts, but fails the transverse isolation energy requirement. Photon candidates for events falling into this region are required to have a transverse isolation energy 3 GeV greater than the default cut value. The E_{T}^{γ}-dependent isolation boundary to Region B can therefore be expressed as $E_{\mathrm{T}}^{iso,\gamma} \geq 7.8$ GeV $+ (4.2 \times 10^{-3}) \times E_{\mathrm{T}}^{\gamma}$ [GeV].
- Region C: Events with a leading photon candidate that satisfies the transverse isolation energy requirement but fails at least one of the cuts applied on three of the shower shape variables (w_{s3}, ΔE and F_{side}). The choice of these three variables has been found to maximize the number of non-prompt photons selected while minimizing the number of prompt photons selected (signal).
- Region D: The region defined as the exclusive combination of regions C and B. The region consists of events with a leading photon candidate that has a transverse isolation energy value 3 GeV greater than the default cut value, and that fails at least one of the cuts applied on three of the shower shape variables (w_{s3}, ΔE and F_{side}).

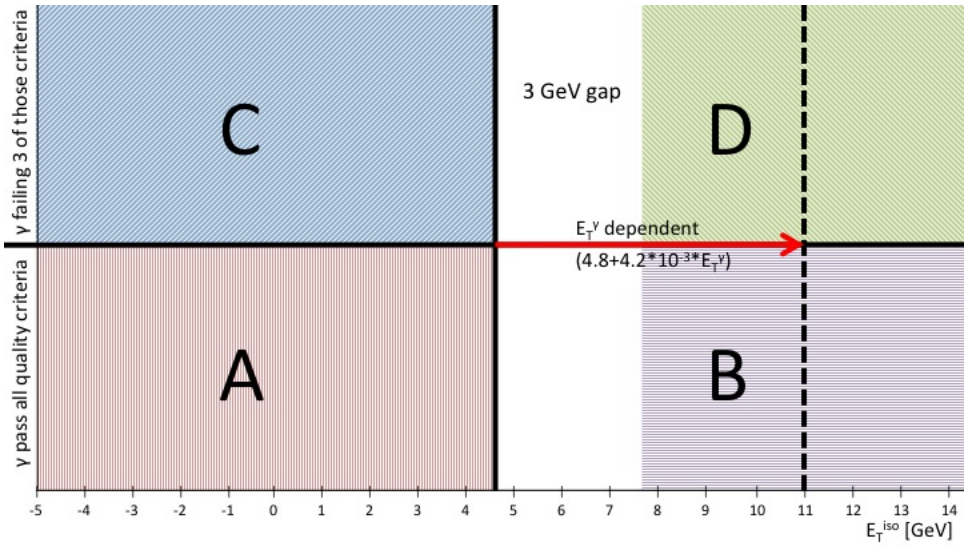

Figure 5–1: Illustration of the two-dimensional plane of the photon shower shape criteria vs. transverse isolation energy used to estimate the background yield in the signal region, A, from the observed yields in the three control regions, B, C and D. The dashed line represents the highest cut value of the E_{T}^{γ}-dependent isolation boundary at $E_{\mathrm{T}}^{\gamma} = 1500$ GeV

The definition of such background enriched samples to estimate the background fraction in a signal region is a common technique in particle physics called a "2D-sideband" subtraction method. It allows this analysis to estimate the remaining background in the signal region almost entirely from data. MC simulations are only needed to correct for some small possible signal leakage into the background-dominated regions. In the simplified scenario, for which B, C and D solely contain background events (i.e. events with a leading photon candidate which is either a non-prompt or fake photon), the number of events with a leading photon candidate which is also a true prompt photon (signal) can be estimated using

$$N_A^{\text{sig}} = N_A - \frac{N_B \cdot N_C}{N_D}, \tag{5.1}$$

where N stands for the number of events in each region denoted by its respective subscript. The signal purity can then be calculated as

$$p_{\text{sig}} = \frac{N_A^{\text{sig}}}{N_A} = 1 - \frac{N_B \cdot N_C}{N_D \cdot N_A}. \tag{5.2}$$

Possible correlations between values of the transverse isolation energy and the electromagnetic cluster shower shape of background photons can be absorbed in a correction factor (R_{bkg}) defined as

$$\frac{N_A^{\rm bkg}}{N_B^{\rm bkg}} = R^{\rm bkg} \times \frac{N_C^{\rm bkg}}{N_D^{\rm bkg}}, \tag{5.3}$$

where the superscript *bkg* refers to the number of events with a leading photon candidate that is not a true prompt photon, in each of the regions of phase space defined above. In this cross-section measurement the correction factor $R^{\rm bkg}$ is set to 1, based on studies that found it to be consistent with unity. The measured fluctuations away from 1 however are used to assess the uncertainty on the assumption $R^{\rm bkg} = 1$ (Appendix E).

The last step of the background subtraction method accounts for signal (prompt) photon events being classified in any of the background regions. The so-called *signal leakage* fractions (c_K) are obtained using MC simulated events and are defined as

$$c_K = \frac{N_K^{\rm sig}}{N_A^{\rm sig}} \tag{5.4}$$

with $K = B, C, D$.

Figure 5–2 shows the signal leakage fractions as a function of $E_{\rm T}^{\gamma}$ in all four η regions. The leakage fraction c_B increases with $E_{\rm T}^{\gamma}$, since the efficiency for the transverse isolation energy selection slightly decreases with increasing $E_{\rm T}^{\gamma}$. The leakage fraction c_C is largest for reconstructed photon transverse energy below 100 GeV since the photon identification efficiency decreases at lower values of $E_{\rm T}^{\gamma}$. The leakage fraction c_D is below 1 % for all values of $E_{\rm T}^{\gamma}$ relevant to the measurement.

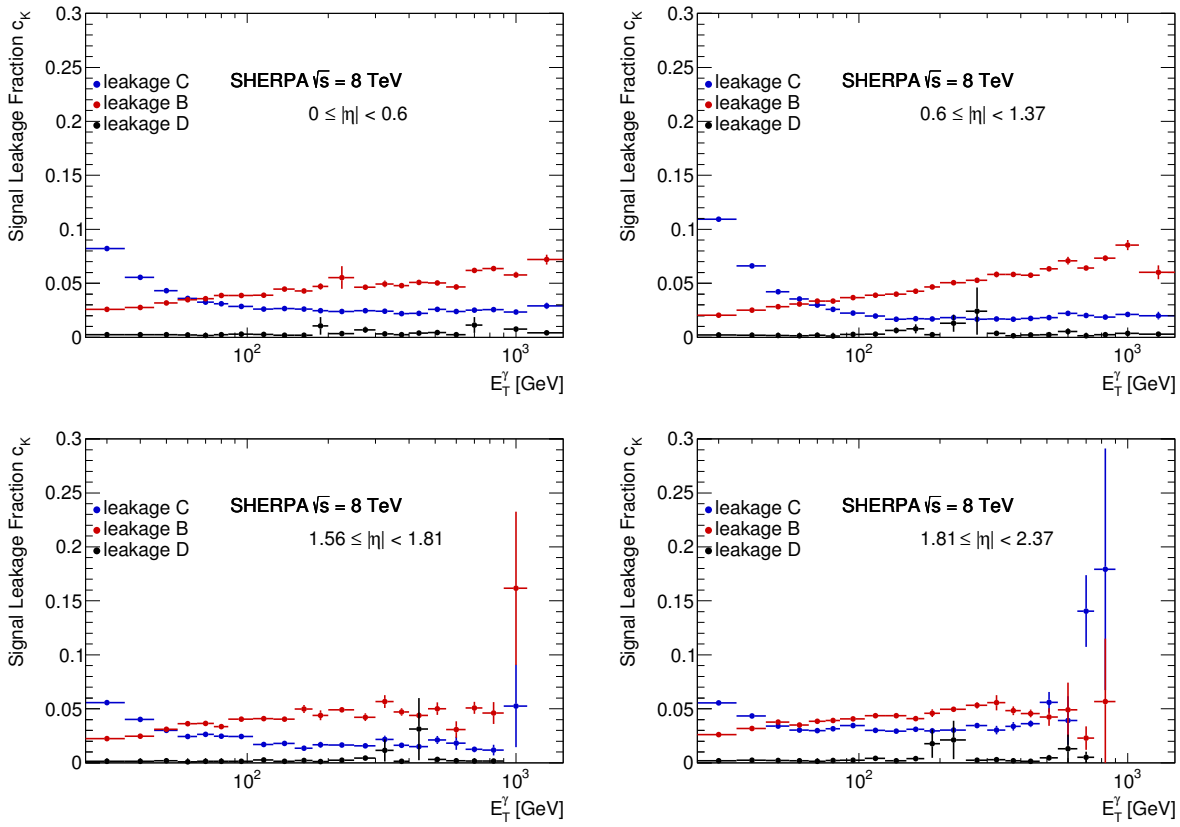

Figure 5–2: Signal leakage fraction (c_K with $K = B, C, D$) in the background dominated regions of the "2D-sideband" method as a function of E_{T}^{γ} and for the different η regions considered.

Taking into account these correction factors, the number of events with a "true" prompt photon can be calculated as

$$N_A^{\text{sig}} = N_A - R^{\text{bkg}} \cdot \left((N_B - c_B N_A^{\text{sig}}) \cdot \frac{(N_C - c_C N_A^{\text{sig}})}{(N_D - c_D N_A^{\text{sig}})} \right). \tag{5.5}$$

This equation is quadratic in terms of the quantity of interest N_A^{sig}. Only the positive solution to the equation is physically meaningful. Figure 5–3 shows the extracted signal purities as a function of E_{T}^{γ} in the different η regions considered. The signal purities without and with signal leakage corrections calculated using `PYTHIA` or `SHERPA` are also shown. As a function of E_{T}^{γ}, the purity rapidly increases from approximately 50% at 25 GeV to approximately 100% at 200 GeV for all η regions. This indicates that beyond 200 GeV, the quality criteria introduced in the photon reconstruction (Section 4.3) effectively reject non-prompt and fake photons at high E_{T}^{γ}. For the lower E_{T}^{γ} region, the contamination is sizeable with almost half the selected photons being considered background. Therefore, the signal leakage corrections dependence on the MC simulation sample used mostly impacts the lower E_{T}^{γ} region.

5.1.1 Background from (Isolated) Electrons Misidentified as Photons

Besides the background arising from non-prompt photons and fake photons that have a higher transverse isolation energy value than signal photons, another source of background contamination comes from electrons faking a prompt photon. As previously mentioned, the calorimeter detector response is very similar for photons and electrons. Although an electron is distinguished from a photon based on a reconstructed

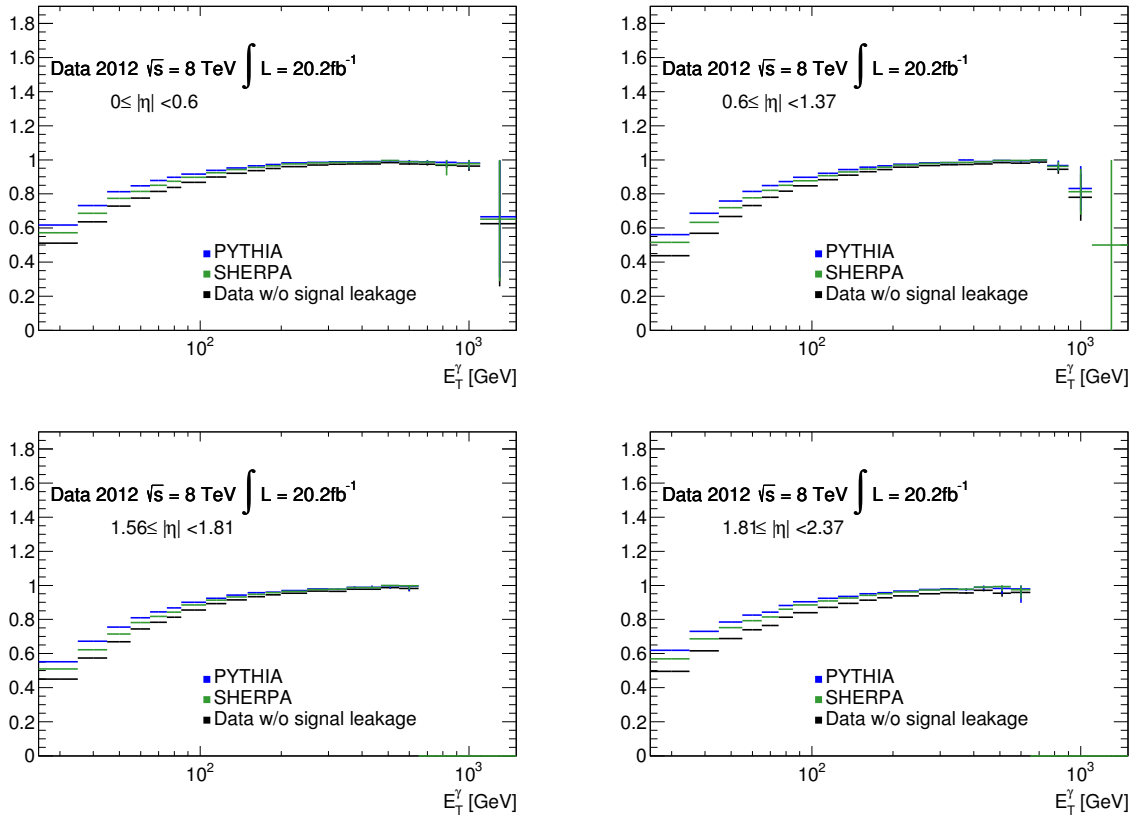

Figure 5–3: Signal purities in data using signal leakage fractions from PYTHIA and SHERPA as a function of E_{T}^{γ} and for the different η region considered. For comparison, the signal purity is also shown before accounting for signal leakage effects.

track in the inner detector, tracking inefficiencies can lead to an electron being reconstructed and identified as a photon candidate. The fake rate of electrons being mis-identified as photon candidates is estimated using $Z \to e^{\pm}e^{\mp}$ and $W \to e^{\pm}\nu$ MC simulated events. It is assumed that the decays of W and Z bosons into electrons are the dominante sources of electron production at the LHC. First, the expected number of events from each physics reaction is obtained by weighting the MC simulated events according to the respective cross-section of each process and the luminosity of the data used for this measurement. Then, the number of fake photons coming from these physics processes is calculated by summing all events that have at least one photon candidate reconstructed within a radius of $\Delta R < 0.2$ of a simulated true electron. This total expected number of fake photons from mis-identified electrons is then divided by the number of signal events obtained after the 2D-sideband background subtraction. The resulting photon fake rate as function of E_{T}^{γ} is shown in Figure 5–4. The largest fraction of mis-identified electrons is 0.7% and corresponds to the region 35 GeV $\leq E_{\mathrm{T}}^{\gamma} <$ 45 GeV. The production cross-section for the two reactions considered is highest in this transverse energy range which corresponds to electrons having an energy approximately half the mass of the decaying boson. The measured number of signal photon events is corrected in each bin by the extracted E_{T}^{γ}-dependent electron fake rate, however no uncertainty is assigned since the effect itself is very small and therefore its uncertainty can be assumed to be negligible in the scope of this analysis.

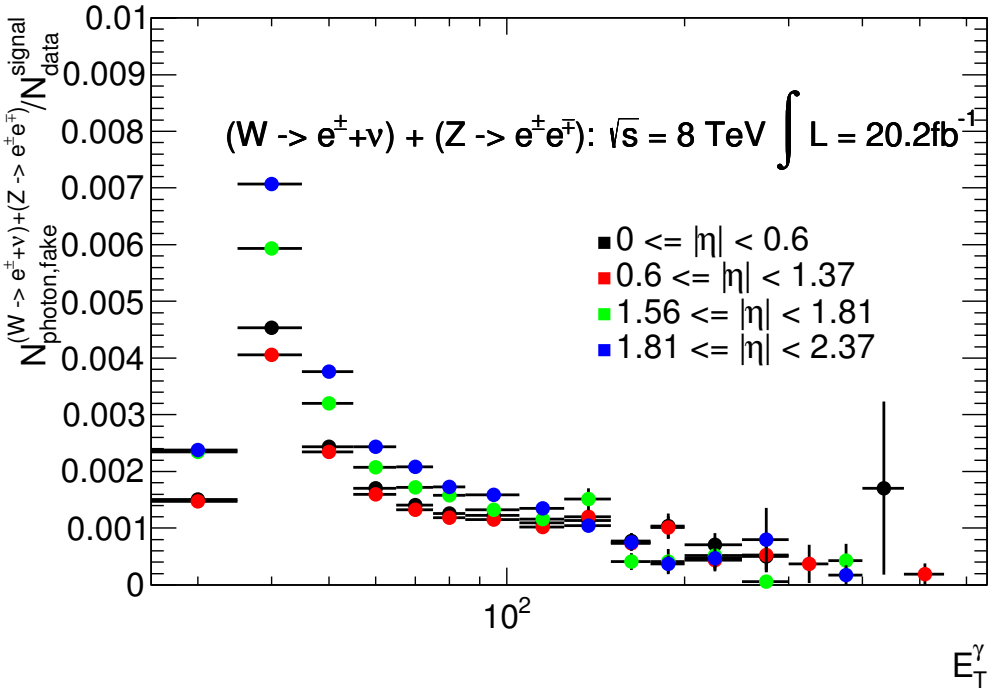

Figure 5–4: Electron fake rate as a function of E_{T}^{γ} extracted from $Z \to ee$ and $W \to e^{\pm}\nu$ MC samples. This fake rate is obtained by dividing the number of expected mis-identified electrons by the number of signal events obtained after the 2D-sideband background subtraction.

CHAPTER 6
Unfolding Detector Effects

The goal of this thesis is to measure the inclusive production cross-section of prompt photons, at the particle-level, independent of the detector performance. By unfolding detector effects from the measured cross-section, the measurement may then be compared to other experimental results as well as theoretical predictions.

The number of selected events in the data is corrected for detector effects such as the finite resolution in the measurement of the energy and direction of particles, and inefficiencies in the prompt photon identification. Detector unfolding correction factors are obtained using the simulated prompt photon samples generated with `PYTHIA`. `SHERPA` is used as a cross-check and to assess the systematic uncertainty associated to parton shower and hadronization models. Both LO parton shower generators produce simulated events that can be passed on to the ATLAS detector simulation thereby producing simulated events mimicking actual data. Various kinematical properties of these simulated event samples were confirmed to describe well real data.

Detector unfolding correction factors are obtained for each E_{T}^{γ} and η bin considered in the analysis. These corrections factors (C_i) are defined as

$$C_i = \frac{N_i^{\mathrm{id}}}{N_i^{\mathrm{true}}}, \tag{6.1}$$

where i represents a particular unique (E_{T}^{γ},η) bin. The symbol N^{true} is the number of simulated events with a true prompt photon satisfying the transverse isolation energy requirement applied at the truth level. The symbol N^{id} corresponds to the number of events with a leading photon candidate satisfying all the photon identification requirements, including the requirement on the maximum transverse isolation energy. In the definition of the correction factors, note that truth-level generated photons are not explicitly required to be geometrically matched with reconstructed photon candidates.

These so-called bin-by-bin correction factors are adequate here to account for detector effects since the size of the E_{T}^{γ} and η bins considered in the analysis were chosen such that most events fall within the same (E_{T}^{γ},η) bin at both truth and detector level.

Figure 6–1 shows the calculated unfolding factors as a function of the transverse photon energy and in different η regions. The detector unfolding correction factors vary between approximately 0.8 and 0.9. The E_{T}^{γ} dependence of these correction factors suggests that one of the main contributions to these corrections comes from inefficiencies in the photon candidate selection.

The statistical uncertainty on the unfolding correction factors arises from the finite number of MC simulated events in each sample used. To avoid double-counting events in the estimate of the statistical uncertainty, three exclusive categories of

events are defined: Events with a leading prompt photon satisfying all requirements both at the truth level and at the detector level and that fall within the same (E_{T}^{γ}, η) bin ($N_i^{\mathrm{id,true,match}}$); Events with a leading photon candidate at the detector level but without a matched prompt photon at the truth level ($N_i^{\mathrm{id,unmatch}}$); Events with a leading prompt photon at the truth level but without a photon candidate at the detector level ($N_i^{\mathrm{true,unmatch}}$). Using this event categorization, the unfolding factors can be expressed as

$$C_i = \frac{N_i^{\mathrm{id,true,match}} + N_i^{\mathrm{id,unmatch}}}{N_i^{\mathrm{id,true,match}} + N_i^{\mathrm{true,unmatch}}}, \tag{6.2}$$

The number of events in each of the three event categories is assumed to be Poisson distributed and the total statistical uncertainty on the unfolding factors is obtained through standard error propagation.

The results of the unfolding are cross-checked with an independent unfolding procedure outlined in Appendix A. Both unfolding approaches provide statistically compatible results.

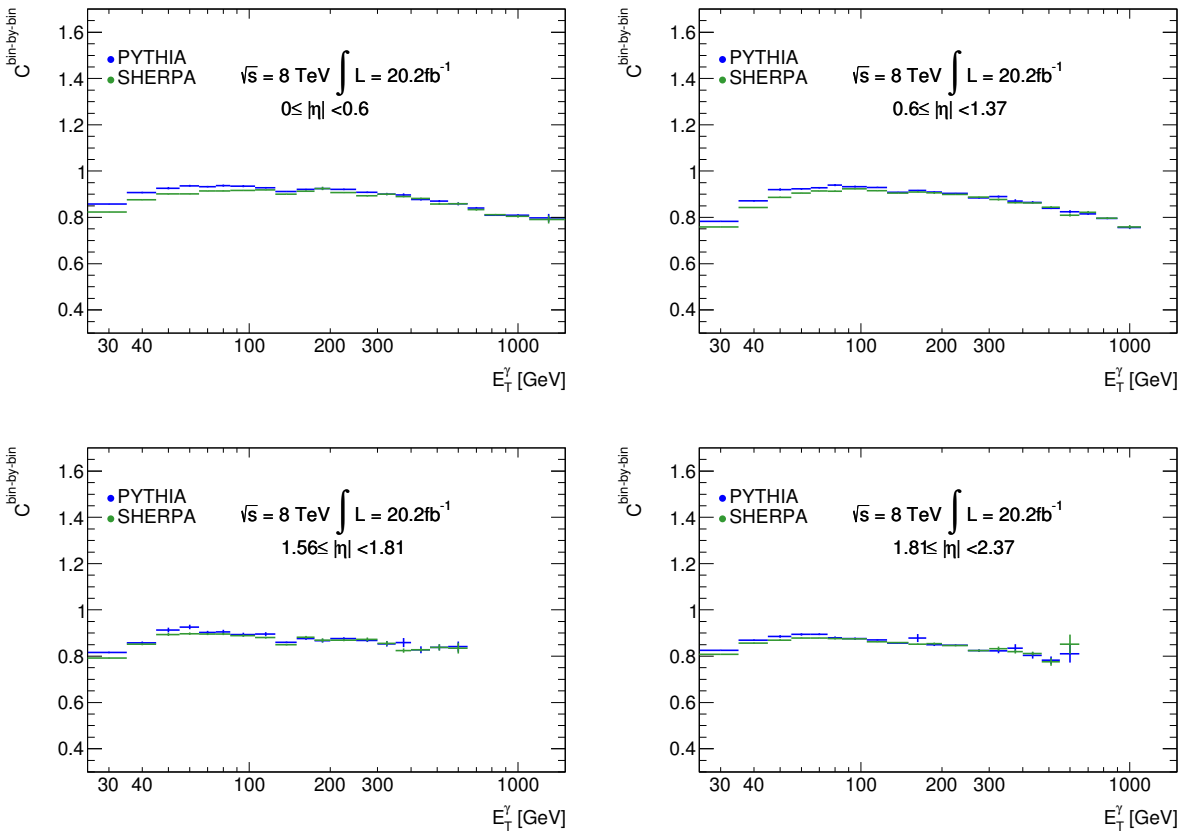

Figure 6–1: Bin-by-bin correction factors as a function of E_{T}^{γ} and in four different η regions. The correction factors are obtained using PYTHIA (blue) and SHERPA (green) simulated samples.

CHAPTER 7
Statistical and Systematic Uncertainties

In order to allow the final cross-section results to be interpreted and their impact assessed, it is necessary to assign an uncertainty to the measurement. This chapter introduces all relevant uncertainties considered as part of the cross-section measurement, along with sources of uncertainties that have been found to be negligible following thorough investigation. A re-sampling technique followed by a smoothing procedure is employed to minimize statistical fluctuations in the estimate of the effect of different sources of systematic uncertainties.

7.1 Smoothing Technique

To minimize statistical fluctuations in the estimate of the effect of different sources of systematic uncertainties a "smoothing" procedure is employed. For each source of systematic uncertainty the statistical component is estimated using a so-called "Bootstrap" method explained in Reference [68]. This method uses a re-sampling technique to estimate the statistical uncertainty component of the systematical shift.

Based on the size of this statistical component, the relative uncertainty distribution ([nominal-shifted]/nominal) is re-binned into fewer bins until statistically significant[1] deviations from the original relative uncertainty distribution are observed. Afterwards, the re-binned relative uncertainty distributions are smoothed using a gaussian kernel smoothening algorithm employed already in other ATLAS measurements [69].

7.2 Statistical Uncertainty

The statistical uncertainty on the cross-section measurement originates from the finite number of photon events measured in data and the number of simulated MC events. The number of simulated MC events is taken into account within the background subtraction method, that partially relies on MC simulation, and the unfolding procedure which is fully based on MC simulation (see Section 6). The statistical uncertainty associated with the finite size of the data as well as the number of simulated MC events is taken to be the standard deviation of a Poisson distributed process with N number of observed occurrences. The large number (order of millions) of generated MC events ensures that the statistical uncertainty arising from the number of simulated MC events amounts to less than 1 % for all E_{T}^{γ} and η bins of the measured cross-section.

[1] The deviation is considered significant with respect to the size of the statistical uncertainty component.

7.3 Systematic Uncertainties

This section presents the different sources of systematic uncertainties considered in the cross-section measurement. The different sources of systematic uncertainties are presented in approximate decreasing order of importance.

- Uncertainty on the integrated luminosity: The uncertainty on the integrated luminosity is derived by the ATLAS luminosity working group. A value of $\pm 2.8\%$ [70] is extracted based on a preliminary calibration of the luminosity scale derived from beam-separation scans performed in November 2012. The extraction follows the same methodology as that detailed in Reference [70].

- Photon energy scale and energy resolution uncertainty: Estimates of the uncertainty on the photon energy scale and resolution are derived centrally by the photon performance group of the ATLAS collaboration [63]. The effect of different sources contributing to the overall energy scale and resolution uncertainties are reported as nuisance parameters that need to be accounted for in the analysis presented here. For each nuisance parameter of the photon energy scale the energy of the photon is varied up and down by the size of the assigned uncertainty. The nuisance parameters of the energy resolution are accounted for by varying the nominal photon energy by an amount determined by a random number drawn from a Gaussian distribution centred at zero with standard deviation equal to the size of the assigned uncertainty. Correlations are taken into account through the nuisance parameters as they are split into an uncorrelated and a fully correlated contribution for each individual uncertainty source.

The E_{T}^{γ} distribution of each uncertainty component is individually smoothed, and is added in quadrature to obtain the total energy scale and resolution uncertainties. The resulting uncertainty is presented in Figure 7–1.

- Uncertainty arising from variations in the relative fraction of direct and fragmentation photons in simulated samples: As previously outlined in Section 5.1, MC simulated samples are used to estimate the signal leakage fractions and to unfold detector effects. Both the signal leakage fractions and the unfolding factors depend on the relative fraction of photons produced through fragmentation. In `PYTHIA`, photons originating from fragmentation processes are generated as part of the final state radiation step, and not as part of the hard scattering. It is therefore possible in the `PYTHIA` simulation to vary the relative fraction of photons originating from fragmentation. The precise fraction of fragmentation photons in data is unknown. In order to estimate its impact on the cross-section measurement, the analysis is performed for two different values of photon fragmentation fraction; either zero, or twice the default fraction used in `PYTHIA`. The size of the variation is chosen based on the change in fragmentation fraction in the MC required to best match the data. Changes in the measured cross-section are taken as the systematic uncertainty associated with the relative fraction of fragmentation to direct photons. Figure 7–2 shows this systematic uncertainty as function of E_{T}^{γ}. Note that the final cross-section measurement is based on the default fraction of fragmentation photons in `PYTHIA` implemented by the authors. Variations in the fragmentation photon fraction only impacts the measured cross-section in the region $E_{\mathrm{T}}^{\gamma} < 200$ GeV.

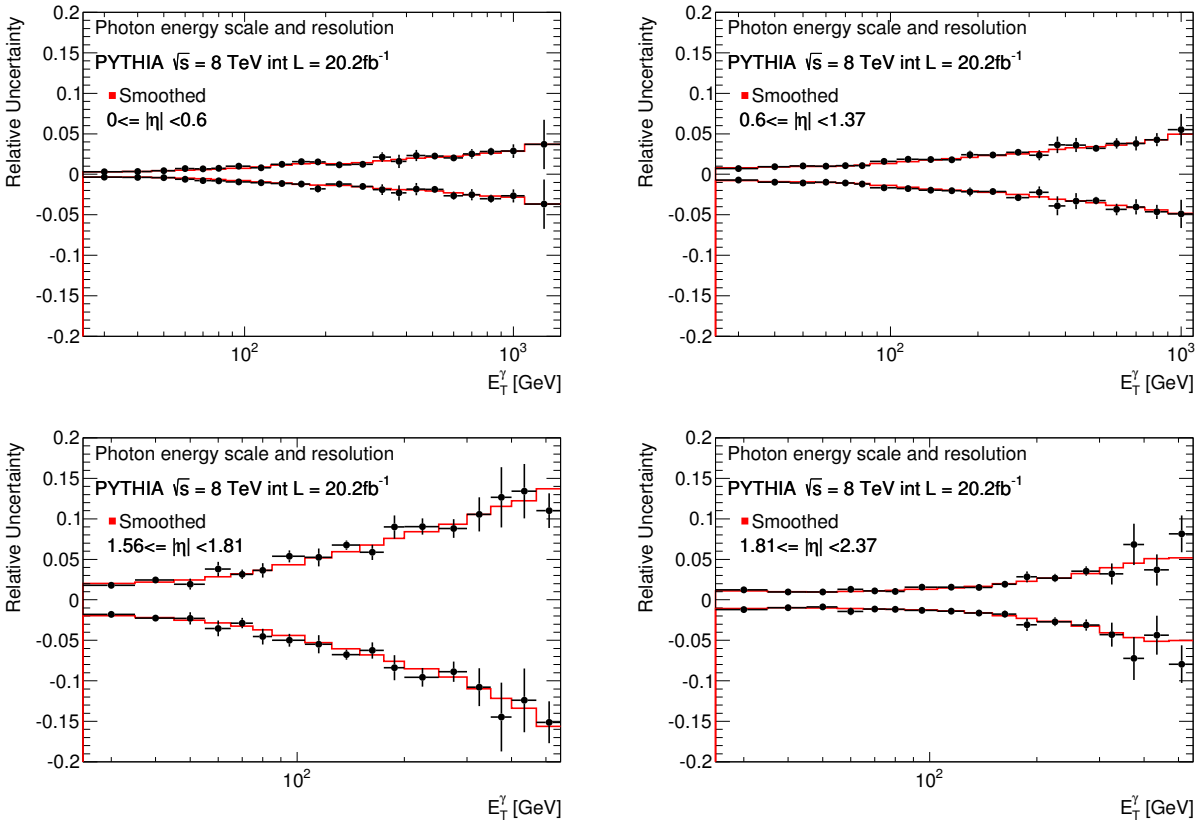

Figure 7–1: Relative systematic uncertainty on the measured photon cross-section arising from varying the photon energy scale and resolution by their individual uncertainty components up and down. The relative uncertainty is presented as a function of E_{T}^{γ} and the four different η regions considered in the analysis. The total uncertainty on the photon energy scale and resolution is obtained by combining the uncertainties from each individual component taking into account measured correlations.

The impact is also shown to be independent of the pseudorapidity region considered. The uncertainty varies from approximately 7% in the first E_{T}^{γ} bin $(25-35\ \mathrm{GeV})$ to 0% for $E_{\mathrm{T}}^{\gamma} > 200\ \mathrm{GeV}$.

- Uncertainty associated with possible correlations between the transverse isolation energy and photon candidate shower shape in background events: The 2D background subtraction method introduced in Section 5.1 relies on the assumption that there are no correlations between values of transverse isolation energy and photon shower shape in background events. This assumption is equivalent to taking $R^{\mathrm{bkg}} = 1$ for the estimation of the number of background events in the signal region (region A). The quantity R^{bkg} can be calculated directly in simulated events with the knowledge of which event is a background or signal event. To estimate R^{bkg} in data requires the definition of four kinematic regions of background-enriched events. To do so, a second transverse isolation energy requirement of $E_{\mathrm{T}}^{\mathrm{iso}} \geq 17.8\ \mathrm{GeV} + (4.2 \times 10^{-3}) \times E_{\mathrm{T}}^{\gamma}\ [\ \mathrm{GeV}]$ is introduced to define Regions E and F as shown in Figure 7–3. The number of data events falling in regions B,D,E and F is used to estimate R^{bkg} as function of E_{T}^{γ}. The study of R^{bkg} both in data and simulated event samples found the value of R^{bkg} to be consistent with unity within 10 % in the kinematic region of the cross-section measurement presented here. The measured values of R^{bkg} as a function of E_{T}^{γ} are shown in Appendix E.

  The impact on the cross-section measurement of changing the nominal value of $R^{\mathrm{bkg}} = 1$ by $\pm 10\,\%$ is shown in Figure 7–4. The uncertainty is largest in the lower E_{T}^{γ} region due to the smaller sample purity used for background

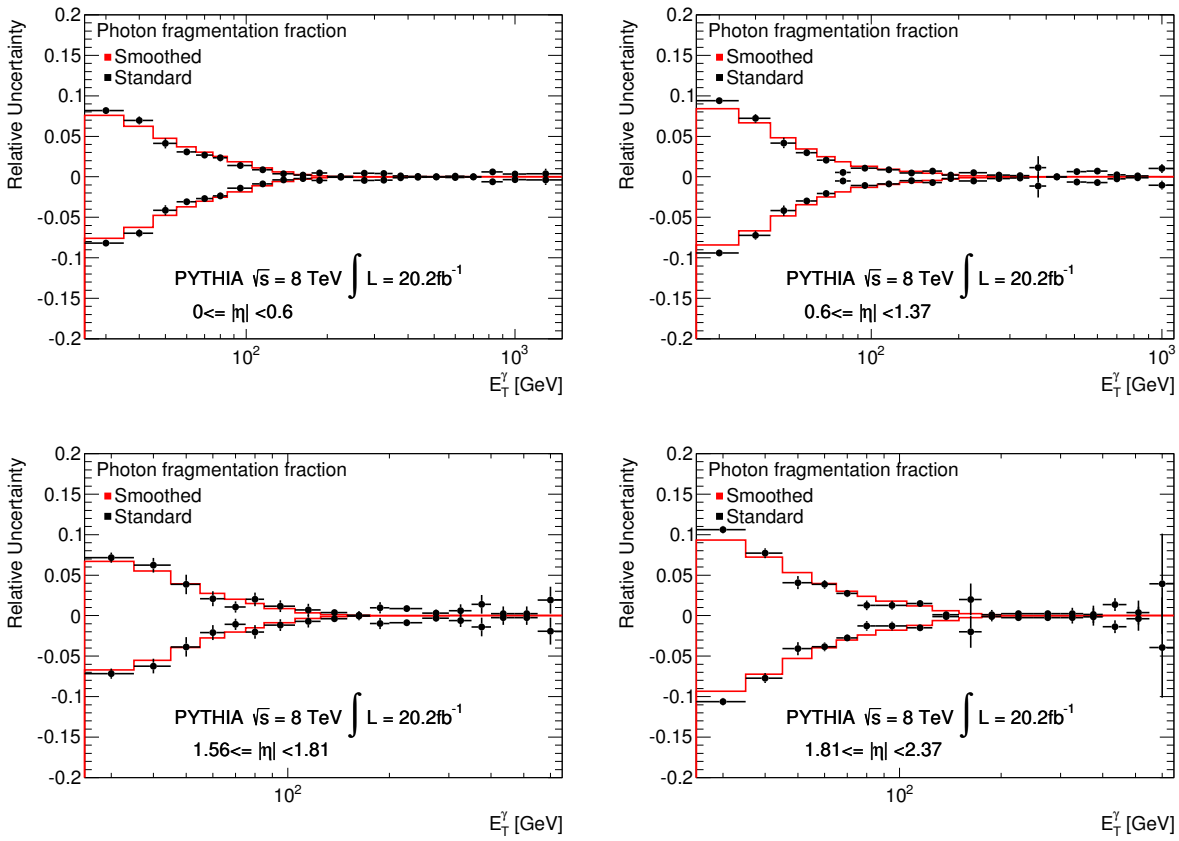

Figure 7–2: Relative uncertainty on the measured photon cross-section based on varying the fraction of fragmentation to direct photons in the PYTHIA simulation. The relative uncertainty is presented as a function of E_{T}^{γ} and the four different η regions considered in the analysis

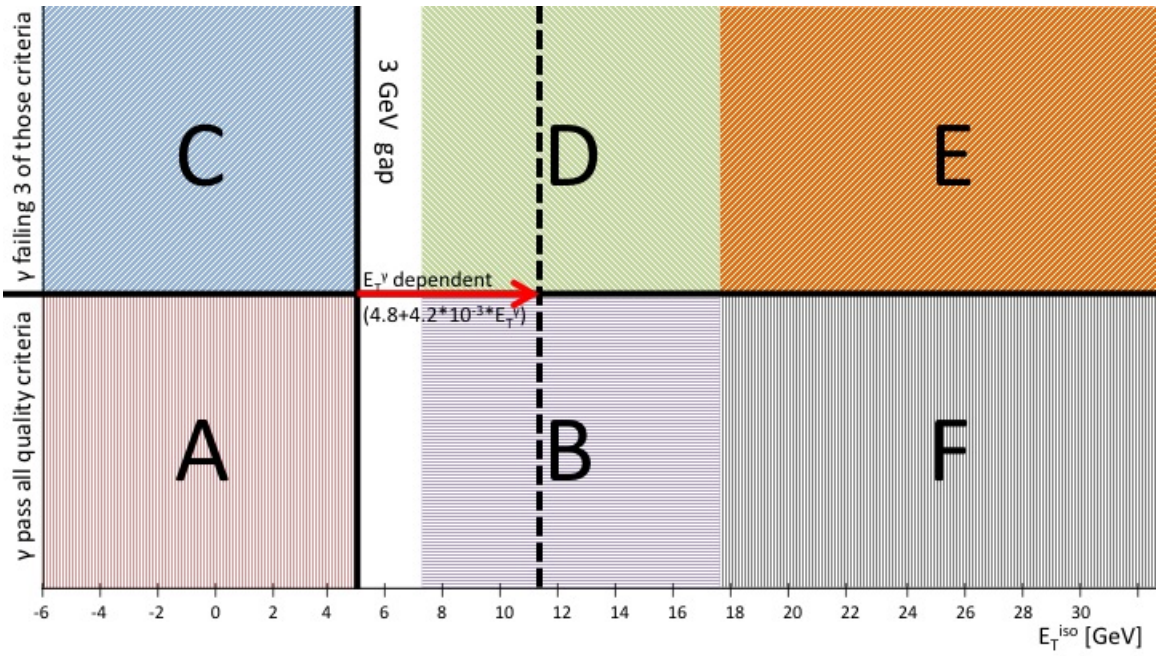

Figure 7–3: Schematic representation of the different kinematic regions defined for the data-driven estimate of R^{bkg}. The dashed line represents the highest cut value of the E_{T}^{γ}-dependent isolation boundary at $E_{\text{T}}^{\gamma} = 1500$ GeV

subtraction in that region. The uncertainty decreases as function of increasing E_{T}^{γ}, from approximately 10% to 0% for $E_{\mathrm{T}}^{\gamma} > 300$ GeV.

- Uncertainty arising from the choice of requirements on the shower shape variables defining the control regions in the 2D sideband method: Considering that the background subtraction method adopted for this analysis relies on the definition of control regions, uncertainties arise from the particular choice of these control regions. As outlined in Section 5.1, one boundary of the control regions is defined by whether or not the leading photon fails the requirements on at least one of three chosen shower shape variables. In order to assess the uncertainty arising from the choice of variables used to define a region enhanced in fake photons, the cross-section is measured using two other choices of variables: whether or not the leading photon fails the requirements on a fourth shower shape variable (w_{η_2}), and whether or not the leading photon fails the selection on only one shower shape variables (F_{side}). The change to a different set of variables to define the region enhanced in fake photons leads to a change of R^{bkg} used for the background subtraction. In order to avoid double-counting of the uncertainties this variation needs to be accounted for. The change of R^{bkg} can be measured in data by comparing the new $R_{\mathrm{var}}^{\mathrm{bkg}}$ value to the nominal value of R^{bkg}.

$$R_{\mathrm{var}}^{\mathrm{bkg}} = R^{\mathrm{bkg}} \frac{R_{\mathrm{var}}^{\mathrm{bkg}}}{R^{\mathrm{bkg}}} \tag{7.1}$$

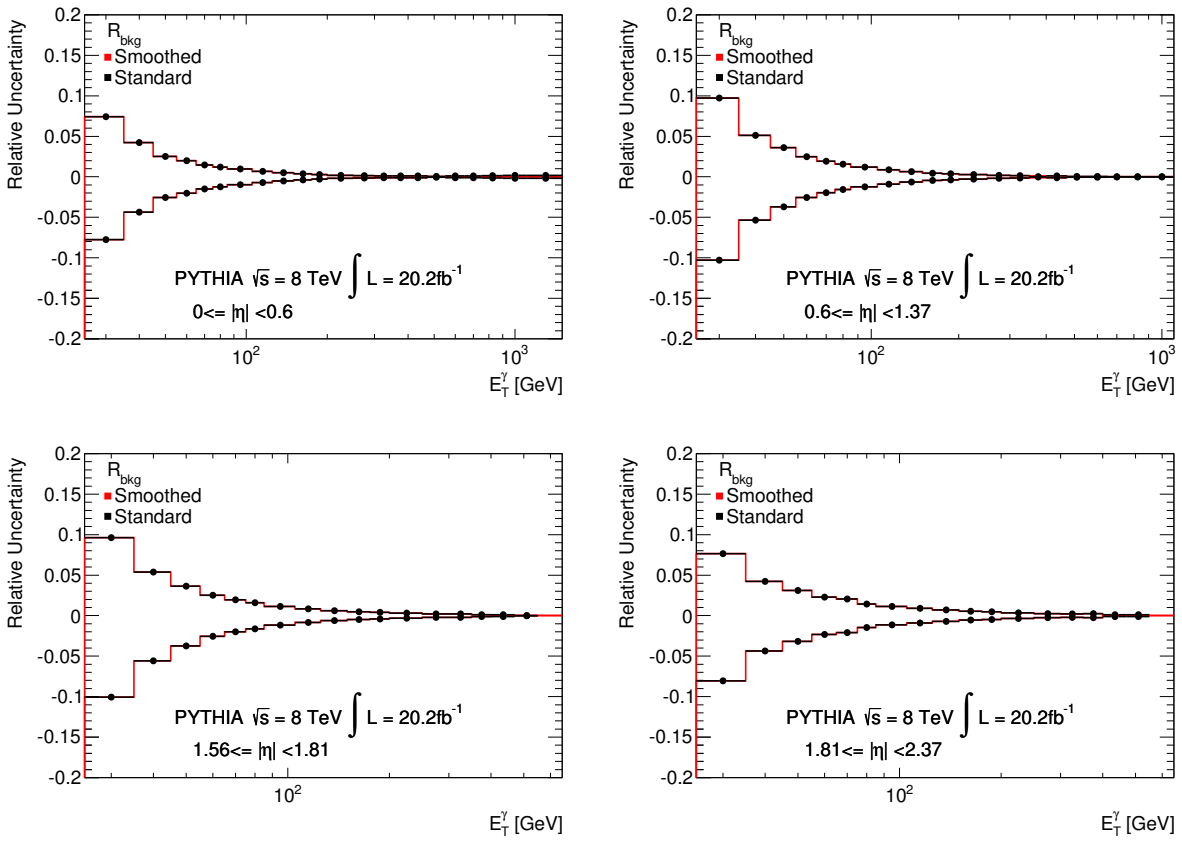

Figure 7–4: Relative uncertainty on the measured photon cross-section arising from varying the background correlation factor (R^{bkg}) up and down by 10 %. The relative uncertainty is presented as a function of E_{T}^{γ} and the four different η regions considered in the analysis.

The nominal value of R^{bkg} as previously discussed is set to 1 and therefore the ratio of $R^{\text{bkg}}_{\text{var}}$ and R^{bkg} is equal to the value of $R^{\text{bkg}}_{\text{var}}$. The ratio of $R^{\text{bkg}}_{\text{var}}$ and R^{bkg} only depends on regions C and D which have almost no contamination from signal photons (especially at low E^{γ}_{T}), allowing for a data-driven measurement of this ratio. The ratio is found to be flat as a function of E^{γ}_{T} with values between 1.1 and 1.2 for the four different $|\eta|$ regions. In order to account for changes in the value of R^{bkg}, the extracted ratio values are used to calculate the uncertainty associated to the change in cross-section when using a different definition of cuts to define the control region.

The resulting uncertainty on the particular choice of shower shape variables for the control region is presented in Figure 7–5. Similarly to the previous uncertainty, as this one also effects the signal purity; the uncertainty is largest in the lower E^{γ}_{T} region due to the smaller sample purity used for background subtraction in that region. The uncertainty decreases as a function of increasing E^{γ}_{T}, from approximately 2% to 0% for $E^{\gamma}_{\text{T}} > 200$ GeV.

- Uncertainty arising from the choice of requirement on the transverse isolation energy defining the control regions in the 2D sideband method: Another uncertainty (within the 2D-sideband method) arises from the chosen $E^{\text{iso}}_{\text{T}}$ cut that defines the second boundary of the control regions. The uncertainty is estimated by varying the E^{γ}_{T}-dependent isolation cut of the control region up and down by 1 GeV ($E^{iso,\gamma}_{\text{T}} \geq (7.8 \pm 1)$ GeV $+ (4.2 \times 10^{-3}) \times E^{\gamma}_{\text{T}}$ [GeV]). A change in the definition of the boundary between control regions affects the calculated signal sample purity, and therefore the final cross-section measurement. The

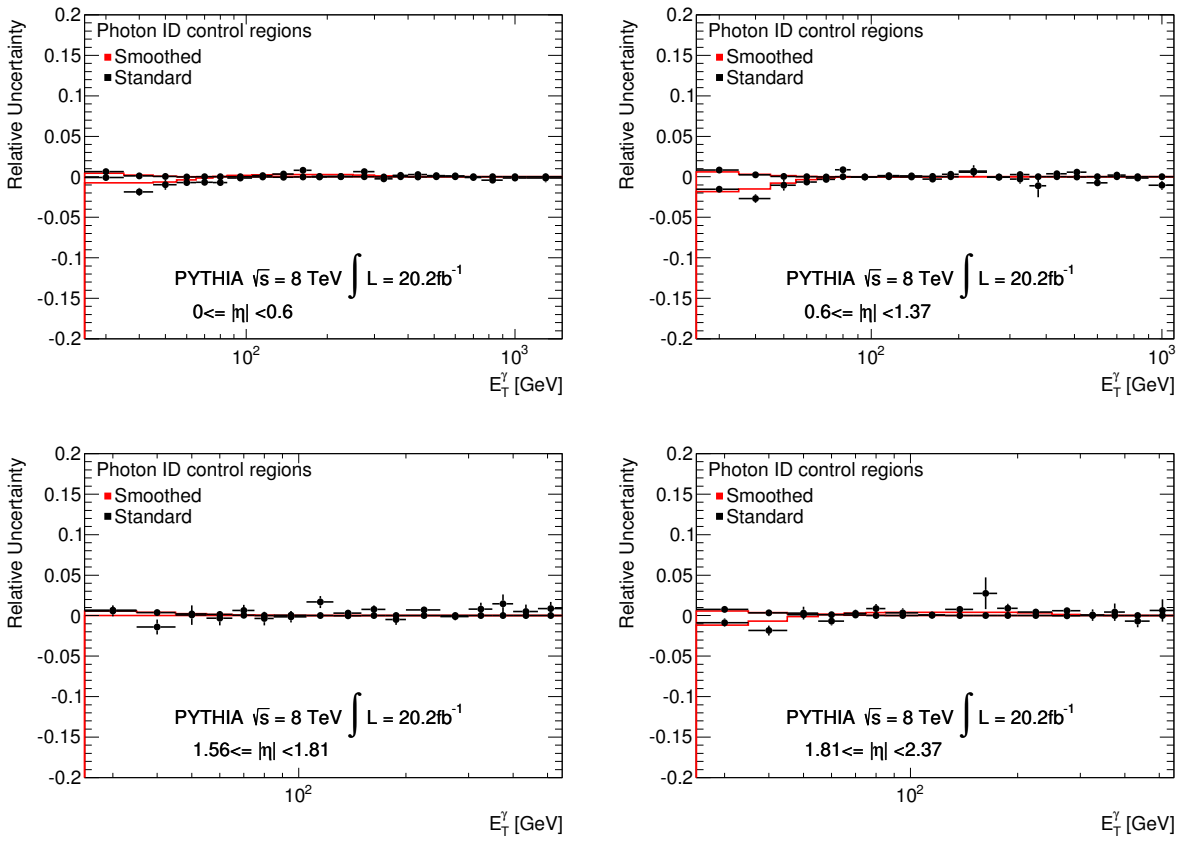

Figure 7–5: Relative uncertainty on the measured photon cross-section associated with the definition of the background enriched control regions of photons explicitly not fulfilling some of the quality requirements. The relative uncertainty is presented as a function of E_{T}^{γ} and the four different η regions considered in the analysis.

resulting effect on the nominal cross-section measurement as a function of E_{T}^{γ} is presented in Figure 7–6. The uncertainty on the choice of transverse isolation energy requirement in the definition of the control regions is below 0.5% over the entire kinematic region considered.

- Uncertainty on photon identification efficiency: Event weights are applied to MC simulated events in order to obtain a photon identification efficiency that is statistically consistent with that measured in data. As explained in Section 4.3.5, these event weights are extracted by the photon performance group [71] by comparing different data-driven photon-identification efficiency measurements with simulation. The uncertainty on the event weights reflects the spread of those different measurement methods and their individual uncertainty. The event-weight uncertainty is propagated through the analysis to the final cross-section measurement and its relative size is shown in Figure 7–7.

  An additional uncertainty is considered since the event weights were derived by the photon performance group using a fixed cut value on the isolation transverse energy ($E_{\mathrm{T}}^{\mathrm{iso}} < 4$ GeV). The analysis presented here uses instead a E_{T}^{γ}-dependent $E_{\mathrm{T}}^{\mathrm{iso}}$ cut value. Therefore, an additional uncertainty is considered to account for the difference in the photon candidate definition used in the derivation of the MC event weights. This additional uncertainty is extracted from MC, by taking the difference in the photon identification efficiency between the E_{T}^{γ}-dependent isolation cut and the fixed cut value of $E_{\mathrm{T}}^{\mathrm{iso}} < 4\,\mathrm{GeV}$. The resulting uncertainties as a function of E_{T}^{γ} are below 0.5% except for $E_{\mathrm{T}}^{\gamma} > 900$ GeV in the pseudorapidity region below 0.6 where it reaches approximately 1%.

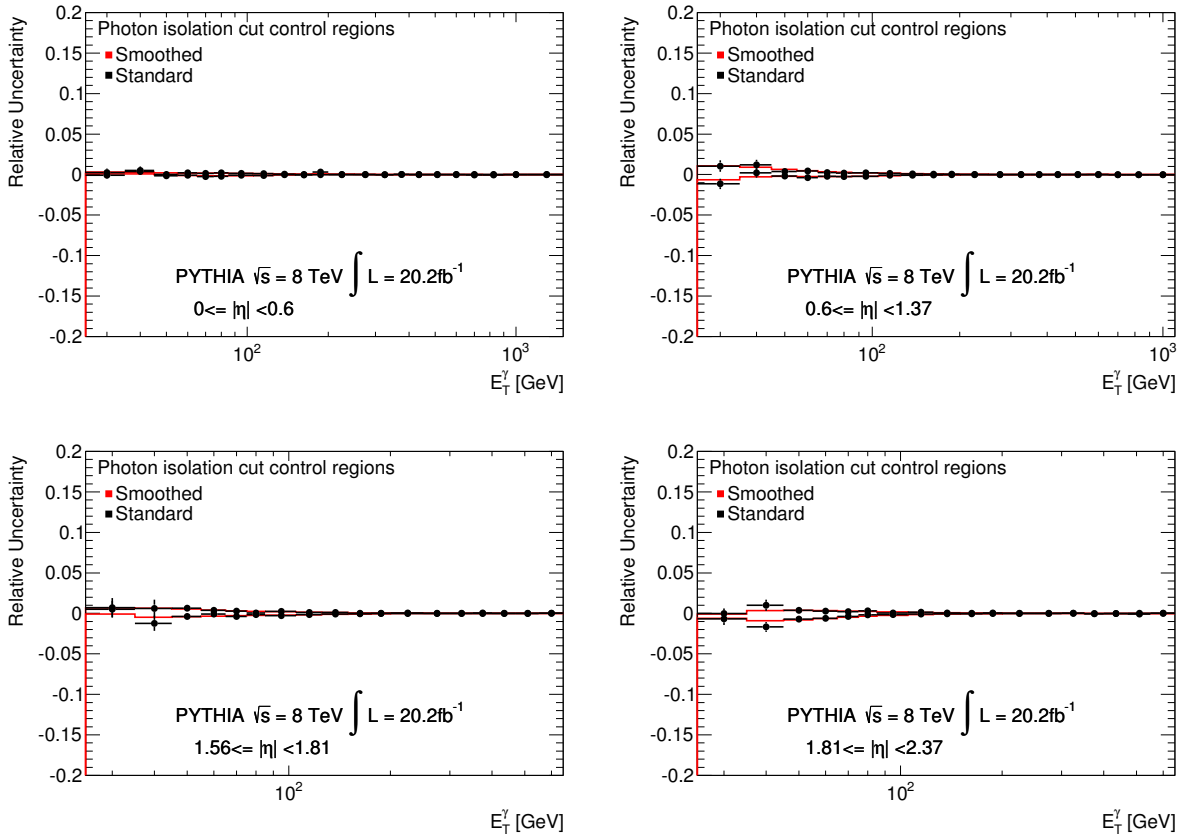

Figure 7–6: Relative uncertainty on the measured photon cross-section based on varying the transverse energy dependent isolation cut of the control region up and down by 1 GeV ($E_{\mathrm{T}}^{iso,\gamma} \geq (7.8 \pm 1)$ GeV $+ (4.2 \times 10^{-3}) \times E_{\mathrm{T}}^{\gamma}$). The relative uncertainty is presented as a function of E_{T}^{γ} and the four different η regions considered in the analysis.

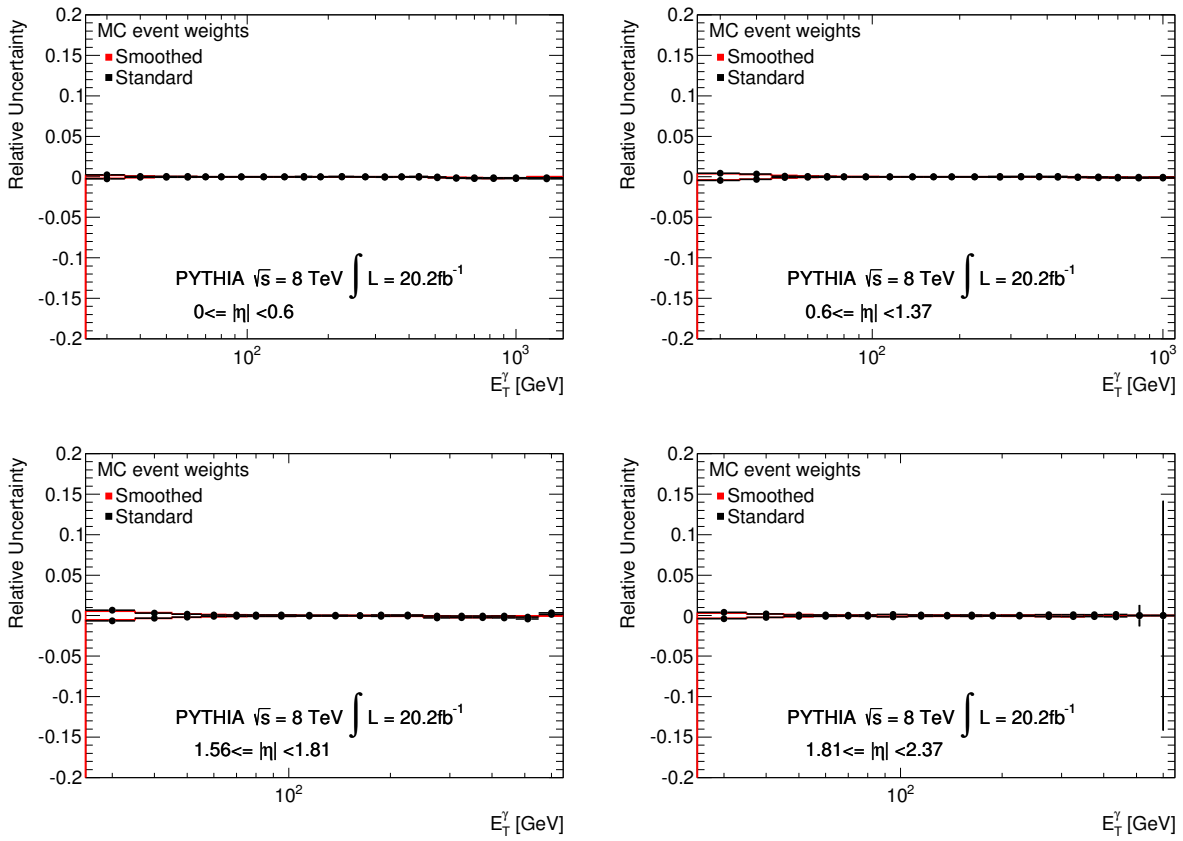

Figure 7–7: Relative systematic uncertainty on the measured photon cross-section arising from the uncertainty on the event weights applied to the MC to match the identification efficiency between data and MC. The relative uncertainty is presented as a function of E_{T}^{γ} and the four different η regions considered in the analysis.

- Trigger efficiency uncertainty: The trigger efficiencies of all single photon triggers relevant to this analysis have been measured to be above 99.6 % in the E_{T}^{γ} range they are used. As presented in Section 3.2.5, trigger efficiencies are measured with a statistical uncertainty of less than 0.1 %. Although the measured trigger efficiencies are used to correct the observed number of data events, their statistical uncertainties are considered negligible and therefore do not contribute to the final measured cross-section uncertainty.

- Pile-up uncertainty: Possible biases associated with the changing pile-up conditions during the 2012 data-taking period were estimated by splitting the data and MC events into two sub-samples, one consisting of events with less than 15 interactions per beam crossing and one sub-sample with more than 25 interactions per beam crossing. The cross-section measurements obtained with each sub-sample are compared and found to be consistent within statistical uncertainties.

- Uncertainty arising from the unfolding method's dependence on the shape of the E_{T}^{γ} simulated distributions.: As a cross-check and to estimate the dependence of the unfolding to a difference in the shape of the E_{T}^{γ} distribution between data and MC simulated events, the MC events are reweighted using a smoothing function matching the data distribution. Measurements of the cross-section are found to change by less than 0.1 % and this uncertainty is therefore considered negligible. The investigation of this uncertainty was not performed by the author, however it was independently cross-checked that the effect is negligible.

- Uncertainty on the transverse isolation energy correction applied to MC simulated samples: The transverse isolation energy of simulated MC events is shifted by a $(\Delta\eta^{\gamma}, E_{\mathrm{T}}^{\gamma})$ dependent correction factor to ensure that the mean of the $E_{\mathrm{T}}^{\mathrm{iso}}$ distribution agrees with that observed in data. The correction factors are obtained from the difference between the data and MC means of the $E_{\mathrm{T}}^{\mathrm{iso}}$ distributions. The means are extracted from a fit of the $E_{\mathrm{T}}^{\mathrm{iso}}$ distributions to a smoothed function. The $E_{\mathrm{T}}^{\mathrm{iso}}$ MC corrections are varied by the equivalent of two times the fit uncertainty used to calculate the mean value of the distributions. This yields differences in the measured cross-section of less than 0.1 % over the entire kinematic region considered. This effect is therefore considered negligible. The detailed study of the shift values and their uncertainties was not performed by the author, however it was independently cross-checked that the effect is negligible.

- Uncertainty associated to parton shower and hadronization models: `PYTHIA` and `SHERPA` use different parton shower and hadronization models. A modelling uncertainty is estimated by taking the difference in measured cross-section obtained with each type of MC sample. To avoid double-counting systematic effects associated with the photon fragmentation fraction in `PYTHIA`, a special `PYTHIA` sample was prepared in which the photon fragmentation fraction was adjusted to best match the E_{T}^{γ} distributions in data. Cross-section measurements obtained with this optimized `PYTHIA` sample are compared with

those obtained by SHERPA. The resulting uncertainty decreases with increasing E_{T}^{γ}, from a value of approximately 2% for $25 - 35$ GeV down to 0% for $E_{\mathrm{T}}^{\gamma} > 100$ GeV.

A summary of the main contributions to the total systematic uncertainty as a function of E_{T}^{γ} is presented in Figure 7–8. At high E_{T}^{γ}, the total uncertainty is mostly dominated by the uncertainty on the photon energy scale. Even though the energy scale uncertainty is relatively small and flat at approximately 1 % for $E_{\mathrm{T}}^{\gamma} > 200$ GeV an increasing impact on the cross-section as a function of E_{T}^{γ} is measured. This effect is understood since the cross-section is measured in finite bin sizes of E_{T}^{γ}. Each bin represents the summation of all events falling in the defined E_{T}^{γ} bin range. The number of events in this measurement is strongly decreasing as a function of E_{T}^{γ}, therefore the number of events close to the lower E_{T}^{γ} boundary of the bin will be much higher than at the high one. A relative shift such as the energy scale uncertainty will therefore be enhanced since more events are shifted in/out at the lower edge of the bin compared to the higher one. In addition, larger bin sizes enhance the effect since this increases the different number of events contributing to each E_{T}^{γ} bin boundary. At low E_{T}^{γ} the uncertainties arising from the unknown fraction of fragmentation to direct photons and from sensitivity to changes in R^{bkg} value are the dominant contributions to the total systematic uncertainty. In addition, the E_{T}^{γ} independent uncertainty of the integrated luminosity of ± 2.8 % is shown but not included in the calculation of the total uncertainty.

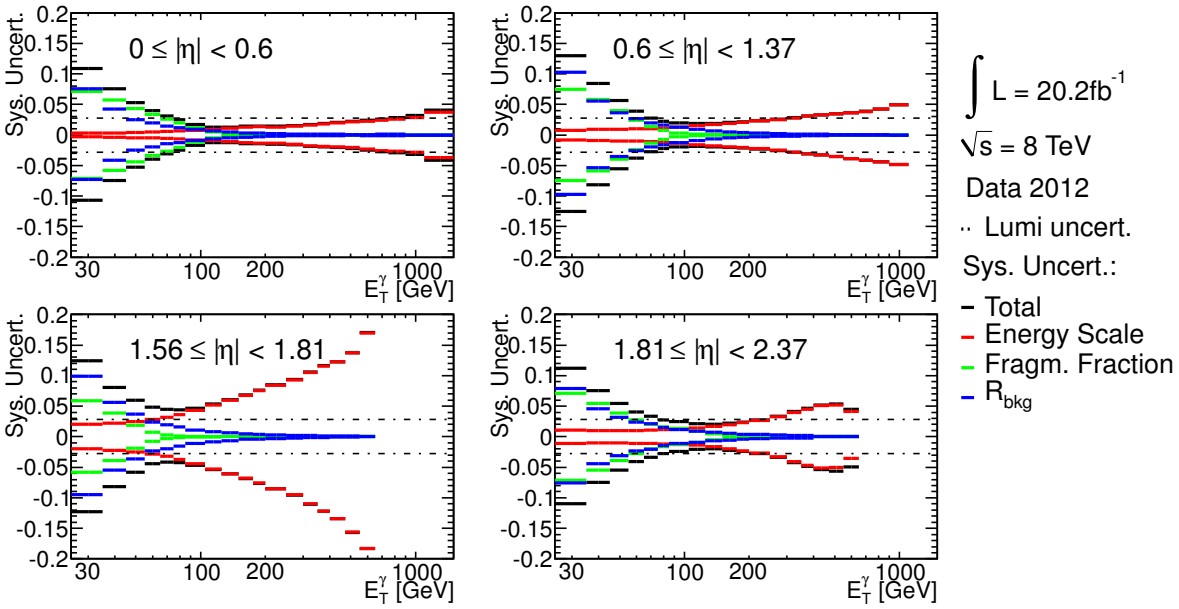

Figure 7–8: Summary plot of the main systematic uncertainties contributing to the measurement presented in this thesis. The summary of the main systematic uncertainties is presented as a function of E_{T}^{γ} and the four different η regions considered in the analysis.

7.4 Uncertainties Associated to NLO Calculations

Uncertainties associated to the NLO calculations are extracted by generating large samples using the same NLO generator, while changing the input of the source of systematic uncertainty.

- The scale uncertainties are evaluated by varying the renormalization, factorization and fragmentation scales[2] independently and coherently to values of $E_{\mathrm{T}}^{\gamma}/2$ and $2E_{\mathrm{T}}^{\gamma}$. This procedure to estimate the size of scale uncertainty is motivated by Reference [72]. Relative differences in the simulated E_{T}^{γ} distributions due to each scale variation are added in quadrature. The combined scale uncertainty is found to be approximately 20 % at the high and low end of the measured E_{T}^{γ} spectrum with a minimum of 12 % at around 150 GeV.

- The PDF uncertainty on the differential cross-section due to insufficient knowledge of the PDFs is obtained by repeating the `JETPHOX` calculations for 52 eigenvector sets of the CT10 PDF and applying a scaling factor in order to obtain the uncertainty for the 68% confidence-level (CL) interval [72]. The corresponding uncertainty on the cross-section increases with E_{T}^{γ} and varies between 5% at $E_{\mathrm{T}}^{\gamma} \simeq 100$ GeV and 15% at $E_{\mathrm{T}}^{\gamma} \simeq 900$ GeV.

[2] The nominal value of the scale factors is set to be equal to the transverse energy of the photon.

- The uncertainty due to the value of the strong coupling constant α_s used in the NLO calculation is evaluated following the recommendation of Reference [73]. The `JETPHOX` prediction (CT10 PDF) was repeated with α_s values varied by ± 0.002 around the central value of 0.118 and then scaled to obtain an uncertainty that corresponds to a 68% CL interval. The α_s uncertainty on the differential cross-section is flat at approximately 10 % over the entire E_{T}^{γ} range in the barrel region ($|\eta| < 1.37$) with the exception of the region $E_{\mathrm{T}}^{\gamma} > 1100$ GeV where the uncertainty increases to 15 %. In the forward region ($1.56 \leq |\eta| < 2.37$) the α_s uncertainty on the differential cross-section decreases from approximately 10 % to 1 % as a function of E_{T}^{γ}.

- The uncertainty arising from hadronization and underlying event correction factors is evaluated using two alternative hadronization and underlying event models: `PYTHIA` which uses a LUND string model [57] of hadronization, and `SHERPA` samples produced using a modified version of the cluster hadronization model [60]. The study is performed with the same photon isolation cuts as the main analysis ($\Delta R = 0.4$ and the E_{T}^{γ}-dependent cut). The hadronization and underlying event correction were found to be close to unity for both models with a small deviation of maximally 2% at low E_{T}^{γ}. For comparisons with the measured cross-section, the hadronization and underlying event correction factor is taken to be 1. An E_{T}^{γ}-dependent uncertainty is however assigned based on the largest deviation from unity between the two models.

CHAPTER 8
Results

This chapter presents the final results of the prompt isolated photon cross-section measurement. The results are compared to LO and NLO theoretical predictions. The measurement is also compared to previous results of prompt photon cross-section measurements.

8.1 Final Cross-Section

The inclusive prompt photon production cross-section is measured as a function of E_{T}^{γ}, in four distinct regions of photon pseudorapidity. In a given η region, the cross-section in each E_{T}^{γ} bin is calculated using

$$\frac{d\sigma}{dE_{\mathrm{T}}^{\gamma}} = \frac{N_{\mathrm{data}} \cdot \frac{1}{\mathrm{PS}} \cdot p_{\mathrm{sig}} \cdot \frac{1}{C^{\mathrm{bin-by-bin}}}}{\int \mathcal{L}dt \cdot \Delta E_{\mathrm{T}}^{\gamma} \cdot \epsilon_{\mathrm{trigger}}}, \tag{8.1}$$

where N_{data} represents the number of events with at least one signal photon, PS is the photon trigger prescale factor for the trigger used to populate events in the particular E_{T}^{γ} bin, p_{sig} represents the purity of the selected signal sample and $C_{\mathrm{bin-by-bin}}$ is the unfolding correction factor. The symbol $\int \mathcal{L}dt$ is the integrated luminosity of $20.2\, fb^{-1}$, $\epsilon_{trigger}$ represents the photon trigger efficiency and $\Delta E_{\mathrm{T}}^{\gamma}$ is the width of the transverse energy bin in GeV.

The measured cross-section as a function of E_{T}^{γ} is presented in Figure 8–1 for the four relevant η regions. The measurement is compared to NLO predictions obtained with `JETPHOX` using the CT10 PDF set. For illustration purposes the cross-section values in the different η regions are scaled by the scale factors shown on the plot. The statistical and systematic uncertainties of the measured cross-section as well as the uncertainties on the NLO predictions are included but generally too small to be visible. The good agreement of the measured cross-section as a function of E_{T}^{γ} with the NLO predictions in all four pseudorapidity regions can be seen. The measured cross-section value in each (E_{T}^{γ}, η) bin and its corresponding statistical and systematic uncertainties are tabulated in Appendix C.

In order to better visualize the large range of cross-section values over several orders of magnitudes, ratios of the predicted to the measured cross-section are presented in Figure 8–2. The statistical uncertainty of the data is represented by the small horizontal lines visible on some of the vertical error bars. The total (statistical and systematic) uncertainty on the measured cross-section is shown as the full error bar. The total uncertainty on the NLO predictions is shown as a grey band which includes the scales, PDF, α_s, and hadronization and underlying event uncertainties. The largest component to the total uncertainty, the scales (μ_R, μ_F and μ_f) uncertainty, is shown separately as the light grey portion of the total uncertainty band. The NLO theoretical predictions are able to reproduce the magnitude and E_{T}^{γ} dependence of the measured cross-section in all four η regions within uncertainties. Slightly smaller cross-section values ($10 - 15\,\%$) are predicted up to E_{T}^{γ} of approximately 650 GeV. The difference reduces for higher transverse photon energies. For

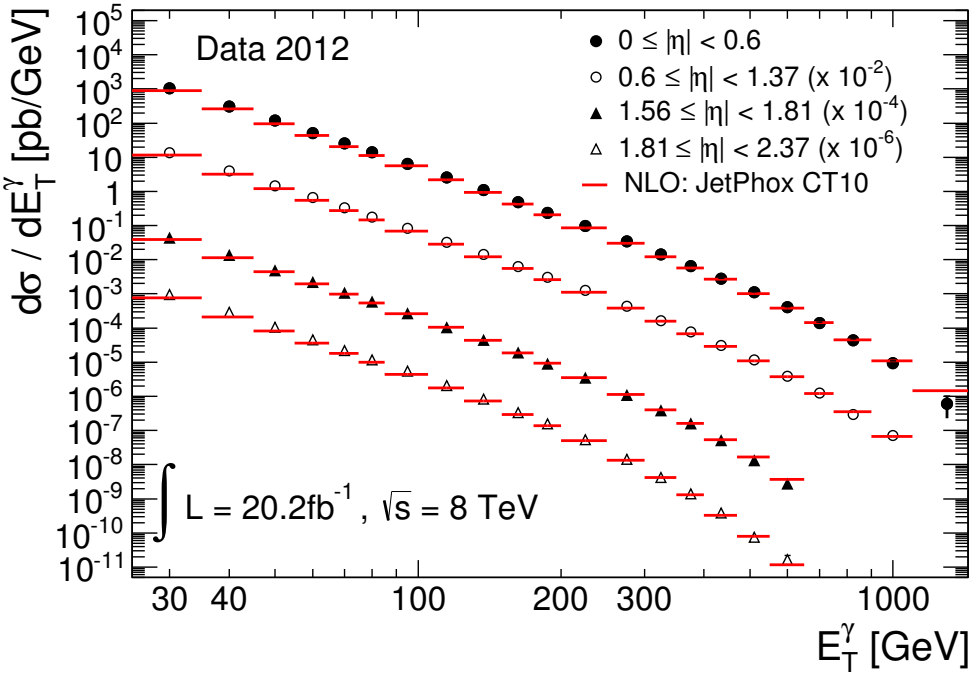

Figure 8–1: Differential cross-section as a function of E_{T}^{γ} in four η regions (scaled, for presentation purposes, by the factors specified in the legend). The measurements (markers) are compared to NLO predictions obtained with `JETPHOX` using the CT10 PDF set. The statistical and systematic uncertainties of the measured cross-section as well as the uncertainties on the NLO predictions are included but generally too small to be visible.

the very highest photon energies $1100 \leq E_{\mathrm{T}}^{\gamma} < 1500$ the prediction overestimates the measurement. The good description of the E_{T}^{γ} dependence by JETPHOX, especially in the region $E_{\mathrm{T}}^{\gamma} < 300$ GeV indicates that the fragmentation fraction is well reproduced by the predictions. The fragmentation fraction itself is E_{T}^{γ} dependent and dominates the region $E_{\mathrm{T}}^{\gamma} < 300$ GeV, thereby affecting the overall E_{T}^{γ} dependence of the cross-section measurement. Apart from the statistically dominated high transverse energy region, the uncertainties on the measured cross-section are smaller than the theoretical uncertainties. The theoretical uncertainties are mainly constant as a function of E_{T}^{γ} with a size of approximately 15 %. The experimental uncertainties decrease as a function of E_{T}^{γ} from around 12 % at $E_{\mathrm{T}}^{\gamma} = 25$ GeV to a few percent[1] up to the statistically dominated high E_{T}^{γ} regions of the measured cross-section.

Comparisons of the measured cross-section to LO (PYTHIA and SHERPA) predictions are also presented in Figure 8–2. Both LO MC generators are able to reproduce the magnitude and shape of the measured cross-section as a function of E_{T}^{γ} in the four η regions. For photons with lower transverse energy ($E_{\mathrm{T}}^{\gamma} < 200$ GeV) increasing deviations from the measured cross-section value can be observed. SHERPA tends to underestimate whereas PYTHIA to overestimate the measured cross-section. The fragmentation fraction is the highest in this region of transverse photon energy. The

[1] In the region $1.56 \leq |\eta| < 1.81$ the larger energy scale uncertainty increases the experimental uncertainty by approximately 3% compared to the other pseudorapidity regions.

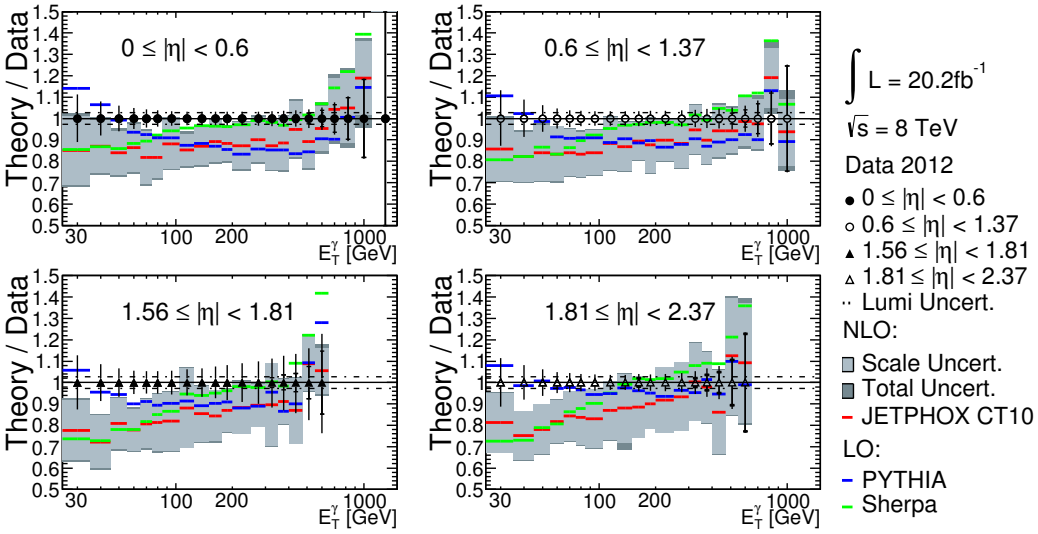

Figure 8–2: Ratio of predicted to measured cross-section as function of E_{T}^{γ} in four η regions. The black markers represent the data and the combined statistical and systematic experimental uncertainty on the measurement. The statistical component of the uncertainty is indicated by a small horizontal tick mark visible on some of the vertical error bars. The measured cross-section is compared to both LO and NLO predictions. The total uncertainty on the NLO predictions is shown as a grey band which includes the scales, PDF, α_s, and hadronization and underlying event uncertainties. The largest component to the total uncertainty, the scales (μ_R, μ_F and μ_f) uncertainty, is shown separately as the light grey portion of the total uncertainty band.

limitation in the description of the fragmentation photons at leading-order is likely the source of this trend.

Comparisons of the measured cross-section and NLO predictions obtained using different input PDFs are shown in Figure 8–3. The relatively large total theoretical uncertainty, as compared to the small dependence of the predictions on the PDFs, does not make it possible to make any statistically significant distinction between

PDFs. Nevertheless, the improved description of the shape of the differential cross-section, along with reduced experimental uncertainties, should make it possible to use the cross-section measurements to reduce uncertainties on the PDF. For example, the impact of the results on the gluon PDF and its uncertainty can be inferred from a PDF sensitivity study [74] performed using the results of the previous ATLAS measurements [11]. A main limitation is the large scale uncertainty (over 20 %) on the predicted photon cross-section. A reduction of this uncertainty could be provided through next-to-next-to leading order (NNLO) prediction that unfortunately are not yet available for the photon production process.

In this analysis, the differential cross-section as a function of pseudorapidity is not explicitly measured, the reason being that the differential cross-section as a function of η corresponds to the cross-section integrated over the whole E_{T}^{γ} spectrum. Since the cross-section is largest at low E_{T}^{γ}, the η dependence of the cross-section is dominated by events with low transverse energy photons. Therefore, the extended energy reach of the measurement presented here does not provide additional information beyond what was measured in previous ATLAS measurements [9–11]. The division of the measured cross-section as a function of E_{T}^{γ} into four pseudorapidity bins however provides insight into the cross-section dependence on η for different values of E_{T}^{γ}.

8.2 Event Display

In order to ensure the quality of this analysis, 3-dimensional visual representations of all events with $E_{\mathrm{T}}^{\gamma} > 1$ TeV were visually cross-checked to ensure that events

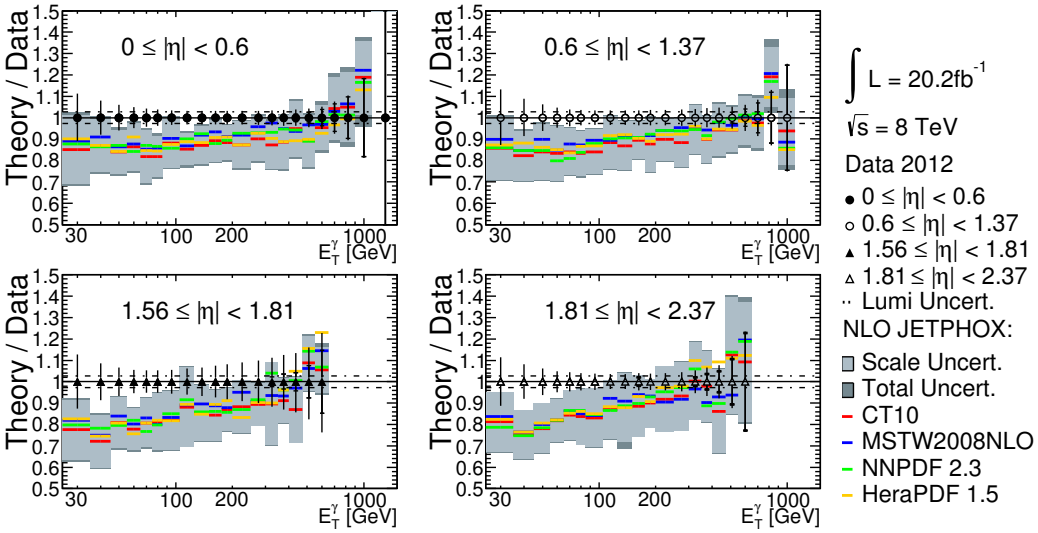

Figure 8–3: The measured cross-section is compared to NLO predictions obtained with JETPHOX using four different PDF sets (CT10, MSTW, NNPDF2.3 and HeraPDF1.5). The black markers represent the data and the combined statistical and systematic experimental uncertainty on the measurement. The statistical component of the uncertainty is indicated by a small horizontal tick mark visible on some of the vertical error bars. The total uncertainty on the NLO predictions is shown as a grey band which includes the scales, PDF, α_s, and hadronization and underlying event uncertainties. The largest component to the total uncertainty, the scales (μ_R, μ_F and μ_f) uncertainty, is shown separately as the light grey portion of the total uncertainty band.

selected displayed a signature compatible with the production of direct photons in proton-proton collisions. Figure 8–4 shows the graphical representation of the event with the highest detected photon transverse energy of $E_{\mathrm{T}}^{\gamma} = 1.5$ TeV recorded during 2012 at a centre-of-mass energy of 8 TeV. It shows how the transverse energy of the photon is balanced by the transverse momentum of a jet ($p_{\mathrm{T}} = 1.3$ TeV). This type of event signature is compatible with that expected from processes leading to the direct production of photons.

8.3 Comparisons to Other Analyses

As mentioned in Section 1.2, the inclusive prompt photon cross-section has been measured before in proton-proton collisions. This section highlights differences between previous measurements and measurements presented in this thesis. The ATLAS collaboration reported the measurement of the inclusive prompt photon cross-section in proton-proton collisions at $\sqrt{s} = 7$ TeV in three separate papers [9–11]. These three sets of measurements covered different regions of photon transverse energy and pseudorapidity. Figure 8–5 shows the region of phase space, expressed in terms of Q^2 and x, covered by the three previous ATLAS measurements and the measurements presented in this thesis[2] . The measurements presented here extend to higher transverse photon energy, and in the lower E_{T}^{γ} region, probe a new kinematic region at low x values. The results, especially at high E_{T}^{γ} and large η values, may be incorporated

[2] The direct translation of Q^2 into E_{T}^{γ} and $\mathrm{x} = \frac{\mathrm{Q}}{\sqrt{\mathrm{s}}}\mathrm{e}^{\pm\eta}$ is based on the massless properties of the photon (rapidity = pseudorapidity) and is only exact for direct photon production through a $2 \to 2$ process.

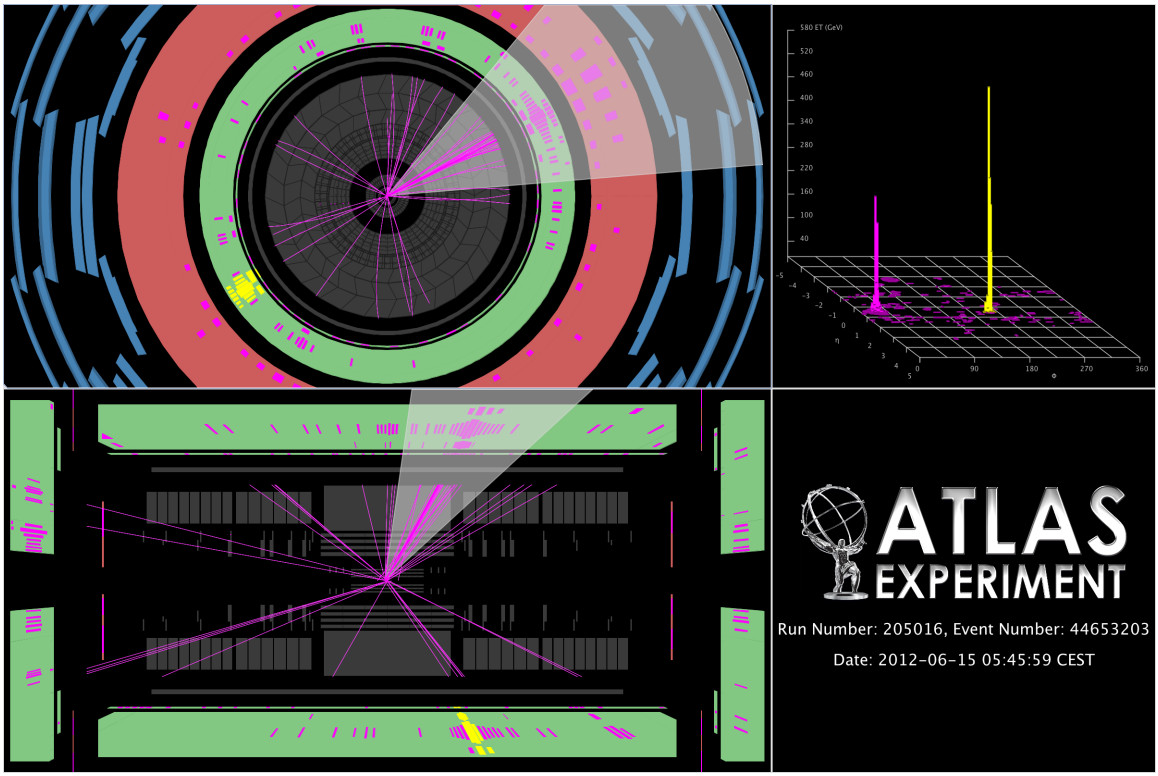

Figure 8–4: Event display of event number 44653203 in run number 205016. The photon candidate is identified as the yellow cluster of deposited energy in the electromagnetic calorimeter at $\eta = 0.53$. The photon candidate is measured to have a transverse energy of 1.5 TeV. The white triangular region indicates the direction of a reconstructed jet with transverse momentum of 1.3 TeV. The photon candidate is categorized as unconverted and has an isolation energy of 0.23 GeV.

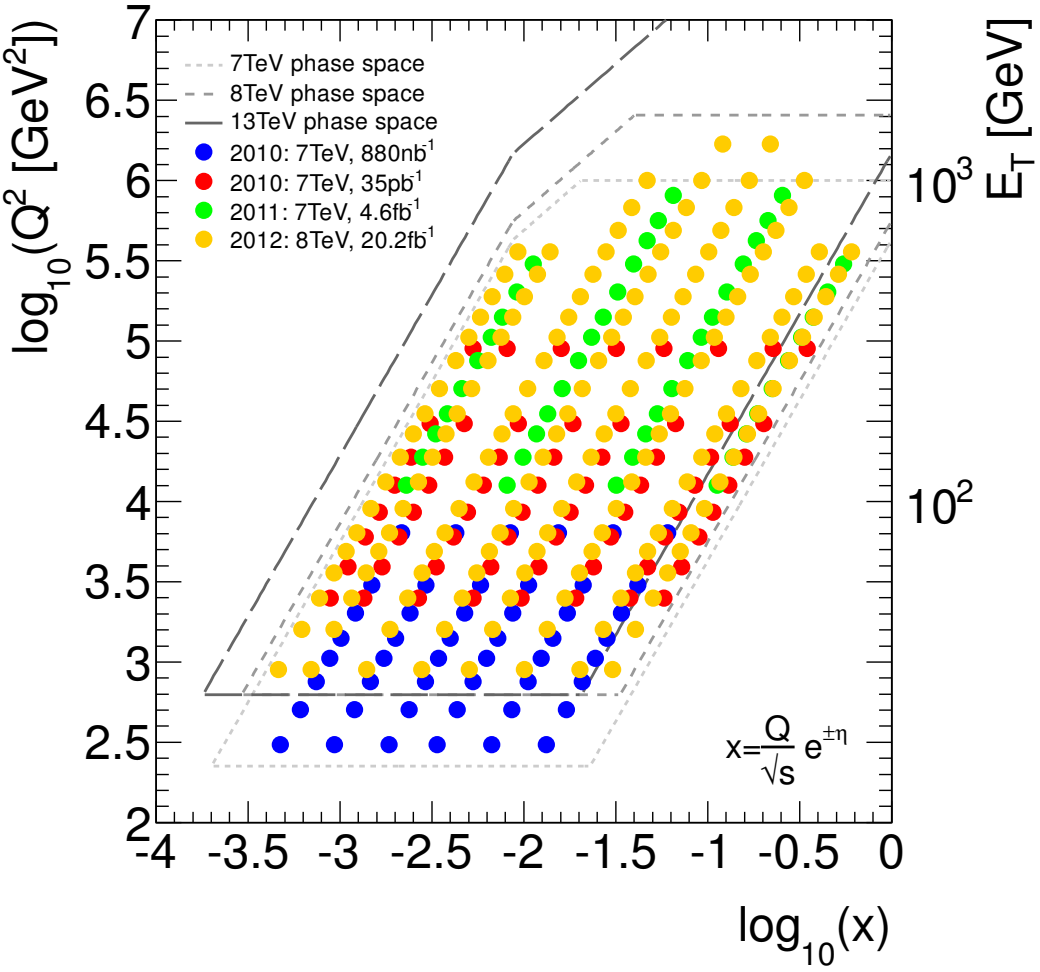

Figure 8–5: Region of kinematic phase space covered by the different ATLAS measurements of the inclusive direct photon production cross-section. The kinematic phase space coverage is expressed in terms of the interaction momentum transfer, Q^2 (related to the photon transverse energy E_{T}^{γ}), and proton momentum fraction x (related to the photon pseudorapidity η). The theoretically maximum kinematic phase space reach of the LHC at a given centre-of-mass energy is also shown. The minimum attainable Q^2 values are taken as the minimum E_{T}^{γ} trigger thresholds that were available during the different ATLAS data taking periods.

in PDF fits to further reduce the relatively large gluon PDF uncertainty at high Q^2 and larger x values. Table 8–1 summarizes the different transverse energy and pseudorapidity regions covered by each ATLAS measurement. Another distinguishing feature between the different analyses is the choice of the requirements applied to the photon transverse isolation energy. All previous measurements are based on a fixed $E_{\mathrm{T}}^{\mathrm{iso}}$ cut value independent of E_{T}^{γ}. In contrast, the analysis presented here uses an E_{T}^{γ}-dependent transverse isolation energy cut. Given the differences in the event selection and centre-of-mass energy, a comparison between the different values of measured cross-section is only approximate. A comparison of the statistical and systematic uncertainties however is straightforward and can reveal the predictive power of each analysis. Figure 8–6 shows this comparison to previous measurements. A reduction of statistical[3] and systematic uncertainty is clearly visible throughout the entire E_{T}^{γ} range considered. Compared to previous analyses the excluded pseudorapidity region[4] in the measurement presented here is adjusted by increasing the upper exclusion value from 1.52 to 1.56. Therefore, the third pseudorapidity bin is slightly smaller compared to previous measurements. It is worth pointing out that the comparison of uncertainties is not exact since the cross-section measurements using 2011 data were only divided into two η regions, while other analyses were divided into

[3] The statistical uncertainty is reduced even in the low E_{T}^{γ} region where photon triggers were prescaled in 2012.

[4] The reconstruction efficiency and photon energy scale is not as precisely measured in the transition region ($1.37 \leq |\eta| < 1.56$) of the electromagnetic calorimeter from the barrel to the end-caps than in other regions of the calorimeter.

Year	**Int. Luminosity**	E_{T}^{γ} **Range** (GeV)	η **regions**	E_T^{iso} (GeV)
2010	$880\,nb^{-1}$	$15 < E_T^{\gamma} < 100$	0-1.37, 1.52-1.81 1.52-1.81	< 3 GeV
2010	$35\,pb^{-1}$	$45 < E_T^{\gamma} < 400$	0-1.37, 1.52-2.37 1.52-1.81,1.81-2.37	< 3 GeV
2011	$4.6\,fb^{-1}$	$100 < E_T^{\gamma} < 1000$	0-1.37, 1.52-2.37	< 7 GeV
2012[5]	$20.2\,fb^{-1}$	$25 < E_T^{\gamma} < 1500$	0-0.6, 0.6-1.37, 1.56-1.81,1.81-2.37	E_T^{γ}-dependent

Table 8–1: Summary of the different transverse energy ranges and pseudorapidity regions included in each ATLAS measurement. The transverse isolation energy requirement used in each analysis is also listed.

four η regions. The significant reduction in systematic uncertainties in the barrel region for $E_{\mathrm{T}}^{\gamma} > 100$ GeV is largely due to a different approach at estimating the systematic uncertainty associated with the parton shower and hadronization models used in simulated events.

The CMS collaboration has also measured the inclusive prompt photon production cross-section in proton-proton collisions at $\sqrt(s) = 7$ TeV [8]. The cross-section was measured by the CMS collaboration in one region of $|\eta| < 1.45$ and for transverse photon energies of $21 < E_{\mathrm{T}}^{\gamma} < 300$ GeV. The CMS analysis uses an isolation requirement of 5 GeV for simulated events and three different isolation criteria for reconstructed photon candidates corresponding to three different subsystems of the CMS detector (track isolation < 2.2 GeV, electromagnetic calorimeter isolation < 4.2 GeV and hadronic calorimeter isolation < 2.2 GeV).

The results on prompt photon cross-section from previous ATLAS [9–11] measurements, CMS [8], D0 [6] and CDF [7] are compared and found to be consistent with

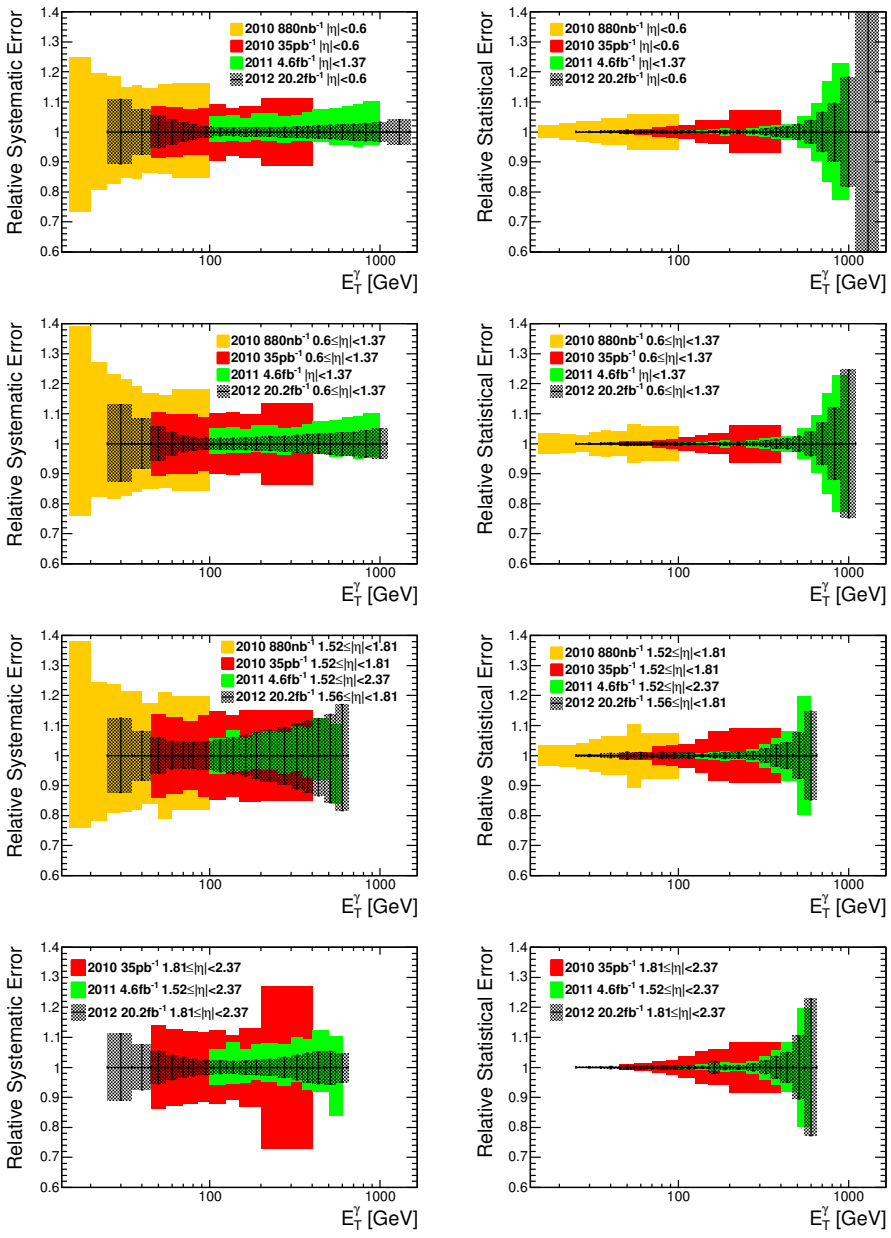

Figure 8–6: The relative size of the statistical and systematic uncertainties for all four inclusive prompt photon cross-section measurements performed with the ATLAS detector. The left column shows a comparison of the relative total systematic uncertainty without including the luminosity uncertainty. The right column shows a comparison of the total relative statistical uncertainty of the measurements. Each row corresponds to measurements performed in a different η region.

NLO calculations from JETPHOX. These measurements have also observed an overall normalization offset of the NLO predictions of the order of 10 %. Nevertheless, all previous measurements observed a relative difference between data and NLO predictions that varied as function of E_{T}^{γ}, in the region $E_{\mathrm{T}}^{\gamma} < 100$ GeV. This effect is not seen in the measurement presented here.

CHAPTER 9
Conclusion & Outlook

The inclusive differential cross-section of isolated prompt photons is measured in proton-proton collisions at a centre-of-mass energy of $\sqrt{s} = 8$ TeV using $20.2\,\text{fb}^{-1}$of collision data collected with the ATLAS detector at the LHC. This represents the most precise measurement of the prompt photon production cross-section in hadron collisions to date. The differential cross-section is measured separately in four different regions of photon pseudorapidity: $|\eta| < 0.6, 0.6 \leq |\eta| < 1.37, 1.56 \leq |\eta| < 1.81, 1.81 \leq |\eta| < 2.37$. The four pseudorapidity regions, in increasing value of pseudorapidity, cover, respectively, the transverse photon energy ranges 25 GeV $\leq E_{\text{T}}^{\gamma} <$ 1500 GeV ($|\eta| < 0.6$), 25 GeV $\leq E_{\text{T}}^{\gamma} <$ 1100 GeV ($0.6 \leq |\eta| < 1.37$), and 25 GeV $\leq E_{\text{T}}^{\gamma} <$ 650 GeV ($1.56 \leq |\eta| < 1.81$, and $1.81 \leq |\eta| < 2.37$). These measurements of the inclusive prompt photon differential cross-section extend to substantially higher values of transverse photon energy as compared to previous ATLAS measurements. Both statistical and systematic uncertainties on the measurements are typically reduced by more than a factor of 2 compared to previous measurements [9–11]. Results are compared with leading order and next-to-leading order perturbative QCD calculations and are found to be in good agreement, as a function of E_{T}^{γ}, over nine orders of magnitude.

Overall, taking into account theoretical uncertainties, next-to-leading order QCD predictions are statistically compatible with the measured differential cross-section. The E_{T}^{γ} dependence of the measured cross-section is well reproduced by next-to-leading order predictions, up to an overall normalization factor of approximately $1.10 - 1.15$. Previous measurements of the prompt photon differential cross-section performed by ATLAS and CMS have also observed a similar offset (of order 10 %) in the overall normalization of the NLO predictions. The source of this overall normalization offset of the NLO predictions still needs to be investigated. Changes in NLO cross-section predictions associated with the use of different PDF sets (CT10, HeraPDF1.5, NNPDF2.3 and MSTW2008NLO) are observed to be much smaller (factor of 3 or more) than the overall theoretical uncertainty on the predictions. It is therefore not possible to make any statistically significant distinction between PDF sets based on a comparison with the measured cross-section. Nevertheless, the adequacy of the predicted E_{T}^{γ} dependence of the cross-section calculated at next-to-leading order, along with reduced experimental uncertainties should make it possible to use the cross-section measurements as input to a global PDF fit in order to reduce uncertainties on the PDFs.

The inclusion of the cross-section measurement into a global PDF fit, by the PDF community, will be an important next step in order to fully explore the impact of the results presented in this thesis. In addition, the measurement would greatly benefit from a reduction of the dominant theoretical uncertainty, the scales uncertainty. This is especially true for the intermediate E_{T}^{γ} range where the experimental uncertainties

are only a few percent. A reduction could be accomplished through NNLO predictions of the photon production cross-section that are unfortunately not yet available. In the future the reduction of theoretical scales uncertainty will become even more important as the statistics increase at high E_{T}^{γ} values from higher luminosity runs at the LHC at centre-of-mass energies of 13 TeV and 14 TeV. The significant increase in centre-of-mass energies at the LHC will allow to measure the cross-section at E_{T}^{γ} values of multiple TeV and test the predictions of the SM in new regions of phase space. The measurement at high E_{T}^{γ} can further provide constraints on the large gluon PDF uncertainties at large values of momentum fraction x. In addition, measurements of the cross-section at small E_{T}^{γ} will allow to test the predictions of the SM at small values of x previously not accessible. The gluon PDF uncertainties are of the same relative magnitude at low x values as they are for high x values. For ongoing and upcoming runs at the LHC it is therefore important to keep the E_{T}^{γ} threshold for photons as low as possible.

APPENDIX A
Cross-check of unfolding procedure

Results obtained from unfolding detector effects from the cross-section measurement using a bin-by-bin procedure were cross-checked using an unfolding iterative approach based on Bayes Theorem [75]. This method iteratively[1] unfolds the differential cross-section by using as the truth level distribution the unfolded distribution obtained from the previous iteration of the unfolding procedure. Figure A–1 shows the relative differences on the final cross-section measurement obtained using either the bin-by-bin or the Bayes theorem method for unfolding the detector effects. The uncertainties shown in Figure A–1 correspond to the statistical uncertainty on the measured cross-section since any systematic uncertainty is canceled in the direct comparison of the methods. Both unfolding methods yield the same results within statistical uncertainties which validates the simpler choice of using the bin-by-bin unfolding procedure for the cross-section measurement.

[1] The unfolding is done using in the first iteration the original MC distribution as the prior of the Bayes theorem. In subsequent iterations, the unfolded distribution obtained in the previous iteration is used as the prior for the next iteration. In this analysis the result converges after four iterations.

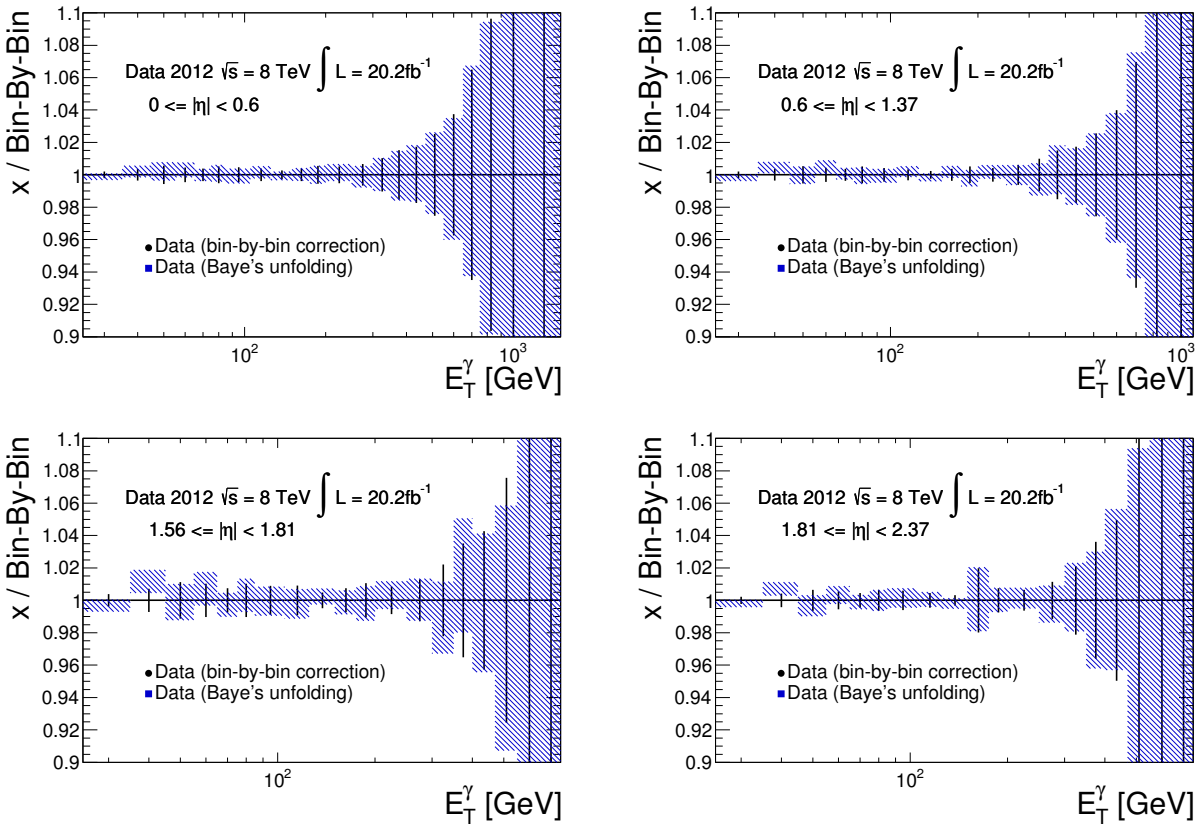

Figure A–1: Comparison of the unfolded differential cross-section as a function of E_{T}^{γ} in four η regions using either the bin-by-bin method or the Bayes theorem to unfold the data. For illustration purposes the ratio with respect to the nominal differential cross-section (bin-by-bin method to unfold) is shown. The uncertainty bars correspond to only the statistical uncertainty of the measured cross-section.

APPENDIX B
Distribution of the geometrical match ΔR between identified and truth-level photons measured in MC simulated events.

The distribution of $\Delta R = \sqrt{\Delta\eta^2 + \Delta\phi^2}$ between identified and truth-level photons is shown in Figure B–1 using simulated MC events (`PYTHIA` and `SHERPA`). Based on these distributions a value of $\Delta R < 0.2$ was chosen to define a match between identified photons at detector level and truth-level photons.

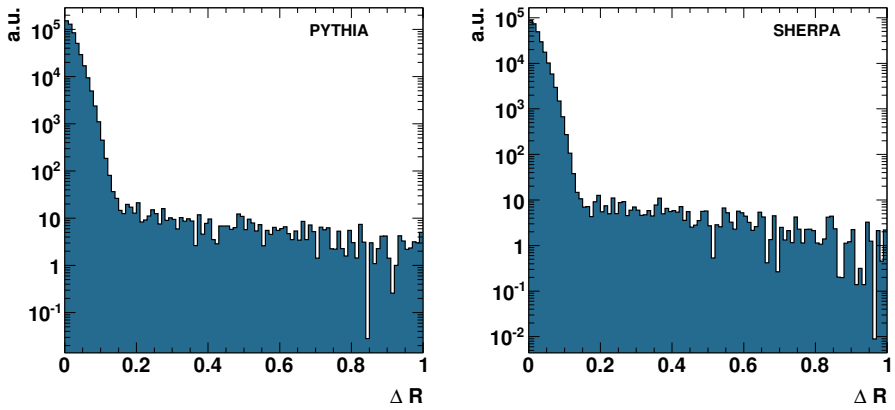

Figure B–1: The ΔR distribution between identified and truth-level photons obtained using `PYTHIA` (left) and `SHERPA` (right).

APPENDIX C
Measured inclusive prompt photon cross-section and uncertainties

The measured inclusive prompt photon cross-section values in each E_{T}^{γ} bin with its associated statistical and systematic uncertainties are tabulated in Table C–1 for $|\eta| < 0.6$, Table C–2 for $0.6 \leq |\eta| < 1.37$, Table C–3 for $1.56 \leq |\eta| < 1.81$, and Table C–4 for $1.82 \leq |\eta| < 2.37$.

E_{T}^{γ} bin [GeV]	$d\sigma^{\gamma}/dE_{\mathrm{T}}^{\gamma}$	Stat. Unc.	Sys. Unc.	[pb/GeV]
$25-35$	1.03	± 0.00	$^{+0.11}_{-0.11}$	$\times 10^{3}$
$35-45$	3.01	± 0.01	$^{+0.23}_{-0.22}$	$\times 10^{2}$
$45-55$	1.15	± 0.01	$^{+0.06}_{-0.06}$	$\times 10^{2}$
$55-65$	5.02	± 0.02	$^{+0.20}_{-0.20}$	$\times 10^{1}$
$65-75$	2.53	± 0.01	$^{+0.08}_{-0.08}$	$\times 10^{1}$
$75-85$	1.37	± 0.01	$^{+0.03}_{-0.03}$	$\times 10^{1}$
$85-105$	6.36	± 0.03	$^{+0.11}_{-0.11}$	$\times 10^{0}$
$105-125$	2.54	± 0.01	$^{+0.03}_{-0.03}$	$\times 10^{0}$
$125-150$	1.09	± 0.00	$^{+0.01}_{-0.01}$	$\times 10^{0}$
$150-175$	4.83	± 0.02	$^{+0.07}_{-0.07}$	$\times 10^{-1}$
$175-200$	2.34	± 0.01	$^{+0.03}_{-0.03}$	$\times 10^{-1}$
$200-250$	9.82	± 0.05	$^{+0.14}_{-0.15}$	$\times 10^{-2}$
$250-300$	3.42	± 0.02	$^{+0.05}_{-0.06}$	$\times 10^{-2}$
$300-350$	1.41	± 0.01	$^{+0.02}_{-0.03}$	$\times 10^{-2}$
$350-400$	6.55	± 0.10	$^{+0.13}_{-0.13}$	$\times 10^{-3}$
$400-470$	2.84	± 0.05	$^{+0.06}_{-0.06}$	$\times 10^{-3}$
$470-550$	1.13	± 0.03	$^{+0.03}_{-0.02}$	$\times 10^{-3}$
$550-650$	4.04	± 0.15	$^{+0.10}_{-0.10}$	$\times 10^{-4}$
$650-750$	1.39	± 0.09	$^{+0.04}_{-0.04}$	$\times 10^{-4}$
$750-900$	4.35	± 0.42	$^{+0.12}_{-0.13}$	$\times 10^{-5}$
$900-1100$	9.33	± 1.70	$^{+0.30}_{-0.30}$	$\times 10^{-6}$
$1100-1500$	6.11	± 3.80	$^{+0.25}_{-0.25}$	$\times 10^{-7}$

Table C–1: The measured inclusive prompt photon cross-section in each E_{T}^{γ} bin with its associated statistical and systematic uncertainties in the region $|\eta| < 0.6$.

E_{T}^{γ} bin [GeV]	$d\sigma^{\gamma}/dE_{\mathrm{T}}^{\gamma}$	Stat. Unc.	Sys. Unc.	[pb/GeV]
$25-35$	1.34	± 0.00	$^{+0.17}_{-0.17}$	$\times 10^{3}$
$35-45$	3.87	± 0.01	$^{+0.33}_{-0.31}$	$\times 10^{2}$
$45-55$	1.44	± 0.01	$^{+0.08}_{-0.08}$	$\times 10^{2}$
$55-65$	6.60	± 0.03	$^{+0.25}_{-0.25}$	$\times 10^{1}$
$65-75$	3.30	± 0.01	$^{+0.09}_{-0.09}$	$\times 10^{1}$
$75-85$	1.77	± 0.01	$^{+0.04}_{-0.04}$	$\times 10^{1}$
$85-105$	8.19	± 0.03	$^{+0.16}_{-0.16}$	$\times 10^{0}$
$105-125$	3.23	± 0.01	$^{+0.06}_{-0.06}$	$\times 10^{0}$
$125-150$	1.39	± 0.00	$^{+0.03}_{-0.03}$	$\times 10^{0}$
$150-175$	6.15	± 0.02	$^{+0.13}_{-0.13}$	$\times 10^{-1}$
$175-200$	3.01	± 0.02	$^{+0.07}_{-0.06}$	$\times 10^{-1}$
$200-250$	1.24	± 0.05	$^{+0.03}_{-0.03}$	$\times 10^{-1}$
$250-300$	4.30	± 0.03	$^{+0.11}_{-0.11}$	$\times 10^{-2}$
$300-350$	1.66	± 0.02	$^{+0.05}_{-0.05}$	$\times 10^{-2}$
$350-400$	7.54	± 0.11	$^{+0.23}_{-0.23}$	$\times 10^{-3}$
$400-470$	3.08	± 0.05	$^{+0.10}_{-0.10}$	$\times 10^{-3}$
$470-550$	1.16	± 0.03	$^{+0.04}_{-0.04}$	$\times 10^{-3}$
$550-650$	3.81	± 0.15	$^{+0.14}_{-0.15}$	$\times 10^{-4}$
$650-750$	1.24	± 0.09	$^{+0.05}_{-0.05}$	$\times 10^{-4}$
$750-900$	2.96	± 0.35	$^{+0.13}_{-0.13}$	$\times 10^{-5}$
$900-1100$	7.22	± 1.78	$^{+0.36}_{-0.35}$	$\times 10^{-6}$

Table C–2: The measured inclusive prompt photon cross-section in each E_{T}^{γ} bin with its associated statistical and systematic uncertainties in the region $0.6 \leq |\eta| < 1.37$

E_{T}^{γ} bin [GeV]	$d\sigma^{\gamma}/dE_{\mathrm{T}}^{\gamma}$	Stat. Unc.	Sys. Unc.	[pb/GeV]
$25-35$	4.41	± 0.02	$^{+0.55}_{-0.54}$	$\times 10^{2}$
$35-45$	1.34	± 0.01	$^{+0.11}_{-0.11}$	$\times 10^{2}$
$45-55$	4.82	± 0.05	$^{+0.29}_{-0.28}$	$\times 10^{1}$
$55-65$	2.15	± 0.02	$^{+0.10}_{-0.10}$	$\times 10^{1}$
$65-75$	1.07	± 0.01	$^{+0.05}_{-0.04}$	$\times 10^{1}$
$75-85$	5.76	± 0.06	$^{+0.25}_{-0.25}$	$\times 10^{0}$
$85-105$	2.69	± 0.02	$^{+0.13}_{-0.13}$	$\times 10^{0}$
$105-125$	1.01	± 0.01	$^{+0.05}_{-0.05}$	$\times 10^{0}$
$125-150$	4.37	± 0.02	$^{+0.26}_{-0.27}$	$\times 10^{-1}$
$150-175$	1.88	± 0.01	$^{+0.13}_{-0.13}$	$\times 10^{-1}$
$175-200$	8.97	± 0.10	$^{+0.69}_{-0.69}$	$\times 10^{-2}$
$200-250$	3.48	± 0.03	$^{+0.29}_{-0.30}$	$\times 10^{-2}$
$250-300$	1.09	± 0.01	$^{+0.10}_{-0.10}$	$\times 10^{-2}$
$300-350$	3.75	± 0.08	$^{+0.40}_{-0.41}$	$\times 10^{-3}$
$350-400$	1.52	± 0.05	$^{+0.18}_{-0.19}$	$\times 10^{-3}$
$400-470$	5.10	± 0.22	$^{+0.63}_{-0.69}$	$\times 10^{-4}$
$470-550$	1.27	± 0.10	$^{+0.18}_{-0.20}$	$\times 10^{-4}$
$550-650$	2.70	± 0.40	$^{+0.46}_{-0.50}$	$\times 10^{-5}$

Table C–3: The measured inclusive prompt photon cross-section in each E_{T}^{γ} bin with its associated statistical and systematic uncertainties in the region $1.56 \leq |\eta| < 1.81$.

E_{T}^{γ} bin [GeV]	$d\sigma^{\gamma}/dE_{\mathrm{T}}^{\gamma}$	Stat. Unc.	Sys. Unc.	[pb/GeV]
$25-35$	9.45	± 0.02	$^{+1.06}_{-1.03}$	$\times 10^{2}$
$35-45$	2.83	± 0.01	$^{+0.21}_{-0.21}$	$\times 10^{2}$
$45-55$	1.03	± 0.01	$^{+0.06}_{-0.06}$	$\times 10^{2}$
$55-65$	4.47	± 0.02	$^{+0.18}_{-0.18}$	$\times 10^{1}$
$65-75$	2.15	± 0.01	$^{+0.07}_{-0.07}$	$\times 10^{1}$
$75-85$	1.17	± 0.01	$^{+0.03}_{-0.03}$	$\times 10^{1}$
$85-105$	5.36	± 0.03	$^{+0.13}_{-0.13}$	$\times 10^{0}$
$105-125$	2.04	± 0.01	$^{+0.04}_{-0.04}$	$\times 10^{0}$
$125-150$	8.27	± 0.03	$^{+0.17}_{-0.17}$	$\times 10^{-1}$
$150-175$	3.31	± 0.07	$^{+0.07}_{-0.07}$	$\times 10^{-1}$
$175-200$	1.51	± 0.01	$^{+0.04}_{-0.04}$	$\times 10^{-1}$
$200-250$	5.40	± 0.03	$^{+0.15}_{-0.15}$	$\times 10^{-2}$
$250-300$	1.42	± 0.02	$^{+0.05}_{-0.05}$	$\times 10^{-2}$
$300-350$	4.18	± 0.09	$^{+0.17}_{-0.18}$	$\times 10^{-3}$
$350-400$	1.34	± 0.05	$^{+0.06}_{-0.07}$	$\times 10^{-3}$
$400-470$	3.86	± 0.19	$^{+0.20}_{-0.21}$	$\times 10^{-4}$
$470-550$	7.16	± 0.76	$^{+0.38}_{-0.40}$	$\times 10^{-5}$
$550-650$	1.08	± 0.25	$^{+0.05}_{-0.05}$	$\times 10^{-5}$

Table C–4: The measured inclusive prompt photon cross-section in each E_{T}^{γ} bin with its associated statistical and systematic uncertainties in the region $1.82 \leq |\eta| < 2.37$.

APPENDIX D
MC transverse isolation energy corrections

The transverse isolation energy of photon candidates in MC simulated events is shifted such that the peak of the distribution obtained using MC simulated events matches that measured in data. The shift values for each E_{T}^{γ} and η bin are listed in Table D–1 for `PYTHIA` and Table D–2 for `SHERPA`.

PYTHIA (GeV)	$\|\eta^\gamma\|$ <**0.6**	**0.6**< $\|\eta^\gamma\|$ <**1.37**	**1.56**< $\|\eta^\gamma\|$ <**1.81**	**1.81**< $\|\eta^\gamma\|$ <**2.37**
$25 < E_T^\gamma < 35$	0.06	0.17	0.09	0.11
$35 < E_T^\gamma < 45$	0.07	0.27	0.05	0.17
$45 < E_T^\gamma < 55$	0.10	0.32	0.23	0.19
$55 < E_T^\gamma < 65$	0.14	0.34	0.19	0.25
$65 < E_T^\gamma < 75$	0.14	0.39	0.22	0.26
$75 < E_T^\gamma < 85$	0.17	0.41	0.24	0.27
$85 < E_T^\gamma < 105$	0.10	0.51	0.24	0.33
$105 < E_T^\gamma < 125$	0.10	0.60	0.29	0.42
$125 < E_T^\gamma < 150$	0.14	0.73	0.40	0.49
$150 < E_T^\gamma < 175$	0.18	0.89	0.47	0.54
$175 < E_T^\gamma < 200$	0.16	1.02	0.49	0.73
$200 < E_T^\gamma < 250$	0.18	1.19	0.59	0.66
$250 < E_T^\gamma < 300$	0.31	1.39	0.43	0.68
$300 < E_T^\gamma < 350$	0.33	1.62	0.47	0.78
$350 < E_T^\gamma < 400$	0.26	1.82	0.41	0.65
$400 < E_T^\gamma < 470$	0.33	1.87	0.41	0.82
$470 < E_T^\gamma < 550$	0.60	2.34	-0.51	1.07
$550 < E_T^\gamma < 650$	0.23	2.74	-0.51	1.07
$650 < E_T^\gamma < 750$	1.09	2.64	-	-
$750 < E_T^\gamma < 900$	1.41	3.44	-	-
$900 < E_T^\gamma < 1100$	0.94	4.58	-	-
$1100 < E_T^\gamma < 1500$	0.94	-	-	-

Table D–1: `PYTHIA` correction values applied to shift the mean value of the transverse isolation energy ($E_{\mathrm{T}}^{\mathrm{iso}}$) distributions to match the measured data mean value of $E_{\mathrm{T}}^{\mathrm{iso}}$. The shift values are quoted in GeV.

SHERPA (GeV)	$\|\eta^\gamma\|$ <**0.6**	**0.6**< $\|\eta^\gamma\|$ <**1.37**	**1.56**< $\|\eta^\gamma\|$ <**1.81**	**1.81**< $\|\eta^\gamma\|$ <**2.37**
$25 < E_T^\gamma < 35$	-0.02	0.11	0.08	0.09
$35 < E_T^\gamma < 45$	0.02	0.19	0.08	0.13
$45 < E_T^\gamma < 55$	-0.01	0.25	0.15	0.20
$55 < E_T^\gamma < 65$	0.09	0.29	0.15	0.23
$65 < E_T^\gamma < 75$	0.05	0.34	0.18	0.25
$75 < E_T^\gamma < 85$	0.14	0.43	0.19	0.32
$85 < E_T^\gamma < 105$	0.06	0.42	0.26	0.31
$105 < E_T^\gamma < 125$	0.06	0.54	0.30	0.37
$125 < E_T^\gamma < 150$	0.12	0.68	0.36	0.47
$150 < E_T^\gamma < 175$	0.11	0.84	0.52	0.56
$175 < E_T^\gamma < 200$	0.05	0.93	0.60	0.57
$200 < E_T^\gamma < 250$	0.17	1.12	0.45	0.60
$250 < E_T^\gamma < 300$	0.32	1.31	0.42	0.60
$300 < E_T^\gamma < 350$	0.26	1.57	0.37	0.67
$350 < E_T^\gamma < 400$	0.26	1.83	0.36	0.61
$400 < E_T^\gamma < 470$	0.31	1.85	0.41	0.78
$470 < E_T^\gamma < 550$	0.56	2.34	-0.51	1.03
$550 < E_T^\gamma < 650$	0.16	2.72	-0.51	1.03
$650 < E_T^\gamma < 750$	1.13	2.64	-	-
$750 < E_T^\gamma < 900$	1.43	3.36	-	-
$900 < E_T^\gamma < 1100$	0.87	4.53	-	-
$1100 < E_T^\gamma < 1500$	0.87	-	-	-

Table D–2: `SHERPA` correction values applied to shift the mean value of the transverse isolation energy ($E_{\mathrm{T}}^{\mathrm{iso}}$) distributions to match the measured data mean value of $E_{\mathrm{T}}^{\mathrm{iso}}$. The shift values are quoted in GeV.

APPENDIX E
Uncertainty estimate of R^{bkg} used in the 2D sideband method

The uncertainty assigned to the value of R^{bkg} used in the background subtraction method is estimated in data by measuring R^{bkg} in the non-isolated regions of the 2D sideband method. The non-isolated region is divided into regions B,D,E and F as shown in Figure 7–3. Figure E–1 shows the measured values of R^{bkg} as a function of E_{T}^{γ} in the four pseudorapidity regions. Based on the measurements presented in Figure E–1, a value of $R^{\mathrm{bkg}} = 1.0 \pm 0.1$ is used to calculate the final cross-section results.

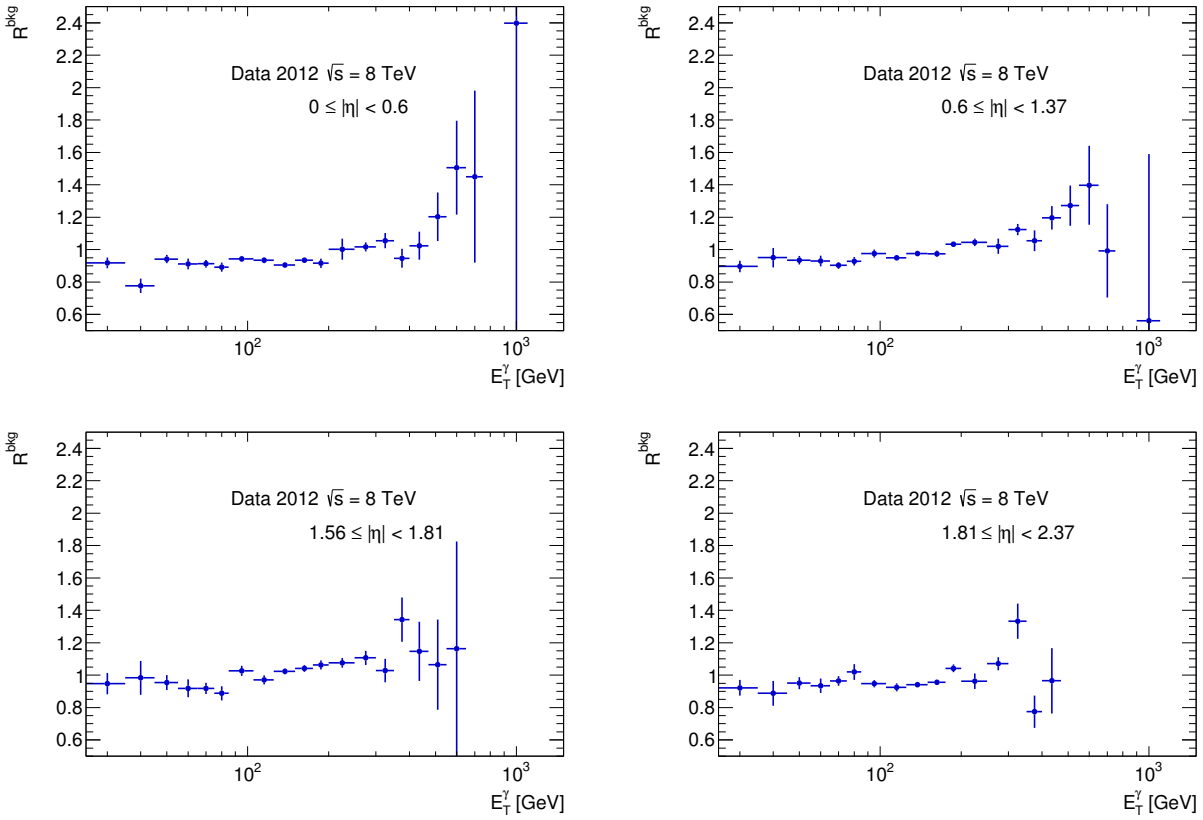

Figure E–1: Background ratio R^{bkg} measured in data in the non-isolated regions B,D,E and F shown in Figure 7–3.

APPENDIX F
Distributions of the nine discriminating variables used within the photon identification.

The distributions of the nine discriminating variables used to separate the signal photons from background photons (mainly originating within jets) as part of the photon identification for unconverted and converted photons are shown in Figure F–1 and Figure F–2 respectively. The specific cut values are adjusted as a function of E_{T}^{γ} and $|\eta|$ in order to maximally explore the differences in shower shape of signal and background photons.

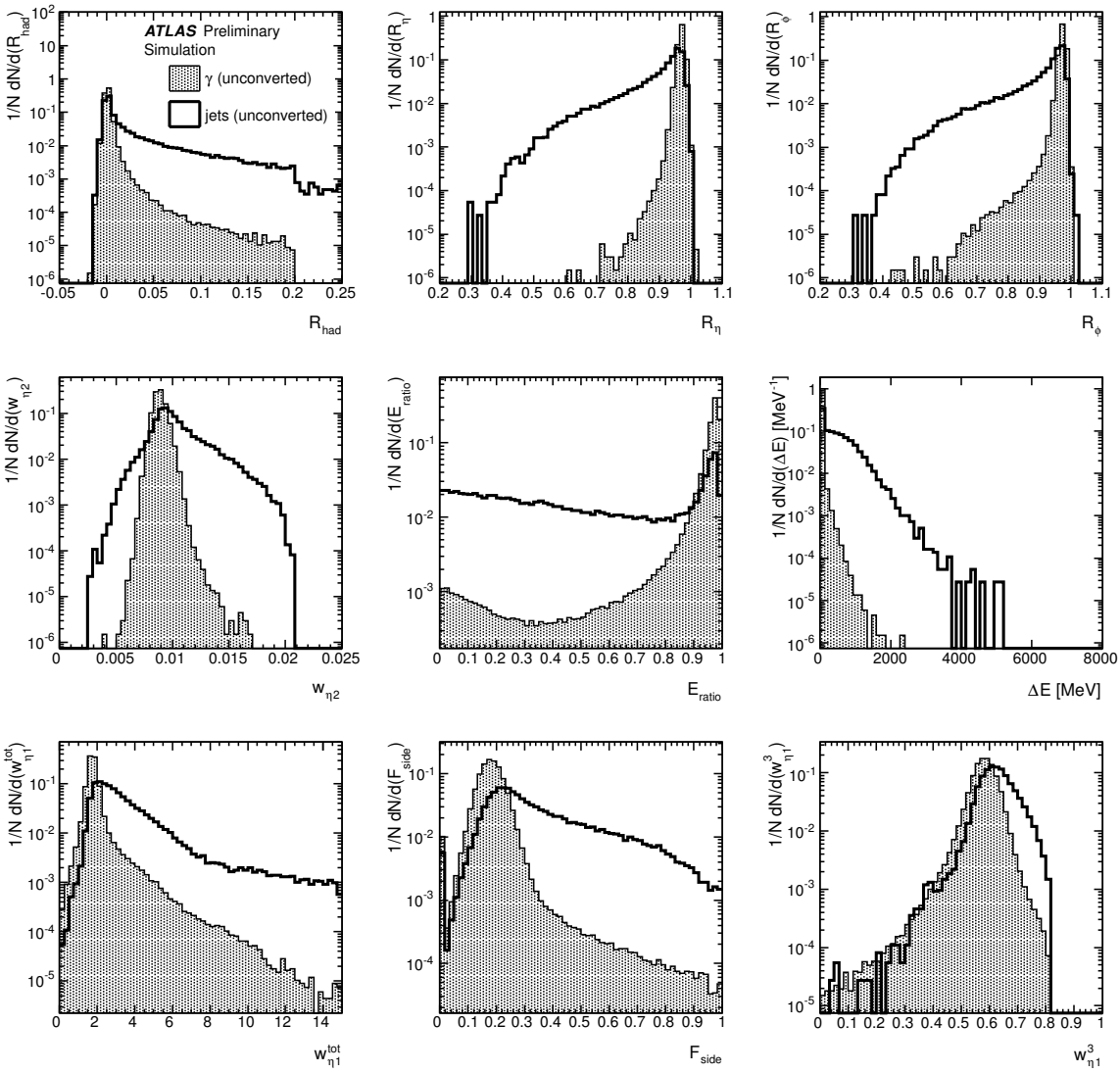

Figure F–1: Normalized distributions of the nine discriminating variables in the region $|\eta| < 0.6$ for $E_{\mathrm{T}}^{\gamma} > 20$ GeV for true (filled) and fake photons identified as unconverted [65].

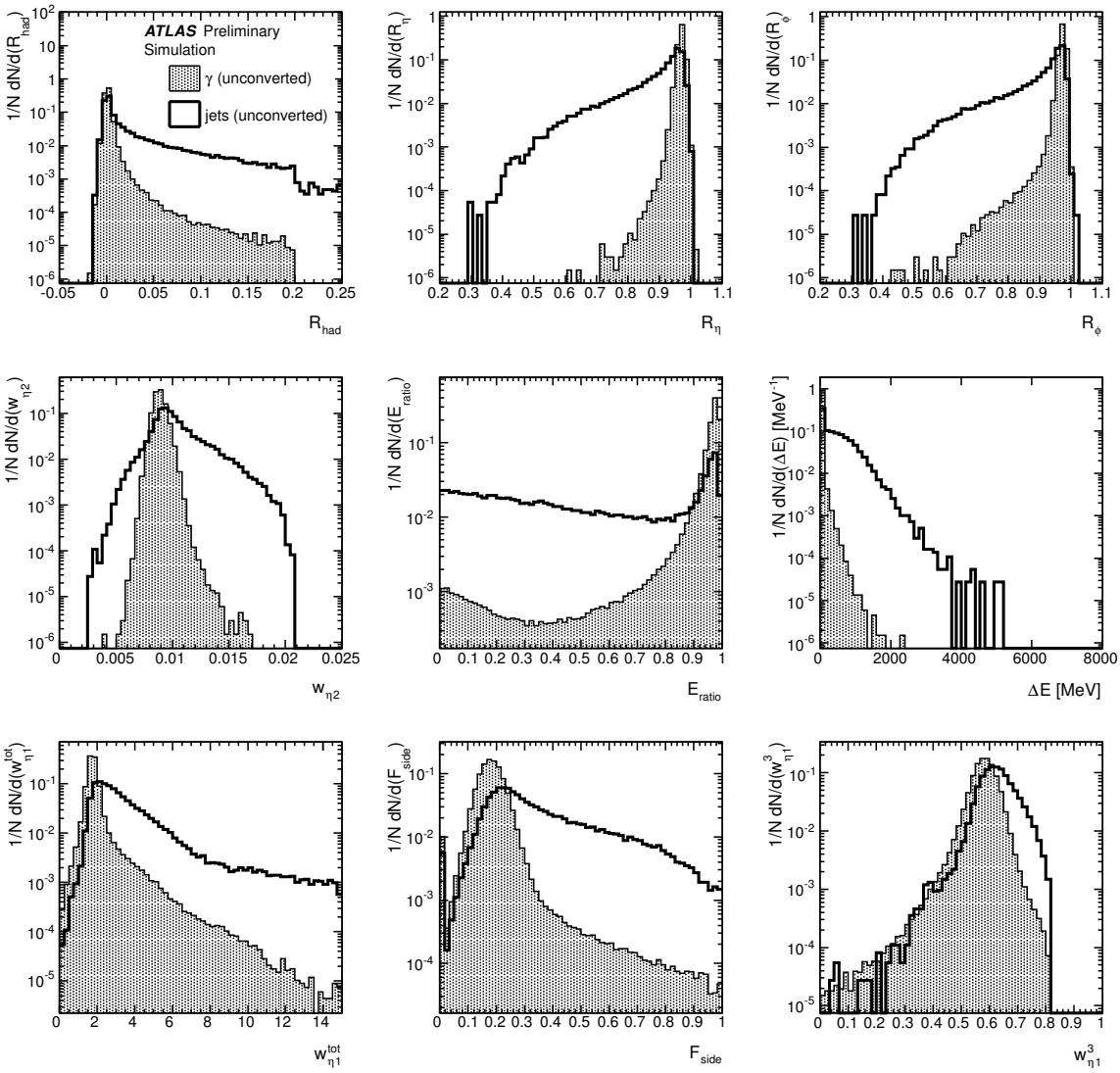

Figure F–2: Normalized distributions of the nine discriminating variables in the region $|\eta| < 0.6$ for $E_{\mathrm{T}}^{\gamma} > 20$ GeV for true (filled) and fake photons identified as converted [65].

References

[1] D. Griffiths, *Introduction to Elementary Particles*, Wiley-VCH, 2nd edition, 1987.

[2] E. Lohrman, *Hochenergiephysik*, Teubner Physik, 5. Auflage, 2005.

[3] Particle Data Group, K. A. Olive et al., *Review of Particle Physics*, Chin. Phys., C38:090001, 2014.

[4] E. Amaldi et al., *Search for Single Photon Direct Production in p p Collisions at* $\sqrt{s}$ *= 53.2-GeV*, Phys. Lett., B77:240–244, 1978.

[5] H1 Collaboration, F. D. Aaron et al., *Prompt Photons in Photon Production at HERA*, Eur.Phys.J., C66:17–33, 2010, `arXiv:0910.5631 [hep-ex]`.

[6] D0 Collaboration, V. M. Abazov et al., *Measurement of the isolated photon cross section in* $p\bar{p}$ *collisions at* $\sqrt{s}$ *= 1.96-TeV*, Phys. Lett. D, 639:151, 2006, `arXiv:051.1054 [hep-ex]`.

[7] CDF Collaboration, D. Acosta et al., *Measurement of the inclusive isolated prompt photon cross section in* $p\bar{p}$ *collisions at* $\sqrt{s} = 1.96$ *TeV using the CDF detector*, Phys. Rev. D, 80:111106(R), 2009, `arXiv:0910.3623 [hep-ex]`.

[8] CMS Collaboration, *Measurement of the Differential Cross Section for Isolated Prompt Photon Production in pp Collisions at 7 TeV*, Phys. Rev. D, 84:052011, 2011, `arXiv:1108.2044 [hep-ex]`.

[9] ATLAS Collaboration, *Measurement of the inclusive isolated prompt photon cross section in pp collisions at* $\sqrt{s} = 7$ *TeV with the ATLAS detector*, Phys. Rev. D, 83:052005, 2011 , `arXiv:1012.4389 [hep-ex]`.

[10] ATLAS Collaboration, *Measurement of the inclusive isolated prompt photon cross- section in pp collisions at* $\sqrt{s} = 7$ *TeV using 35* pb^{-1} *of ATLAS data*, Phys. Lett. B, 706:150, 2011 , `arXiv:1108.0253 [hep-ex]`.

[11] ATLAS Collaboration, *Measurement of the inclusive isolated prompt photon cross section in pp collisions at sqrt(s) = 7 TeV with the ATLAS detector using 4.6 fb^{-1}*, Phys. Rev. D, 89:052004, 2014 , arXiv:1311.1440 [hep-ex].

[12] E. Rutherford, *The scattering of alpha and beta particles by matter and the structure of the atom*, Phil.Mag., 21:669–688, 1911.

[13] J. Chadwick, *Possible Existence of a Neutron*, Nature, 129:312, 1932.

[14] J. I. Friedman and H. W. Kendall, *Deep inelastic electron scattering*, Ann. Rev. Nucl. Part. Sci., 22:203–254, 1972.

[15] R. P. Feynman, *The behavior of hadron collisions at extreme energies*, Conf.Proc., C690905:237–258, 1969.

[16] J. D. Bjorken and E. A. Paschos, *Inelastic Electron-Proton and γ-Proton Scattering and the Structure of the Nucleon*, Phys. Rev., 185:1975–1982, Sep 1969.

[17] D. J. Gross and F. Wilczek, *Ultraviolet Behavior of Non-Abelian Gauge Theories*, Phys. Rev. Lett., 30:1343–1346, Jun 1973.

[18] R. P. Feynman, *Mathematical Formulation of the Quantum Theory of Electromagnetic Interaction*, Phys. Rev., 80:440–457, Nov 1950.

[19] P. Pascual and R. Tarrach, *QCD: Renormalization For The Practitioner*, Lect. Notes Phys., 194:1–277, 1984.

[20] S. Forte and G. Watt, *Progress in the Determination of the Partonic Structure of the Proton*, Ann. Rev. Nucl. Part. Sci., 63:291–328, 2013, arXiv:0409313 [hep-ph].

[21] V. N. Gribov and L. N. Lipatov, *e+ e- pair annihilation and deep inelastic e p scattering in perturbation theory*, Sov.J.Nucl.Phys., 15:675–684, 1972.

[22] G. Altarelli and G. Parisi, *Asymptotic Freedom in Parton Language*, Nucl.Phys., B126:298, 1977.

[23] V. N. Gribov and L. N. Lipatov, *Deep Inelastic ep-Scattering in a Perturbation Theory*, Sov. J. Nucl. Phys., 15:438–450, 1972.

[24] H1 and ZEUS Collaboration, Dr. Eram Rizvi et al., *Combined Measurement and QCD Analysis of the Inclusive ep Scattering Cross Sections at HERA*, JHEP, 2010, arXiv:0911.0884v2 [hep-ex].

[25] H1 collaboration, *H1 Fast Navigator*, http://www-h1.desy.de.

[26] ZEUS collaboration, *The ZEUS experiment*, http://www-zeus.desy.de.

[27] J. D. Bjorken and S. D. Drell, *Relativistic quantum mechanics*, McGraw-Hill, 1964.

[28] P. Aurenche, R. Baier, M. Fontannaz, J. F. Owens, and M. Werlen, *The gluon content of the nucleon probed with real and virtual photons*, Phys. Rev. D, 39:3275, 1989.

[29] H.-L. Lai, J. Botts, J. Huston, J. G. Morfin, J. F. Owens, et al., *Global QCD analysis and the CTEQ parton distributions*, Phys. Rev. D, 51:4763, 1995, arXiv:9410404 [hep-ph].

[30] A. D. Martin, R. G. Roberts, W. J. Stirling, and R. S. Thorne, *Parton distributions: A New global analysis*, Eur. Phys. J. C, 4:463, 1998, arXiv:9803445 [hep-ph].

[31] A. D. Martin, R. G. Roberts, W. J. Stirling, and R. S. Thorne, *Parton distributions and the LHC: W and Z production*, Eur. Phys. J. C, 14:133, 2000, arXiv:9907231 [hep-ph].

[32] P. Aurenche, M. Fontannaz, J.-P. Guillet, E. Pilon, and M. Werlen, *A New critical study of photon production in hadronic collisions*, Phys. Rev. D, 73:094007, 2006, arXiv:0602133 [hep-ph].

[33] D. d'Enterria and J. Rojo, *Quantitative constraints on the gluon distribution function in the proton from collider isolated-photon data*, Nucl. Phys. B, 860:311, 2012, arXiv:1202.1762 [hep-ph].

[34] L. Evans and P. Bryant, *LHC Machine*, JINST, 3:S08001, 2008.

[35] ALICE Collaboration, K. Aamodt et al., *The ALICE experiment at the CERN LHC*, JINST, 3:S08002, 2008.

[36] ATLAS Collaboration, *The ATLAS Experiment at the CERN Large Hadron Collider*, JINST, 3:S08003, 2008.

[37] CMS Collaboration, R. Adolphi et al., *The CMS experiment at the CERN LHC*, JINST, 3:S08004, 2008.

[38] LHCb Collaboration, A. Augusto Alves et al., *The LHCb Detector at the LHC*, JINST, 3:S08005, 2008.

[39] R. L. Witkover, editor, *Proceedings: Linear Accelerator Conference, Montauk, N.Y., Sep 10-14, 1979*, 1980, http://www.osti.gov/energycitations/product.biblio.jsp?osti_id=5165613.

[40] K. H. Reich, *The CERN Proton Synchrotron Booster*, IEEE Trans. Nucl. Sci., 16:959–961, 1969.

[41] M. G. N. Hine and P. Germain, *Performance of the CERN Proton Synchrotron*, In *Proceedings, 3rd International Conference on High-Energy Accelerators, HEACC 1961*, 25-28, 1962.

[42] *First Proton Anti-proton Collisions in the CERN SPS Collider*, Phys. Lett., B107:306–309, 1981.

[43] M. Lamont, *The First Years of LHC Operation for Luminosity Production*, IPAC13, 2013, http://www.JACoW.org.

[44] K. Eggert, K. Honkavaara, and A. Morsch, *Luminosity considerations for the LHC*, CERN-AT-94-04-DI, CERN-LHC-NOTE-263, 1994, https://cds.cern.ch/record/260711.

[45] ATLAS Collaboration, *Public Luminosity Plots*, https://twiki.cern.ch/twiki/bin/view/AtlasPublic/LuminosityPublicResults.

[46] ATLAS Collaboration, *ATLAS inner detector: Technical design report, 1*, ATLAS-TDR-4, 1997, https://cds.cern.ch/record/331063.

[47] ATLAS Collaboration, *ATLAS pixel detector electronics and sensors*, JINST, 3:P07007, 2008.

[48] ATLAS Collaboration, *The ATLAS Transition Radiation Tracker (TRT) proportional drift tube: Design and performance*, JINST, 3:P02013, 2008.

[49] ATLAS Collaboration, *Particle Identification Performance of the ATLAS Transition Radiation Tracker*, ATLAS-CONF-2011-128, 2011, http://cds.cern.ch/record/1383793.

[50] ATLAS Collaboration, *ATLAS liquid argon calorimeter: Technical design report*, ATLAS-TDR-2, 1996, http://cds.cern.ch/record/331061.

[51] ATLAS Collaboration, *ATLAS muon spectrometer: Technical design report*, ATLAS-TDR-10, 1997, https://cds.cern.ch/record/331068.

[52] ATLAS Collaboration, *Performance of the Electron and Photon Trigger in p-p Collisions at $\sqrt{s}$=7 TeV with the ATLAS Detector at the LHC in 2011*, ATLAS-CONF-2012-048, 2012, http://cds.cern.ch/record/1450089.

[53] T. Sjostrand, S. Mrenna, and P. Z. Skands, *A Brief Introduction to PYTHIA 8.1*, 2007-10-20, arXiv:0710.3820v1 [hep-ph].

[54] T. Gleisberg et al., *Event generation with SHERPA 1.1*, 2008, arXiv:0811.4622v1 [hep-ph].

[55] S. Agostinelli et al., *Geant4 - A Simulation Toolkit*, Nuclear Instruments and Methods A 506, 250-303, 2003, http://geant4.cern.ch/results/publications.shtml.

[56] J. Pumplin et al., *New Generation of Parton Distributions with Uncertainties from Global QCD Analysis*, 2002, arXiv:0201195v3 [hep-ph].

[57] B. Andersson, G. Gustafson, G. Ingelman, and T. Sjostrand, *Parton Fragmentation and String Dynamics*, Phys. Rept., 97:31–145, 1983.

[58] P. Bartalini, E. L. Berger, B. Blok, G. Calucci, R. Corke, et al., *Multi-Parton Interactions at the LHC*, 2011, arXiv:1111.0469 [hep-ph].

[59] H.-L. Lai et al., *New parton distributions for collider physics*, Phys. Rev. D, 82:074024, 2010, arXiv:1007.2241 [hep-ph].

[60] J.-C. Winter, F. Krauss, and G. Soff, *A modified cluster-hadronisation model*, Eur. Phys. J. C, 36(3):381–395, 2004.

[61] S. Catani et al., *Cross section of isolated prompt photons in hadron-hadron collisions*, J. High Energy Phys., 0205:028, 2002, arXiv:0204023 [hep-ph].

[62] ATLAS Collaboration, *Measurement of the production cross section of an isolated photon associated with jets in proton-proton collisions at sqrt(s) = 7 TeV with the ATLAS detector*, Phys. Rev. D, 85, 2014 , arXiv:1203.3161 [hep-ex].

[63] ATLAS Collaboration, *Electron and photon energy calibration with the ATLAS detector using LHC Run 1 data*, Eur. Phys. J. C (2014) 74:3071, 2014, arXiv:1407.5063v2 [hep-ph].

[64] M. Aleksa, M. Delmastro, M. Fanti, R. Lafaye, W. Lampl, S. Laplace, D. Prieur, F. Tarrade, and I. Wingerter-Seez, *ATLAS Combined Testbeam*, ATL-LARG-PUB-2006-003, 2006, https://cds.cern.ch/record/942528.

[65] ATLAS Collaboration, *Expected photon performance in the ATLAS experiment*, 2011, ATL-PHYS-PUB-2011-007, ATL-COM-PHYS-2010-1051.

[66] M. Cacciari, G. P. Salam, and S. Sapeta, *On the characterisation of the underlying event*, J. High Energy Phys., 04:1004, 2010, arXiv:0912.4926 [hep-ph].

[67] M. Cacciari, G. P. Salam, and G. Soyez, *The Catchment Area of Jets*, JHEP, 04:005, 2008, arXiv:0802.1188 [hep-ph].

[68] B. Efron and R. Tibshirani, *An Introduction to the Bootstrap*, Macmillan Publishers Limited, 1993.

[69] ATLAS Collaboration, *Measurement of dijet cross sections in pp collisions at 7 TeV centre-of-mass energy using the ATLAS detector*, JHEP, 05:059, 2014, arXiv:1312.3524 [hep-ex].

[70] ATLAS Collaboration, *Improved luminosity determination in pp collisions at $\sqrt{s} = 7$ TeV using the ATLAS detector at the LHC*, Eur. Phys. J. C, 73(8):1–39, 2013, arXiv:1302.4393 [hep-ex].

[71] ATLAS Collaboration, *Measurements of the photon identification efficiency with the ATLAS detector using 4.9 fb1 of pp collision data collected in 2011*, ATLAS-CONF-2012-123, 2012, https://cds.cern.ch/record/1473426.

[72] R. Blair et al., *NLO Theoretical Predictions for Photon Measurements Using the PHOX Generators*, CERN-OPEN-2011-041, Sep 2011.

[73] H.-L. Lai, J. Huston, Z. Li, P. Nadolsky, J. Pumplin, D. Stump, and C.-P. Yuan, *Uncertainty induced by QCD coupling in the CTEQ global analysis of parton distributions*, Phys. Rev., D82:054021, 2010, arXiv:1004.4624 [hep-ph].

[74] ATLAS Collaboration, *A study of the sensitivity to the proton parton distributions of the inclusive photon production cross section in pp collisions at 7 TeV measured by the ATLAS experiment at the LHC*, ATL-PHYS-PUB-2013-018, 2013, `https://cds.cern.ch/record/1636863`.

[75] Rev. T. Bayes, *An essay toward solving a problem in the doctrine of chances*, Phil. Trans. Roy. Soc. Lond., 53:370–418, 1764.